Nanostructured catalytic films for multiphase microstructured reactors

Nanostructured Catalytic Films for Multiphase Microstructured Reactors

Proefschrift

ter verkrijging van de graad van doctor aan de
Technische Universiteit Eindhoven, op gezag van de
rector magnificus, prof.dr.ir. C.J. van Duijn, voor een
commissie aangewezen door het College voor
Promoties in het openbaar te verdedigen
op donderdag 29 oktober 2009 om 16.00 uur

door

Oki Muraza

geboren te Jakarta, Indonesië

Dit proefschrift is goedgekeurd door de promotor:

prof.dr.ir. J.C. Schouten

Copromotoren:

dr. E.V. Rebrov
en
dr. M.H.J.M. de Croon

The work described in this thesis was financed by the Dutch Technology Foundation (STW). Financial support from Shell Global Solutions, Akzo, DSM, Schering-Plough is gratefully acknowledged. A catalogue record is available from the Library Eindhoven University of Technology Nanostructured Catalytic Films For Multiphase Microstructured Reactors / by O. Muraza

A catalogue record is available from the Eindhoven University of Technology Library

ISBN: 978-90-386-2016-9

Subject headings: Catalytic films, Chemical reactors

Contents

Nanostructured Catalytic Films for Multiphase Microstructured Reactors

Summary

The application of microstructured catalytic reactors for gas-liquid reactions requires the development of new techniques for the incorporation of highly active catalytic thin films onto their microstructured surfaces. These catalytic thin films may have open porosities even up to 50%. Their application limits the pressure drop over the microreactor in comparison to micro packed beds, it enhances the catalyst accessibility, and it may significantly reduce mass transfer limitations.

In this PhD thesis, ordered mesoporous silica and titania films with a thickness of 100 to 400 nm were developed via an evaporation induced self assembly method on different substrates (glass, silicon, titanium). These polymer templated mesoporous silica films have a narrow pore size distribution and were synthesized with a wide range of pore sizes (2 to 8 nm). A new calcination protocol was developed which allows the complete removal of the surfactant at mild conditions. The thermal and hydrothermal stability of the films that were obtained with an ionic surfactant was improved by pH adjustment during hydrolysis and by Al incorporation. Microwave assisted hydrothermal synthesis of these ordered microporous films was also investigated in an attempt to reduce the synthesis time from several days to less than 10 hours.

The obtained thin films have been loaded with polymetallic nanoparticles with a size of 1 to 3 nm to specifically activate a selected functionality of complex organic molecules. Methods for the deposition and the stabilization of bi-metallic and tri-metallic clusters by adsorption onto the mesoporous thin films have been investigated. A “one pot” sol-gel synthesis of the mesoporous films with embedded colloidal nanoparticles was developed which eliminates an additional impregnation step and produces a uniform distribution of the active components throughout the mesoporous films.

Various experimental techniques such as ellipsometric porosimetry, XRD, 2D SAXS, XPS, SEM, and TEM have been applied to obtain insight in the physical and chemical phenomena that determine the performance as well as the stability of the thin films. The activity and the selectivity of the resulting catalytic thin films have been investigated in the batch and in the continuous mode in the hydrogenation of citral and phenylacetylene. The latter was done in a 10 m long micro capillary (i.d. 250 μm) with a catalytic thin film deposited onto its inner channel wall surface. It was shown that the selectivity towards the target product can be changed by varying the metal ratio in the bimetallic nanoparticles. The high stability of these catalytic thin films

allows their further implementation in fine chemicals synthesis using microstructured reactors.

Nanostructured Catalytic Films for Multiphase Microstructured Reactors

Samenvatting

De toepassing van microgestructureerde katalytische reactoren voor gas-vloeistofreacties vereist de ontwikkeling van nieuwe technieken voor het afzetten van katalytisch zeer actieve, dunne lagen op microgestructureerde oppervlakken. Deze katalytische, dunne lagen kunnen een porositeit hebben tot wel 50%. Toepassing van deze lagen beperkt de drukval over microreactoren in vergelijking met micro gepakte bedden, het zorgt voor een betere bereikbaarheid van de katalysator en het kan stofoverdrachtlimiteringen significant verminderen.

Het onderzoek in dit proefschrift behelst de ontwikkeling van geordende mesoporeuze silica- en titanialagen van 100 tot 400 nm dikte via de EISA (Evaporation Induced Self Assembly) methode op verschillende substraten zoals glas, silicium en titanium. Deze mesoporeuze silicalagen werden gesynthetiseerd via een polymeer sjabloon en bezitten een nauwe poriediameterverdeling. Lagen met een brede reeks van poriediameters van 2 tot 8 nm zijn daarbij bereid. Een nieuw calcineringsprotocol werd ontwikkeld waarmee het mogelijk is het oppervlak-actieve polymeer te verwijderen onder milde omstandigheden. De thermische en hydrothermale stabiliteit van de lagen, verkregen via het gebruik van ionogeen, oppervlak-actief polymeer, is verbeterd door het aanpassen van de pH bij de hydrolyse en door het inbouwen van aluminium in de laag. In een poging de benodigde synthesetijd te reduceren van enige dagen tot minder dan 10 uur werd ook onderzoek gedaan naar de hydrothermale synthese van de geordende microporeuze lagen met behulp van microgolfstraling.

De verkregen lagen werden beladen met polymetallische nanodeeltjes met afmetingen tussen 1 en 3 nm om specifiek een geselecteerde functionaliteit van complexe, organische moleculen te activeren. Er werd onderzoek uitgevoerd naar methoden voor het afzetten en stabiliseren van bi- en trimetallische clusters via adsorptie op mesoporeuze dunne lagen. Een “één-pots” synthese van de mesoporeuze lagen met ingebouwde, colloïdale nanodeeltjes werd ontwikkeld. Deze synthese elimineert een additionele impregnatiestap en leidt tot een uniforme verdeling van de actieve componenten in de mesoporeuze laag.

Verschillende experimentele technieken zoals ellipsometrische porosimetry, XRD, 2D-SAXS, XPS, SEM en TEM werden toegepast om inzicht te verwerven in de fysische en chemische verschijnselen die zowel de katalytische activiteit als de stabiliteit van de dunne lagen bepalen. De activiteit en de selectiviteit van de resulterende katalytische lagen zijn zowel in batch- als in continubedrijf onderzocht

in de hydrogenering van citral en phenylacetyleen. De laatste reactie werd uitgevoerd in een 10 m lang capillair met een inwendige diameter van 250 μm, waarbij een katalytische dunne laag was afgezet op de binnenwand van het capillair. De selectiviteit naar het gewenste product bleek te kunnen worden veranderd door variatie van de metaalverhouding in de bimetallische nanodeeltjes. De hoge stabiliteit van deze katalytische dunne lagen maakt verder gebruik mogelijk in microgestructureerde reactoren voor fijn-chemische synthese.

Chapter 1

Introduction

Chip- and capillary-based microreactor research for fine chemicals synthesis is a rapidly growing field worldwide following the realization of the benefits of microfluidic technology over conventional chemical synthesis. These include improved temperature control, enhanced selectivity, and both environmental and safety benefits resulting from the use of small quantities of reagents and solvents [1]. Development of microstructured catalytic reactors for multiphase (gas-liquid) reactions on a solid catalyst deposited on channel walls is a focal direction in process intensification, which requires new techniques for incorporation of porous catalytic thin films onto structured surfaces. These catalytic thin films prevent high pressure drop, enhance catalyst accessibility and eliminate mass transfer limitations. In order to increase the amount of deposited catalytic materials, the thin layers of porous materials such as (i) amorphous ordered mesoporous silicas with pore networks having different symmetry groups, (ii) ordered mesoporous organosilicas with various surface functional groups, (iii) amorphous carbons with ordered mesopores, (iv) ordered mesoporous (mixed) metal oxides, and (v) micro- and mesoporous zeolites, have been developed. For application in structured reactors, significant efforts have also been carried out to synthesize mesoporous silicas with various shapes: coatings/films, foams, fibers, monoliths, and spheres [2].

The first part of this PhD thesis is focused on the sol-gel synthesis of micro- and mesoporous silica films on various substrates by an evaporation induced self assembly (spin-coating and dip-coating) and hydrothermal methods. The microwave assisted hydrothermal synthesis of ordered microporous films was also investigated in an attempt to reduce the synthesis time from several days to less than 10 hours. Since many catalytic applications involve elevated temperatures and non-aqueous

solvents, the thermal and hydrothermal stability of these materials was improved by a pH adjustment during hydrolysis and by Al incorporation. The film properties were investigated by different experimental characterization techniques such as ellipsometric porosimetry, XRD, 2D SAXS, SEM, TEM, and TGA. The second part of the thesis is devoted to the development of the methods to load polymetallic nanoparticles with a size of 1 to 3 nm into the micro- and mesoporous thin films to specifically activate a selected functionality of complex organic molecules, which are intermediates in fine chemical production. The true bimetallic character of the embedded nanoparticles was confirmed by XPS. The activity and selectivity of the resulting catalytic thin films have been investigated in the batch and continuous mode in the hydrogenation of α,β-unsaturated aldehydes to the unsaturated alcohols and alkynes to alkenes. The latter was done in a 10 m long microchannel (i.d. 250 μm) operated in the annular flow regime with a catalytic thin film deposited onto the inner surface. In the annular regime, the gas flows in the center of the tube, while the liquid flows along the channel wall as a liquid film. In microchannels, the small thickness of this liquid film does not create any resistance to hydrogen transfer from the gas core through the film to the catalyst. Therefore, reactions always occur in the kinetic regime, which allows fast catalyst optimization.

1.1 Microstructured reactors

1.1.1 Catalytic multiphase microstructured reactors

Catalytic gas phase [3], and multiphase (liquid-liquid [4] and gas-liquid [5]) reactions can be performed in microreactors. The production of a large number of fine chemicals, particularly in the field of flavour and fragrance chemistry and pharmaceuticals, involves selective hydrogenation as a critical step. In these gas-liquid-solid reactions, the overall production rate is often limited by inter-phase mass transfer. Such multi-phase reactions can be performed in microchannels or microcapillaries with a catalytic thin film deposited on the channel wall. The superiority of immobilized and deposited catalytic films on microreactor channels

over packed-bed microreactors has previously been reported [6]. The efficient use of such microstructured reactors requires an enhancement of the internal reactor surface by deposition of nanostructured (micro- or mesoporous) catalytic films onto the walls of the reactor channels. Both types of thin films reduce the pressure drop along the microchannels while diffusion into catalytic sites occurs faster in mesoporous films. This thesis will be devoted to the development of catalytic microreactors with nanostructured thin films for gas-liquid hydrogenation reactions.

Various two phase (gas-liquid) flow regimes can be realized in microchannels (Figure 1.1) to control the residence time and the liquid hold-up and therefore the selectivity in consecutive hydrogenation reactions. In a complementary PhD project [7], various flow regimes have been studied and it was demonstrated that a catalytic reaction always proceeds in the kinetic regime under both slug and annular flow. Therefore, the main concern is to develop thin catalytic coatings to avoid internal mass transfer limitation in the porous structure. As the diffusion of large organic molecules in the porous network is much slower as compared to that observed in gas phase reactions, the maximum coating thickness in fast hydrogenation reactions should not exceed 1 μm to avoid internal mass transfer limitations at moderate catalyst loadings (1-2 wt.%).

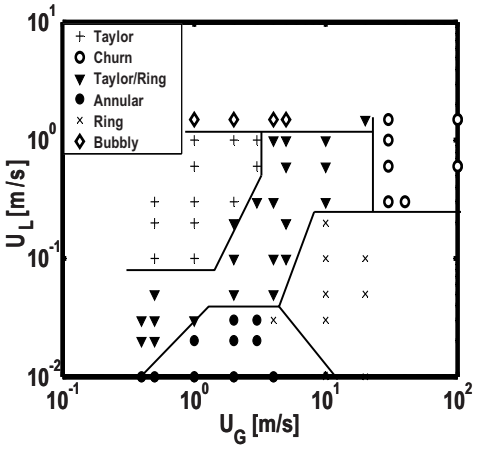

Figure 1.1. A typical flow regime map for an isopropanol/nitrogen system in a 2 cm rectangular microfluidic channel with a cross-section of 100 x 50 μm² [7].

The maximum layer thickness to prevent internal mass transfer limitation can be determined according to:

$$\varphi = d_{cat}\sqrt{\frac{k_v}{D_{eff}}} < 0.1 \tag{1.1}$$

where φ is the Thiele modulus (dimensionless) which designates the pore diffusion (internal) limitation [8], d_{cat} is the maximum catalytic film thickness to avoid internal mass transfer limitation, k_v is the reaction rate coefficient per unit volume of support, and D_{eff} is the effective diffusivity in mesoporous structures.

Deposition of catalytic materials on structured surfaces can be done via sol-gel methods. Usually, deposition on open and plane surfaces is carried out by spin-coating while deposition onto the inner surface of capillaries/microchannels is performed by dip-coating. Deposition of a catalyst on plane surfaces should be followed by polishing steps to remove the undesired coated surfaces for subsequent sealing. Deposition of a catalyst in capillaries can be done by applying vacuum on one side and sucking the solution from the other side [9]. Compatibility between catalytic coatings and incorporation techniques on the reactor materials is the main issue in many catalytic microreactor studies [5].

1.1.2 Reactor material choice and modification

The choice of substrate materials for the microreactor depends to a great extent on: (i) the surface hydrophilicity of the substrates, (ii) the material restrictions on the manufacturing side; (iii) the need for fast development in the testing phase; (iv) the corrosion activity of the substrate in the expected chemical environment, and (v) the possible interaction between the substrate components and the catalyst leading to quicker catalyst deactivation.

Glass, fused silica, silicon, metals and metal alloys are most common materials applied for construction of microstructured reactors. Metal and alloy substrates are, however, not compatible with many fine chemical synthesis applications. Borosilicate glass and fused silica seem to be ideal substrates for thin film deposition in low-temperature liquid phase chemical synthesis. They contain a relatively high

concentration of surface hydroxyl groups, have high corrosion a resistance and are chemically inert towards many organic molecules. Furthermore, microchannels with a precise control of both the cross-section and the surface roughness can be easily etched in glass by dry reactive ion etching. Fused silica capillaries are already applied in many chromatographic applications and are readily available on the market.

The adhesion between the nanostructured films and the substrates (silicon, glass, fused silica) depends on the substrate surface roughness and its hydrophilicity. At high wetting angles between the substrate surface and the synthesis solution, the adhesion of the resulting films is weak to encounter shear stress which appears under flow conditions in microchannels. As the chemical and mechanical stability of thin films play a very important role in microreactor applications, substrate modification was adapted and optimized in many studies [10,11].

Good adhesion between thin films and substrates can be obtained by increasing the interfacial interactions by using a hydrophilic oxide layer and by the formation of hydrogen or covalent bonds. A 15 nm layer of a hydrophilic layer of titania deposited by e.g. atomic layer deposition [12] increases adhesion [13,14]. The titania layer can be made super-hydrophilic by means of UV irradiation. TiO_2 is irradiated with UV-photons to create reversible molecular defects on the TiO_2 film surface. Photon energy is absorbed by the TiO_2 surface where it releases an electron and a positive hole is formed on the spot. When two holes meet, this leads to an oxygen vacancy which dissociatively adsorbs a water molecule in the form of a hydroxyl group [15]. By formation of two hydroxyl groups at the surface of the TiO_2 support, the surface becomes more hydrophilic. These hydroxyl groups act as the binder between the porous thin films and the support. Thus, an increase of the number of surface hydroxyl groups induces a better adhesion between the inorganic film and the support.

The mechanical stability of amorphous mesoporous oxide films depends on their porous structure and the character of the interface between the film and the

substrate [10]. In that sense, a rougher interface provides a stronger adhesion which prevents delamination of the films.

1.2 Ordered mesoporous silica films

Following the discovery of ordered mesoporous oxide materials (OMOMs), ordered mesoporous oxide films (OMOFs) were developed as potential inorganic catalyst supports with controlled porosity [16-25]. Ordered mesoporous silicas (OMSs) have attractive properties such as a high specific surface area, a large volume of mesopores, adjustable diameters of primary pores with narrow pore size distribution, as well as tailorable surface properties and morphology [26-28]. Ordered micro- and mesoporous silica films (OMSFs) are the potential host matrices to support metal and metal oxide nanoparticles which also allows to grow other nanostructured materials such as carbon nanotubes [29]. They are also applied in electrochemical [30], biology and medicine [31], and lab-on-a-chip applications [32], and as sensors [33].

Similar to mesoporous M41S materials, OMSFs are synthesized with cationic surfactants as structure directing agents [25]. Their framework of ordered hexagonal one-dimensional pores with adjustable well-defined size from 2 to 10 nm allows loading metal nanoparticles with controlled size [34,35]. A high specific surface area of these materials of 800-1000 m^2/g and a high concentration of terminal silanol groups (in the range of 1 to 2 OH per nm^2) facilitates high metal loadings [36].

The drawback of the mesoporous oxide materials templated by ionic surfactants is their poor (hydro)thermal stability because of their thin amorphous silica pore walls of about 0.5 to 1.5 nm. Ordered silicas with large (> 5 nm) cage-like mesopores (SBA-15 and 16) and thicker pore walls of 3 to 7 nm, can be synthesized using commercially available block copolymers as structure-directing agents. These materials have a higher thermal stability than that of MCM-41 cage-like OMSs with a cubic *Pm3n* structure that can also be synthesized using large alkylammonium surfactants [37]. The pore diameters of SBA-15 and SBA-16 are modifiable between about 6 to 15 nm depending on the type of structure directing agent and the

synthesis conditions. Another significant and unique feature of polymer templated OMSs is the presence of complimentary porosity (mainly micropores) in the amorphous siliceous walls. These complementary pores interconnect adjacent mesopores and differentiate these materials from ionic surfactant-templated OMSs.

1.2.1 Synthesis of ordered mesoporous silica films

Currently, the self-assembly synthesis of large channel-like polymer templated OMSs with a hexagonal (*P6mm* symmetry) structure as well as large pore cage-like OMSs with a body-centered cubic (*Im3m* symmetry) structure, is well established. OMSs are synthesized using a combination of self-assembly (self-organization of surfactant micelles or block copolymers) and sol-gel processes involving hydrolysis and condensation of alkoxysilanes according to the well known chemistry (Equations 1.2 to 1.4) [38-44]:

$$\equiv \text{Si-OR} + \text{H}_2\text{O} = \equiv \text{Si-OH} + \text{R-OH} \quad (1.2)$$

$$\equiv \text{Si-OR} + \equiv \text{Si-OH} = \equiv \text{Si-O-Si} \equiv + \text{R-OH} \quad (1.3)$$

$$\equiv \text{Si-OH} + \equiv \text{Si-OH} = \equiv \text{Si-O-Si} \equiv + \text{H}_2\text{O} \quad (1.4)$$

where R is an alkyl group.

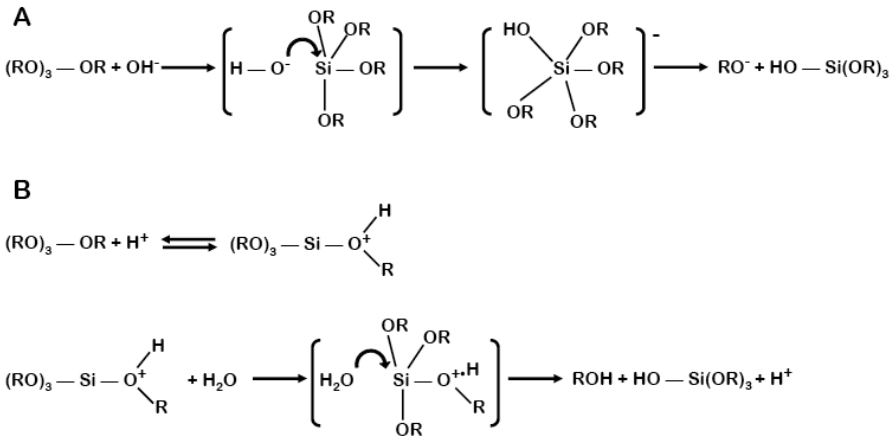

Figure 1.2. Mechanism of the base- or acid- catalyzed hydrolysis and condensation of alkoxysilanes, panels A and B, respectively [45].

The base process proceeds via nucleophilic substitution of the alkoxide (RO-) by the OH^- group. The acid process involves the reversible protonation of the alkoxy group and the subsequent nucleophilic substitution of either the silanol or H_2O (see Figure 1.2, panels A and B, respectively). The hydrolysis of the first alkoxy group is believed to be a rate limiting step and the remaining alkoxy groups hydrolyze fast with the subsequent condensation of $Si(OH)_4$ [45,46].

Therefore, the hydrolysis and condensation can be presented as:

$$Si(OR)_4 + 4\ H_2O = Si(OH)_4 + 4\ R\text{-}OH \text{ (hydrolysis)} \quad (1.5)$$

$$n\ Si(OH)_4 = n\ SiO_2 + 2n\ H_2O \text{ (condensation)} \quad (1.6)$$

where R is an alkyl group.

In the case of OMSFs synthesized at high pH, an aqueous or alcoholic ammonia solution is employed, whereas an aqueous HCl solution is typically used at low pH. The most popular silica precursors used to obtain OMSFs are tetraethyl orthosilicate (TEOS) and sodium metasilicate. When TEOS is used, the alkyl group (R) in chemical reactions (1.2 to 1.6) is C_2H_5 and the by-product (R-OH) is ethanol.

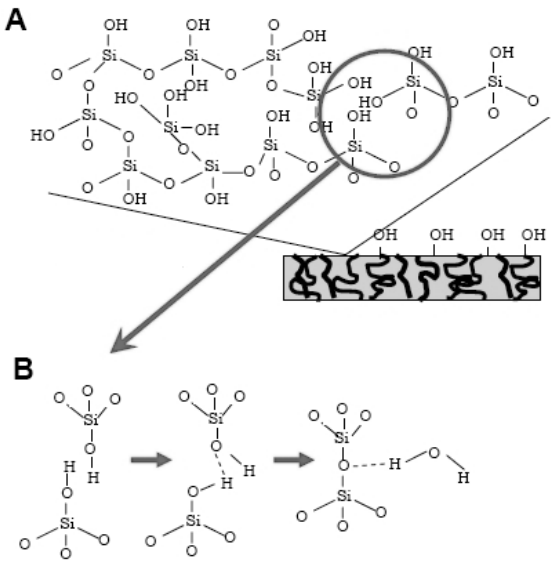

Figure 1.3. Graphical representation of siliceous walls and the surface of OMSs (panel A) and dehydration/dehydroxylation of silica (panel B) [55, 56].

The resulting OMSFs possess amorphous silica walls: a polysiloxane network composed of siloxane bridges (Si-O-Si) with silanol groups sticking-out from the wall surface (SiO_2(s)-OH), as shown in Figure 1.3A. These hydrophilic surface groups can be removed (at least partially) via dehydration and/or dehydroxylation by a temperature treatment above 473 K (Figure 1.3B). Generally, a typical supramolecular-templated synthesis of OMSFs can be considered as a two-step process. The first step involves the self-assembly of silica and template species (hydrolysis and condensation of silica species in the presence of the surfactant, solvent and co-solvent). The second step involves the consolidation of the siliceous amorphous pore walls. Many attempts have been made to control the experimental conditions in both synthesis steps (pH, acid concentration, salt addition) as well as to optimize the temperature and the synthesis time in order to perform fine-tuning of the properties of the resulting materials [47-54].

1.2.2 Evaporation induced self assembly via dip-coating and spin-coating

The self-assembly of functional nanocomposite films is induced by means of evaporation which regulates the increase of the concentration and the micellisation of the surfactant molecules. The properties of the mesostructure of silica films depend on the synthesis and deposition parameters including the relative humidity (RH) which defines the evaporation rate and the stabilization of the hybrid films [57]. It is well-known that the self-assembly of inorganics taking place under acidic synthesis conditions is a highly co-operative mechanism between both the organic and inorganic phases through charge density matching variation in a sol-gel process. The final mesostructure is a function of various parameters such as the surfactant/metal precursor ratio [57-58], pH value, evaporation rate spinning rate, and relative humidity [18-20,57].

The spinning rate is important as the solvent evaporation happens rapidly (10–30 s) during spinning, enriching the silica oligomers in the films. At the same time, the surfactant is reaching the critical micelle concentration and finally an ordered mesostructure is formed. The aging time of the initial solution is also critical

to the final mesostructure. Both 3D hexagonal and cubic mesostructures can be obtained by variation of the aging time. The 3D hexagonal mesostructure is mainly obtained from the solution with aging times between 2 and 24 h, whereas the cubic mesostructure is obtained with longer aging times up 72 h. Another processing parameter which influences the thin film quality is the relative humidity during the spin coating process and after deposition in the stabilization period. Different mesophases can be obtained by changing the relative humidity from 20 to 80% [18, 19, 57].

1.2.3 Development of calcination protocol

The calcination treatment consists of the further stabilization of the inorganic network and the gently removal of the structure templating agent. Beside complete template removal, the calcination procedure results also in the consolidation of the porous structure (dehydration and dehydroxylation of siliceous walls and surface, respectively, see Figure 1.3B), accompanied by some shrinkage and/or in some cases collapse of the structure upon elevated temperature. There are a limited number of published studies concerning the specific removal of the organic surfactant. Among them are plasma and supercritical fluid extraction [59], solvent extraction [60], ozone treatment [61], and photocalcination using UV-light in vacuum [62]. Removal of the surfactant from the inorganic–organic composite materials after synthesis is generally conducted via calcination in an air flow at temperatures above 723 K. However, this procedure leads to film distortion or even crack formation because of the considerable amount of internal stress generated by the film shrinkage and due to the different linear expansion coefficients of the thin films and the substrate. Removal of the template by calcination results in a higher degree of structural contraction in the thin films obtained by EISA as compared with those obtained by hydrothermal synthesis. Therefore, the main challenge is to reach complete surfactant removal at relatively mild conditions. The heating rate during the thermal treatment should be adjusted to control the template removal and to prevent crack formation.

1.2.4 Stability enhancement

The factors governing the thermal stability of ordered mesoporous silica films (OMSFs) are still not fully elucidated. Thermal and hydrothermal stability of OMSFs is one of the most important properties from the viewpoint of their prospective applications in microstructured reactors. Since many OMSFs exhibit rather low hydrothermal stability, numerous research activities have been undertaken to identify the conditions suitable for the synthesis of hydrothermally stable OMSFs and to elaborate effective methods to stabilize the OMSF structures. The mesoporous structure needs to be preserved during the thermal treatment step often followed by catalyst impregnation steps. A catalytic reaction is usually performed in an organic solvent. Until now, all stability studies have been performed with mesoporous material powders.

Thermal stability can be improved by an increase of the pore wall thickness [37,63,64], or by the proper introduction of aluminium heteroatoms [65,66]. The collapse of mesoporous silica in the presence of water or in polar solvents with active hydrogen atoms, involves the rupture and hydrolysis of siloxane bridges [67]. Therefore, to compromise the integrity of the framework, a larger number of siloxane groups needs to be hydrolyzed in highly condensed materials. Similarly, in the case of thicker walls, a thicker layer should be dissolved by hydrolysis of siloxane bridges to disintegrate the framework. Mesoporous materials with enhanced hydrothermal stability can be obtained using procedures that increase the degree of silica framework cross-linking [68-70], the thickness of the silica walls [37,68], or using those providing reduced amounts of hydroxyl groups [72]. The latter can be achieved by high temperature calcination [71], or by hydrophobic vapour treatment [72]. A higher density of the silica framework can be obtained by the addition of organic or inorganic salts during the synthesis [73-75], by pH adjustment [76], or/and by incorporation of aluminium [67,77,78].

1.2.5 Microwave assisted hydrothermal synthesis

Hydrothermal sol-gel synthesis is a very efficient method to synthesize microporous thin films on different microstructured substrates. In an effort to combine the robust stability of crystalline zeolites with the larger pores of mesoporous silica, mesoporous zeolites have been synthesized by secondary growth after seeding the substrates with nanocrystals or by adding an amphiphilic organosilane surfactant to the conventional synthesis mixture [79-83]. The resulting pore diameters are similar to those in OMSs with amorphous frameworks [79]. However, the long synthesis times and the high alkalinity of the synthesis mixture can lead to partial substrate dissolution in case of glass and silicon substrates.

To overcome these problems, the microwave-assisted hydrothermal synthesis (MAHys) of ordered micro- and mesoporous silicas has gradually gained popularity [84,85]. Microwave irradiation assures a rapid and homogeneous heating of the entire solution and enhances the crystallization rates of zeolites. Although in-depth theoretical knowledge of microwave interactions with matter is still at an initial stage of development, there is a great interest in the microwave-assisted synthesis of nanostructured thin films due to the aforementioned advantages of this method. Microwave assisted hydrothermal synthesis (MAHyS) with NH_4F as mineralizing agent results in a highly crystalline zeolite Beta (91% crystallinity) after 8 hours of microwave heating at 423 K [86]. Titanosilicate (ETS-4) thin films were successfully synthesized by microwave heating at 508 K within 50 min [87].

The coupling of microwave heating with a hydrothermal synthesis requires application of special non-polar substrate materials such as quartz, pure aluminium oxide (corundum), or special glass types. While these are not exotic materials for making microreactors and indeed have been applied for laboratory prototypes, there is presently no clear methodology how to perform sol-gel synthesis of microporous thin films on such substrate materials. An approach for the development of glass based microstructured devices is to utilize the intrinsic properties of glass through application of thin protective films, consisting of more alkali-resistant materials, e.g.

zirconia, on the glass surface. The wettability can be improved by surface treatments or by deposition of a titania hydrophilic film by ALD, as described in section 1.1.2.

1.2.6 Incorporation of mono and polymetallic nanoparticles in porous oxide films.

Despite a large diversity of methodologies available for deposition of an active component onto support materials, the reproducible preparation of catalytic thin films in microchannels remains a crucial requirement in the fabrication of these multiphase microfluidic devices. The main challenges are: (i) to obtain high loadings of active metal component at high dispersion, (ii) to provide high accessibility of active nanoparticles by the reactants, (iii) to ensure a long term stability of the nanoparticles during reactor operation, (iv) to have a possibility to control the stoichiometry of bimetallic nanoparticles, and (v) the method should provide a possibility for scaling-up towards multiple channels.

In this sense, the prior preparation of bimetallic nanoparticles that can be subsequently deposited on a selected support is seen as a suitable alternative to conventional methods since both composition and particle size can be controlled [88,89]. Colloidal nanoparticles can be synthesized using a polyol reduction method [90], such that the synthesized nanoparticles protected by a polymer, that prevents the aggregation of nanoparticles in solution, are dispersed in a solvent. Then, the pre-formed shielded nanoparticles are embedded in the pores of mesoporous materials during cooperative self-assembly. The direct incorporation of air-stable nanoparticles into the mesoporous inorganic matrix of a thin film delivered on the internal surface of a fused silica capillary was recently reported [91]. The nanoparticles retain their small particle size even after calcination, and are accessible for reaction thereafter. The nanoparticles can also be incorporated into the hydrophobic core of templated micelles [92]. With the recent advancement in colloidal chemistry, nanoparticles can even be incorporated into liquid crystalline phases. In these ordered systems, the efficiency of doping is maximal when the particle diameter is less than two-third of the liquid crystal spacing [93].

The properties of nanoparticle confinement in mesoporous materials are the main factor determining their activity and selectivity [94-97]. Usually, high loadings of highly dispersed nanoparticles can only be obtained on a support with a large specific surface area [98]. The precise control of the size and the stoichiometry of embedded nanoparticles allow exploring their size effect on their activity and selectivity in different reactions [95,97,101-102]. Recent advances in nanotechnology have also been applied to design well controlled catalytic nanoparticles with known chemical composition [97,98]. Analysis of the synthesis of nanoparticles by the polyol reduction method [90] and the mixed metal cluster synthesis [99-100] are well documented in the literature, however they are beyond the scope of this work.

1.2.7 Selectivity control by the stoichiometry of polymetallic nanoparticles

Platinum-rhenium and platinum-tin bimetallic catalysts have attracted great interest because of their superior properties in a variety of important processes [102,103]. The electropositive metal is supposed to release electronic density to the noble metal. The electropositive metal becomes electron-deficient and can preferentially accommodate, e.g. carbonyl groups of multifunctional substrates through their nucleophilic oxygen atom. Therefore, hydrogenation of α,β-unsaturated aldehydes to the unsaturated alcohols has often been applied as a model reaction to test the performance of bimetallic supported catalysts. In case of diffusion limitations or strong adsorption on the catalyst surface, the resulting unsaturated alcohol or partially saturated aldehyde can be hydrogenated at its remaining unsaturated bonds to yield the saturated alcohol. Cis-trans isomerization or several other types of side reactions, such as cyclization or acetalization should be suppressed. The probability to hydrogenate either the C=C or the C=O bond of the unsaturated aldehydes, which governs the final selectivity to the unsaturated alcohol, depends critically on the mode of adsorption of the molecule [104], which in turns depends on the electron-donating species (either the second metal or the support) interacting with the metal particles to improve the selectivity to the unsaturated alcohol.

The structure of the metal nanoparticles encaged in the micro- or mesoporous films, where most of the atoms are interacting with the surface of the support framework, is very sensitive to any change in the acid-base properties of the support. Therefore the selectivity to the unsaturated alcohols of the monometallic nanoparticles encaged in the microporous materials (e.g. zeolites) can be enhanced as the acidity of micro- or mesoporous materials is decreased. It was reported that the presence of species generated upon reduction at high temperature of the reducible TiO_2 support, leads to catalysts active and highly selective to the hydrogenation of the carbonyl bond [105].

Selective hydrogenation of terminal alkynes to alkenes represents another type of reactions where bimetallic catalysts encaged into mesoporous supports can be applied. It is possible to fine-tune the alkene adsorption strength via bimetallic composition [91]. At an optimum metal ratio the strong alkyne adsorption prevents adsorption of the alkene. As a result, the alkene leaves the surface immediately rather than to stay on it being further hydrogenated.

1.3 Research objectives and the layout of the thesis

The main objective of this study is to demonstrate full selectivity control of chemical reactions by total structure uniformity of microstructured catalytic reactors at multiple length scales (Figure 1.4). First of all, on the *nanoscale*, by obtaining polymetallic clusters with a narrow particle size distribution, controlled stoichiometry, and required metal loadings. Then, on the *microscale* by synthesizing only a thin micro- or mesoporous film onto the reaction channels to perform reactions in the kinetic regime avoiding internal diffusion limitations. Finally, on the *macroscale*, by maintaining the narrow residence time distribution in a microchannel [106-111].

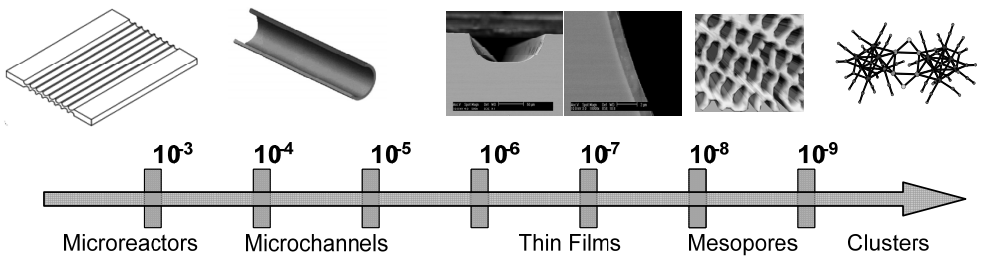

Figure 1.4. Full reaction control by total structure uniformity at multiple length scales.

A significant part of the research is devoted to the synthesis of ionic surfactant templated ordered micro- and mesoporous silica films (OMSFs) and to the improvement of their thermal stability and stability in non aqueous solvents. In ***Chapter 2***, the effect of Al incorporation and pH adjustment during hydrolysis of the silica precursor on the thermal and structural stability of ordered microporous silica films with a 2D structure is presented. The stability of aluminium incorporated silica films is examined in several organic solvents with different polarity. The optimum Al/Si ratio which shows the smallest d-spacing shift after solvent has been identified. The stability of the microporous films is further tested in the hydrogenation of phenyl acetylene performed in a batch reactor.

The deposition of polymer templated mesoporous silica thin films with hexagonal and cubic structures by evaporation induced self assembly method onto microchannel walls is discussed in ***Chapter 3***. The microchannels with a depth of 50 μm and with different aspect ratios (width/depth) in the range from 2 to 5 were produced by dry reactive ion etching in a borosilicate glass substrate. The width to depth ratio between 2 (semi-circular) and 3 (semi-oval) provides the most uniform thickness of the mesoporous silica films over the channel cross-section.

The synthesis of polymer templated mesoporous thin films and the development of adsorption methods to deposit bimetallic (Pt-Sn) mixed-metal cluster precursors onto OMSFs, are presented in ***Chapter 4***. The effect of different synthesis parameters such as the surfactant/silica ratio, the aging time and the spinning rate during spin-coating are studied. In the proposed approach, the functionality of the

relatively fragile metallic clusters is accommodated through the rigid inorganic framework providing protection and by the 3D distribution of the catalytic function to provide better catalyst dispersion.

In ***Chapter 5***, the microwave assisted hydrothermal synthesis of microporous zeolitic films via secondary growth is presented. The effect of synthesis time, temperature and template to alumina ratio on the morphology of the thin zeolitic films is investigated. Stable zeolite Beta films with a thickness of ca. 1-2 μm are synthesized on a glass substrate. Prior to the synthesis, a protective layer of zirconia is deposited on the substrate to prevent dissolution of the substrates in a highly alkaline synthesis mixture. Then, the hydrophilicity of the substrates is increased by the deposition of a thin titania layer. The quality of the protective zirconia layer determines the success of the subsequent sol-gel synthesis.

The activity and selectivity in citral hydrogenation of monometallic Pt nanoparticles embedded in different micro- and mesoporous supports (Pt-H-Y zeolite, Pt-SAPO-5, Pt-MCM-41) with different acidity are described in ***Chapter 6***. The interplay between steric limitations caused by pore morphology and acidity on selectivity has been studied. H-SAPO-5 was the most selective support for hydrogenation towards the unsaturated alcohols with a selectivity of 57% at a conversion level of 46%. The unique combination of a monosized pore diameter, weak Brønsted acidity, and a large Pt particle size contributed to a high selectivity.

The potential of efficiently integrating thin film technology with colloidal and cluster chemistry to produce different mesoporous matrices that can host a variety of mono- bi- and tri-metallic nanoparticles is discussed in ***Chapter 7***. The clusters and colloidal nanoparticles are incorporated onto mesostructured silica films with different methods of incorporation and tested in the hydrogenation of citral in a microchannel operating under annular flow conditions. The stability of the mesostructured silica films in the tested reactions is evaluated.

Finally, in ***Chapter 8*** the main conclusions derived from the previous chapters were summarized together with an outlook to extra large surface area microsystems.

References

[1] P. Watts, S.J. Haswell, *Chem. Soc. Rev.* 34 (2005) 235-246

[2] N. Shimura, M. Ogawa, *J. Colloid Interface Sci*. 303 (2006) 250-255.

[3] V. Hessel, S. Hardt, H. Löwe, A. Müller, G. Kolb, *Chemical Micro Process Engineering Vol. 1 and 2,* Wiley-VCH, Weinheim 2005.

[4] B.P. Mason, K.E. Price, J.L. Steinbacher, A.R. Bogdan, D.T. McQuade, *Chem. Rev.* 107 (2007) 2300–2318.

[5] J. Kobayashi, Y. Mori, K. Okamoto, R. Akiyama, M. Ueno, T. Kitamori, S. Kobayashi, *Science* 304 (2004) 1305–1308.

[6] J. Bravo, A. Karim, T. Conant, G.P. Lopez, A. Datye, *Chem. Eng. J.* 101 (2004) 113-121.

[7] (a) V. Haverkamp, V. Hessel, H. Lowe, G. Menges, M.J.F. Warnier, E.V. Rebrov, M.H.J.M. de Croon, J.C. Schouten, M.A. Liauw, *Chem. Eng. Technol*. 29 (2006) 1015–1026. (b) M.J.F. Warnier, E.V. Rebrov, M.H.J.M. de Croon, V. Hessel, J.C. Schouten, *Chem. Eng. J*. 135 (2008) S153-S158.

[8] O. Levenspiel Chemical Reactor Engineering, John Wiley and Sons Inc., New York, 3rd Ed., 1999.

[9] H. Chen, L. Bednarova, R.S. Besser, W.Y. Lee, *Appl. Catal., A* 286 (2005) 186-195.

[10] F. Mammeri, E. Le Bourhis, L. Rozes, C. Sanchez**,** *J. Mater. Chem.* 15 (2005) 3787-3811.

[11] C.M. Yang, A.T. Cho, F.M. Pan, T.G. Tsai, K.J. Chao, *Adv. Mater.* 13 (2001) 1099-1102.

[12] S.B.S. Heil, P. Kudlacek, E. Langereis, R. Engeln, M.C.M. van de Sanden, W.M.M. Kessels, *Appl. Phys. Lett*. 89 (2006) 131505-1-131505-3.

[13] (a) S. Eichenlaub, C. Chan, S.P. Beaudoin, *J. Colloid Interface Sci.* 248 (2002) 389-397. (b) S. Eichenlaub, A. Gelb, S.P. Beaudoin, *J. Colloid Interface Sci*. 280 (2004) 289-298.

[14] (a) B.A. Latella, M. Ignat, C. Barbe, D.J. Cassidy, H, Li, *J. Sol-Gel Sci. Tech*. 31 (2004), pp. 143-149. (b) D.P. Birnie III, *J. Sol-Gel Sci. Tech*. 31 (2004) 225-228.

[15] (a) R. Wang, K. Hashimoto, A. Fujishima, M. Chikuni, E. Kojima, A. Kitamura, M. Shimohigoshi, T. Watanabe, *Nature* 388 (1997) 431-432. (b) M. Miyauchi, A. Nakajima, A. Fujishima, K. Hashimoto, T. Watanabe, *Chem. Mater*. 12 (2000) 3–5. (c) R. Wang, N. Sakai, A. Fujishima, T. Watanabe, K. Hashimoto, *J. Phys. Chem. B* 103 (1999) 2188–2194.

[16] (a) M. Ogawa, *J. Chem. Soc. Chem. Commun*. (1996) 1149–1150. (b) M. Ogawa, T. Igarashi, K. Kuroda, *Bull. Chem. Soc. Jpn*. 70 (1997) 2833–2837.

[17] D. Kundu, H.S. Zhou, I. Honma, *J. Mater. Sci. Lett*. 17 (1998) 2089–2092.

[18] D. Grosso, F. Cagnol, G.J. de A.A. Soler-Illia, E. L. Crepaldi, H. Amenitsch, A. Brunet-Bruneau, A. Bourgeois, C. Sanchez, *Adv. Funct. Mater*. 14 (2004) 309-322.

[19] D. Zhao, P. Yang, N. Melosh, J. Feng, B.F. Chmelka, G.D. Stucky, *Adv. Mater.* 10 (1998) 1380–1385.

[20] Y. Lu, R. Gandguli, C. Drewien, *Nature* 389 (1997) 364–368.

[21] H. Yang, N. Coombs and G.A. Ozin, *J. Mater. Chem***.** 8 (1998) 1205–1211.

[22] C.A. Alberius, K.L. Frindell, R.C. Hayward, E.J. Kramer, G. Stucky, *Chem. Mater.* 14 (*2002*) 3284–3294.

[23] (a) J.M. Berquier, L. Teyssedre, C. Jacquiod, *J. Sol-Gel. Sci. Technol*. 13 (1998) 739–742. (b) A. Chougnet, C. Heitz, E. Søndergard, J.M. Berquier, P.A. Albouy. M. Klotz , *J. Mater. Chem.* 15 (2005) 3340-3345. (c) A. Chougnet, C. Heitz, E. Søndergard, P.-A. Albouy. M. Klotz, *Thin Solid Films* 495 (2006) 40-44.

[24] C.J. Brinker, Y. Lu, A. Sellinger, H. Fan, *Adv. Mater*. 11 (1999) 579–585.

[25] (a) J.S. Beck, J. C. Vartuli, W. J. Roth, M. E. Leonowicz, C. T. Kresge, K. D. Schmitt, C. T. W. Chu, D. H. Olson, E. W. Sheppard, *J Am. Chem. Soc.* 114 (1992) 10834–10843. (b) C.T. Kresge, M.E. Leonowicz, W.J. Roth, J.C. Vartuli, J.S. Beck, *Nature* 359 (1992) 710–712.
[26] D.E. De Vos, M. Dams, B.F. Sels, P.A. Jacobs, *Chem. Rev.* 102 (2002) 3615-3640.
[27] Y. Liu, T.J. Pinnavaia, *J. Mater. Chem*. 12 (2002) 3179-3190.
[28] T. Linssen, K. Cassiers, P. Cool, E.F. Vansant, *Adv. Colloid Interface Sci.* 103 (2003) 121-147.
[29] D. Barreca, W.J. Blau, G.M. Croke, F.A. Deeney, F.C. Dillon, J.D. Holmes, C. Kufazvinei, M.A. Morris, T.R. Spalding, E. Tondello, *Micropor. Mesopor. Mater*, 103 (2007) 142-149.
[30] D.F. Fattakhova-Rohlfing, J. Rathouský, Y. Rohlfing, O. Bartels, M. Wark, *Langmuir* 21 (2005) 11320-11329.
[31] D.F. Fattakhova-Rohlfing, M. Wark, J. Rathouský, *Chem. Mater.* 19 (2007) 1640–1647.
[32] R. Fan, S. Huh, R. Yan, J. Arnold, P. Yang, *Nature Mater*. 7 (2008) 303-307.
[33] G. Walters, I.P. Parkin, *J. Mater. Chem*. 19 (2009) 574-590.
[34] F. Goettmann, C. Sanchez, *J. Mater. Chem*. 17 (2007) 24–30.
[35] T. Maschmeyer, F. Rey, G. Sankar, J.M. Thomas, *Nature* 378 (1995) 159-162.
[36] J.M. Thomas, R. Raja, R. *ChemInform*, 36, (2005) 163-211.
[37] (a) D. Zhao, J. Feng, Q. Huo, N. Melosh, G. Fredrickson, B. Chmelka, G. Stucky, *Science* 279 (1998) 548–552. (b) D. Zhao, Q. Huo, J. Feng, B.F. Chmelka, G.D. Stucky, *J. Am. Chem. Soc.* 120 (1998) 6024–6037.
[38] C.J. Brinker, *G*.W. Scherer *Sol-gel science and technology* (*1989),* New York, USA: Academic Press.
[39] J.Y. Ying, C.P. Mehnert, M.S. Wong, *Angew. Chem. Int. Ed*. 38 (1999) 56–77.
[40] U. Ciesla, F. Schüth, *Micropor. Mesopor. Mater*. 27 (1999) 131–149.
[41] C.J. Brinker, *J. Non-Cryst. Solids* 100 (1988) 31-50.
[42] C.J. Brinker, K.D. Keefer, D.W. Schaefer, R.A. Assink, B.D. Kay and C.S. Ashley, *J. Non-Cryst. Solids* 63 (1984) 45-59.
[43] C.J. Brinker, G.W. Scherer, Sol-Gel Science: The Physics and Chemistry of Sol-Gel Processing, Academic Press, Inc.: New York, 1990.
[44] R.K. Iler, The Chemistry of Silica, Wiley: New York, 1979.
[45] S.L. Chen, P. Dong, G.H. Yang, J.J. Yang, *Ind. Eng. Chem. Res.* 35 (1996) 4487-4493.
[46] G.H. Bogush, C.F. Zukoski, *J. Colloid Interface Sci*. 142 (199) 1-18.
[47] P.F. Fulvio, S. Pikus, M. Jaroniec, *J. Colloid Interface Sci.* 287 (2005) 717-720.
[48] P.F. Fulvio, S. Pikus, M. Jaroniec, *J. Mater. Chem*. 15 (2005) 5049-5053.
[49] C. Yu, B. Tian, J. Fan, G.D. Stucky, D. Zhao, *Chem. Commun*. (2001) 2726-2727.
[50] J.R. Matos, M. Kruk, L.P. Mercuri, M. Jaroniec, L. Zhao, T. Kamiyama, O. Terasaki, T.J. Pinnavaia, Y. Liu, *J. Am. Chem. Soc*. 125 (2003) 821-829.
[51] M Kruk, J.R. Matos, M. Jaroniec, *Colloids Surf. A* 241 (2004) 27-34.
[52] R.M. Grudzien, M. Jaroniec, *Stud. Surf. Sci. Catal.* 156 (2005) 105-112.
[53] T.W. Kim, R. Ryoo, M. Kruk, K.P. Gierszal, M. Jaroniec, S. Kamiya, O. Terasaki, *J. Phys. Chem. B* 108 (2004) 11480-11489.
[54] J. Fan, C. Yu, J. Lei, Q. Zhang, T. Li, B. Tu, W. Zhou, D. Zhao, *J. Am. Chem. Soc. 127* (2005) 10794-10795.
[55] T.M.H. Costa, M.R. Gallas, E.V. Benvenutti, J.A.H. da Jornada, *J. Non-Cryst. Solids* 220 (1997) 195-201.
[56] K.W. Gallis, C.C. Landry, *Adv. Mater*. 13 (2001) 23-26.

[57] C. Sanchez, C. Boissière, D. Grosso, C. Laberty, L. Nicole, *Chem. Mater*. 20 (2008) 682-737.
[58] A. Thomas, F. Goettmann, M. Antonietti, *Chem. Mater*. 20 (2008) 738–755.
[59] S. Kawi, M.W. Lai, *Chem. Commun*. (1998) 1407-1408.
[60] Z.-L. Hua, J.-L. Shi, L. Wang, W.-H. Zhang, *J. Non-Cryst. Solids* 292 (2001) 177-183.
[61] M.T.J. Keene, R. Denoyel, P.L. Llewellyn, *Chem. Commun*. (1998) 2203-2204.
[62] A. Hozumi, Y. Yokogawa, T. Kameyama, K. Hiraku, H. Sugimura, O. Takai, M. Okido, *Adv. Mater*. 12 (2000) 985-987.
[63] R. Mokaya, *J. Mater. Chem*. 12 (2002) 3027-3033.
[64] R. Mokaya, *Chem. Commun*., (2001) 933-934.
[65] A.S. O'Neil, R. Mokaya, M. Poliakoff,. *J. Am. Chem. Soc.* 124 (2002) 124, (36), 10636-10637.
[66] R. Mokaya, *ChemPhysChem.* 3 (2002) 360-363.
[67] (a) S.C. Shen, S. Kawi, *J. Phys. Chem. B* 103 (1999) 8870-8876. (b) K. Cassiers, T. Linssen, M. Mathieu, M. Benjelloun, K. Schrijnemakers, P. Van Der Voort, P. Cool, E.F. Vansant, *Chem. Mater.* 14 (2002) 2317–2324.
[68] F. Zhang, Y. Yan, H. Yang, Y. Meng, C. Yu, B. Tu, D. Zhao, *J. Phys. Chem. B* 109 (2005) 8723-8732.
[69] R. Mokaya, *J. Phys. Chem. B 103* (1999) 10204-10208.
[70] R. Ryoo, J. Kim, *J. Chem. Soc. Chem. Commun*., (1995) 711-712.
[71] J.D. Bass, D. Grosso, C. Boissiere, E. Belamie, T. Coradin, C.Sanchez, *Chem. Mater*. 19 (2007) 4349–4356.
[72] N. Nishiyama, S. Tanaka, Y. Egashira, Y. Oku, K. Ueyama, *Chem. Mater*., 14 (2002) 4229-4234.
[73] R. Ryoo, J.M. Kim, C.H. Ko, C.H. Shin, *J. Phys. Chem.* 100 (1996) 17718-17721.
[74] R. Ryoo, S. Jun, *J. Phys. Chem. B* 101 (1997) 317-320.
[75] D. Das, C.-M. Tsai, S. Cheng, *Chem. Commun*. 5 (1999) 473-474.
[76] J.M. Kim, S. Jun, R. Ryoo, *J. Phys. Chem. B 103* (1999) 6200-6205.
[77] Y. Han, F.-S. Xiao, S. Wu, Y. Sun, X. Meng, D. Li, S. Lin, F. Deng, X. Ai, *J. Phys. Chem. B* 105 (2001) 7963-7966.
[78] (a) Mokaya, R., *J. Phys. Chem. B* 104 (2000) 8279-8286. (b) R. Mokaya, *Chem. Commun*., (2000b) 1541-1542. (c) R. Mokaya, *Chem. Comm*., (2001) 633-634. (d) R. Mokaya, *Chemphyschem*., 4 (2002) 360-363.
[79] M. Choi, H.S. Cho, R. Srivastava, C. Venkatesan, D.H. Choi, R. Ryoo *Nature Mater*. 5 (2006) 718-723.
[80] (a) W. Fan, M.A. Snyder, S. Kumar, P.S. Lee, W.C. Yoo, A.V. McCormick, R.L. Penn, A. Stein, M. Tsapatsis, *Nature Mater.* 7 (2008) 984-991. [b] K. Yamamoto, T. Tatsumi, *Chem. Mater*. 20 (2008) 972–980.
[81] L. Tosheva, V.P. Valtchev, *Chem. Mater*. 17 (2005) 2494-2513.
[82] K. Egeblad, C.H. Christensen, M. Kustova, C.H. Christensen, *Chem. Mater*. 20 (2008) 946–960.
[83] J. Pérez-Ramírez, C. H. Christensen, K. Egeblad, C. H. Christensen, J.C. Groen, *Chem. Soc. Rev.* 37 (2008) 2530-2542.
[84] G.A. Tompsett, W.C. Conner, K.S. Yngvesson, *ChemPhysChem*, 7 (2006) 296-319.
[85] M. Nuchter, B. Ondruschka, W. Bonrath, A. Gum, *Green Chemistry* 6 (2004) 128-141.
[86] D.-S. Kim,. J.-S. Chang, J.-S. Hwang,. S.-E. Park, J.M. Kim, *Micropor. Mesopor. Mater.* 68 (2004) 77-82.
[87] D. Coutinho, J.A. Losilla, K.J. Balkus Jr, *Micropor. Mesopor. Mater.* 90 (2006) 229-236.

[88] R.W. Wunder, J. Philips, *J. Phys. Chem*. 100 (1996) 14430.
[89] H. Bönnemann, R.M. Richards, *Eur. J. Inorg. Chem*. (2001) 2455.
[90] (a) P. Lu, T. Teranishi, K. Asakura, M.Miyake, N. Toshima, *J. Phys. Chem. B* 103 (1999) 9673-9682. (b) S. Dominguez-Dominguez, A. Berenguer-Murcia, A. Linares-Solano, D. Cazorla-Amoros, J. Catal. 257 (2008) 87-95. (c). S. Domínguez-Domínguez, Á. Berenguer-Murcia, D. Cazorla-Amorós, A. Linares-Solano, J. Catal. 243 (2006) 74-81.
[91] E.V. Rebrov, A. Berenguer-Murcia, H.E. Skelton, B.F.G. Johnson, A.E.H. Wheatley, J.C. Schouten, *Lab Chip* 9 (2009) 503-506.
[92] J.L. Gu, J.L. Shi, L.M. Xiong, H. Chen, M. Ruan, *Micropor. Mesopor. Mater*. 74 (2004) 199-204.
[93] L. Ramos, P. Fabre, *Langmuir* 13 (1997) 682–686.
[94] A.J. Gellman, N. Shukla, *Nature Mater.* 8 (2009) 87-88.
[95] S.H. Joo, J.Y. Park, C.K. Tsung, Y. Yamada, P. Yang, G.A. Somorjai, *Nature Mater*. 8 (2009) 126-131.
[96] (a) A.T. Bell, *Science* 299 (2003), pp. 1688-1691. (b) J. Grunes, J. Zhu, G.A. Somorjai, *Chem. Comm.*, (2003) 2257-2260.
[97] K. Wikander, A.B. Hungria, P.A. Midgley, A.E.C. Palmqvist, K. Holmberg, J.M. Thomas, *J. Colloid Interface Sci*. 305 (2007) 204-208.
[98] J. Kobler, T. Bein, *ACS Nano*, 2 (2008) 2324–2330.
[99] T. Gacoin, S. Besson, J.P. Boilot, *J. Phys. Condens. Mater.* 18 (2006) S85–S95.
[100] S. Costacurta, L. Malfatti, P. Innocenzi, H. Amenitsch, A. Masili, A. Corrias, M.F. Casula, *Micropor. Mesopor. Mater*. 115 (2008) 338-344.
[101] R. Narayanan, M.A. El-Sayed, *Top. Catal*. 47 (2008) 15–21.
[102] F. Klasovsky, P. Claus, Metal nanoclusters in catalysis: effects of nanoparticle size, shape and structure, in Metal nanoclusters in catalysis and materials science: the issue of size-control, Part I (B. Corain, G. Schmid, N. Toshima, Eds.), Elsevier 2008, 167-183.
[103] J.M. Thomas, R. Raja, *Stud. Surf. Sci. Catal*. 148 (2004) 163.
[104] F. Delbecq, P. Sautet, *J. Catal*. 220 (2003) 115-126.
[105] P. Reyes, M.C. Aguirre, G. Pecchi, J.L.G. Fierro, *J. Mol. Catal. A* 164 (2000) 245-251.
[106] (a) Y. Kemmochi, M. Hu, Y. Murakami, Y. Tsuji, M. Ogura, S. Maruyama, T. Okubo, *Trans Mater. Res. Soc. Jpn.* 30 (2005) 341-344. (b) B. Louis, C. Subrahmanyam and L. Kiwi-Minsker, B. Viswanathan, P.A., Buffat, A. Renken, *Catal. Commun.* 3 (2002) 159-163
[107] N. Ishigami, H. Ago, Y. Motoyama, M. Takasaki, M. Shinagawa, K. Takahashi, T. Ikuta, M. Tsuji. *Chem. Commun.*, 2007, 1626–1628.
[108] S. Kataoka, A. Endo, A. Harada, Y. Inagi, T. Ohmori, *Appl. Catal., A* 342 (2008) 107–112.
[109] V. Meille, *Appl. Catal., A*.315 (2006) 1-17.
[110] K. Haas-Santo, M. Fichtner, K. Schubert, *Appl. Catal., A* 220 (2001) 79-92.
[111] G. Germani, P. Alphonse, M. Courty, Y. Schuurman, C. Mirodatos, *Catal. Today* (2005) 114-120.
[112] R. Zapf, C. Becker-Willinger, K. Berresheim, H. Bolz, H. Gnaser, V. Hessel, G. Kolb, P. Lob, A.-K. Pannwitt, A. Ziogas, *Trans. IChemE*. 81 (2003) 721-729.
[113] E.V. Rebrov, G.B.F. Seijger, H.P.A. Calis, M.H.J.M. de Croon, C.M. van den Bleek, J.C. Schouten, *Appl. Catal., A* 206 (2001) 125-143.
[114] T.R. Dietrich, A. Freitag, R. Scholz, *Chem. Eng. Technol*. 28 (2005) 477-483.

Chapter 2

Enhancement of the stability of microporous silica films in non-aqueous solvents at elevated temperature

This Chapter is adapted from:
O. Muraza, E.V. Rebrov, M.H.J.M. de Croon, J.C. Schouten, Enhancement of the stability of micro porous silica films in non-aqueous solvents at elevated temperature, *Micropor. Mesopor. Mater*. 124 (2009) 20-29.

Abstract

The effect of Al incorporation and pH adjustment during hydrolysis of the silica precursor on the thermal and structural stability of ordered microporous silica films with a 2D structure is presented. The structural stability of the films was determined from a combination of LA XRD/TEM data with porosity data obtained from ethanol adsorption isotherms. Thermogravimetric analysis and FTIR data were used to determine the template removal and the thermal stability. The stability of aluminium incorporated silica films has further been examined in several organic solvents with different polarity. A solvent with a higher polarity interacts more strongly with the films; the long-order structure disappeared after exposure to polar solvents. After exposure to non-polar solvents, the pore size uniformity was retained after 48 h. The samples with an Al/Si ratio of 0.007 showed the smallest d-spacing shift after exposure to hexane. The stability was further tested in the hydrogenation of phenyl acetylene performed in a batch reactor over 1 wt.% Pd/Si(Al)O_2/Si (Al/Si=0.007) films at 303 K and 10 bar H_2 with hexane as solvent. No deactivation was observed in two subsequent hydrogenation runs.

2.1 Introduction

Ordered micro- and mesoporous silica films (OMSFs) with an ultrahigh specific surface area (800-1200 m^2/g) and a tunable pore size have a large potential as a catalyst support in structured reactors (e.g. microchannels, monoliths and foams) in processing of large organic molecules, which are usually intermediates in the production of fine chemicals. Since many applications involve elevated temperatures and non-aqueous environments, there is a great interest and demand for the study of thermal stability of OMSFs and their stability in non-aqueous solvents. The OMSFs possess amorphous silica walls which can be represented as polysiloxane networks composed of siloxane bridges (Si-O-Si) with silanol groups sticking-out from the wall surface. These hydrophilic surface groups can be removed, at least partially, via dehydroxylation by temperature treatment above 473 K [1]. The mesoporous structure needs to be preserved during the thermal treatment step often followed by catalyst impregnation steps and a catalytic reaction usually performed in an organic solvent. Until now, all stability studies have been performed with mesoporous material powders. Their hydrothermal stability was reported for at least 48 hours in boiling water. Later studies suggested that the SBA-15 silicas are stable in boiling water for at least 72 h [2,3] but not more than 6 days [4-7].

It is well-known that the self-assembly taking place under the acid synthesis conditions is highly co-operative between both the organic and inorganic phases through charge density matching variation in a sol-gel process for the synthesis of mesoporous silica thin films. The resulting film structure of thin films can be influenced by different synthesis parameters, such as CTAB/TEOS ratio [8-11], relative humidity [12], and calcination conditions [8,11-14]. The effect of pH adjustment on the properties of thin films was not investigated so far.

The factors governing the thermal stability of OMSFs are still not fully elucidated. Thermal stability can be improved by an increase of the pore wall thickness [15,16], or the proper introduction of aluminium heteroatoms [17,18]. The collapse of mesoporous silica in the presence of water or in polar solvents with active hydrogen atoms, involves the rupture and hydrolysis of siloxane bridges [19,20].

Therefore, to compromise the integrity of the framework, a larger number of siloxane groups needs to be hydrolyzed in highly condensed materials. Similarly, in the case of thicker walls, a thicker layer should be dissolved by hydrolysis of siloxane bridges to disintegrate the framework. The degradation process proceeds faster in a solution containing nucleophilic species [21]. Mesoporous materials with enhanced hydrothermal stability can be obtained using procedures that increase the degree of silica framework cross-linking [22-24], the thickness of the silica walls [22,25], or with reduced amounts of hydroxyl groups [26]. The latter can be achieved by high temperature calcination [27,28], or by hydrophobic vapour treatment [26]. A higher density of the silica framework can be obtained by addition of organic or inorganic salts during the synthesis [29-21], by repeated pH adjustment [32], or/and incorporation of aluminium [20,33,37]. The most stable mesoporous silica materials contain heteroatoms (mainly aluminium) on their surface [38-42] or in their framework [15,19,34-37,43-45]. The degradation rate of the materials with an Al/Si ratio of 0.11 was 30 times slower than that of the all-silica film [21].

The aluminium grafting on the outer domain gave a better protection than grafting deeper in the inorganic framework. The mesoporous materials with an Al/Si ratio of 0.02 were reported to provide a higher hydrothermal stability than those with an Al/Si ratio of 0.10 [34-36]. At low Al/Si ratios, aluminium is grafted on the pore surface or into the outer region of the wall. As the aluminium content increased, the extra aluminium moved into the interior of the mesoporous wall rather than being incorporated directly in the silica network [37].

On the other hand, the aluminium incorporation into the silica network can negatively influence the long-order structure of mesoporous materials [46-48]. As the Al/Si ratio increases from 0.014 to 0.031, the long-order structure decreases with simultaneous decrease of the d-spacing from 3.91 to 3.22 nm. An interaction between the charged surfactant molecules and the framework aluminium sites caused contraction of the mesoporous structure [34-36]. It should also be noted that Brønsted and Lewis acid sites are formed in modified silica materials as a result of aluminium incorporation. This results in a controllable ion exchange capacity and acidic

properties [49], which should be taken into account when these materials will be used in catalysis.

The main objective of this work was the assessment and improvement of the thermal and hydrothermal stability of ordered mesoporous silica films with a 2D mesostructure in non-aqueous solvents. The effect of Al incorporation on enhancement of the stability will be presented. A combination of LA XRD/TEM data with porosity data obtained from ethanol adsorption isotherms has been chosen in this study for the assessment of the structural stability. Thermogravimetric analysis and FTIR have been used to study the template removal and thermal stability.

2.2 Experimental

2.2.1 Synthesis mixture preparation

Silicon and titanium substrates of 1 cm x 1 cm were used in this study. Prior to the synthesis, the titanium substrates were treated in several steps to increase their surface roughness as described elsewhere [50] for a better adhesion of thin films.

Solution A was prepared by dissolving tetraethylorthosilicate (TEOS, 99 wt.%, Merck) in 1-propanol (>99.5 wt. %, Fluka) followed by adding distilled water and HCl (Fluka). Then, solution A was stirred for 1 h followed by addition of 2-butanol (99 wt.%, Aldrich) and stirring of the resulting solution for 30 min. After that solution A was preheated to 333 K and aluminium tri-sec-butoxide (ATSB, 97 wt.%, Aldrich) was added and the resulting solution was stirred for 10 min. The Al content (x) was varied in the range of 0-0.020. The acid amount (y) in solution A was varied in the range of $2.0 \cdot 10^{-4}$ to $8.0 \cdot 10^{-4}$. The highest water amount of 3.52 corresponds to the highest acid amount of $8.0 \cdot 10^{-4}$ and vice versa. The surfactant solution was prepared separately by dissolving cetyl trimethyl ammonium bromide (CTAB, 95 wt.%, Aldrich) in distilled water. The CTAB solution was added to solution A and the resulting solution with a molar composition of 1 TEOS: 6.48 1-propanol: 2.64 2-butanol: 0.15 CTAB: x ATSB: 9.84 H_2O: y HCl was aged for 2 h at room temperature.

Series Si-pH samples were synthesized by the above method, while others (Si-A series) were synthesized by introducing a step for pH adjustment to 2.0 during

hydrolysis of the silica precursor. In the synthesis of Si-pH series samples, the acid amount was fixed at a H^+/Si ratio of $4.0 \cdot 10^{-4}$. In the synthesis of Si-A series samples, a 0.1 M HCl solution was added dropwise to maintain the pH at a desired value which was controlled by a pH meter.

For catalytic tests, palladium nanoparticles were incorporated into the synthesis solution by using a polyvinyl pyrrolidone stabilized 1-propanol suspension of colloidal Pd nanoparticles (4 nm in diameter) in 1-propanol instead of pure 1-propanol. The concentration of Pd nanoparticles was selected in order to obtain a 1 wt.% Pd loading in the micro porous silica film.

All as-synthesized films were first dried at room temperature for 12 h in a glove box with a relative humidity (RH) of 80%. Drying and calcination were performed in an oven at a residual pressure of 15 mbar. The heating rate from 298 to 573 K was 1 K/min with a 1-hour dwelling time every 25 K below 473 K, a 2-hour dwelling time at 498, 523 and 548 K, and a 4-hour dwelling time at 573 K.

2.2.2 Characterization

2.2.2.1 Ellipsometric porosimetry

Ellipsometric Porosimetry (EP) was used to determine the mesopore volume and the pore size distribution. The pore volume was determined from the change in the effective refractive index in the range of 400-1200 nm. The refraction index of the dry (without ethanol) micro porous film (n_M) and the total non-porous fraction (f_M) were calculated from the change in the effective refraction index (n_{ef}) at the end points of the isotherm using the Bruggeman effective medium approximation (BEMA, Eq. 2.1) and the refraction indexes of air and ethanol (n_m = 1.00 and 1.361 at 633 nm, respectively):

$$f_M \frac{n_M^2 - n_{ef}^2}{n_M^2 + 2n_{ef}^2} + (1 - f_M) \frac{n_m^2 - n_{ef}^2}{n_m^2 + 2n_{ef}^2} = 0 \qquad (2.1)$$

The porous fraction ($1 - f_M$) was determined from n_{ef} with the BEMA model at zero ethanol pressure by fitting the volumetric fraction of the inorganic framework with the air refraction index for the second material (n_p =1).

The isotherm was determined by fitting the volumetric fractions of the inorganic component (f_M), ethanol (f_{ET}), and air with the BEMA model at each relative pressure (Eq. 2.2):

$$f_M \frac{n_M^2 - n_{ef}^2}{n_M^2 + 2n_{ef}^2} + f_{ET} \frac{1.361^2 - n_{ef}^2}{1.361^2 + 2n_{ef}^2} + (1 - f_{ET} - f_M) \frac{1.00 - n_{ef}^2}{1.00 + 2n_{ef}^2} = 0 \quad (2.2)$$

Subsequently, the ethanol volume adsorbed (V_{ET}) is related to the product of the total film volume (V_F), the pore fraction ($1–f_M$), and the volumetric fraction of the ethanol saturated film (f_{ET}):

$$V_{ET} = V_F (1 - f_M) f_{ET} \quad (2.3)$$

Ethanol adsorption/desorption measurements were carried out at 287 K over a wide range (10^{-4} - 0.995) of relative pressures (p/p_0). The details of the sample pretreatment procedures are described elsewhere [51]. Structural parameters of the materials studied were determined from the desorption branch of the isotherm using an improved Derjaguin – Broekhoff - de Boer model (IDBdB) with cylindrical pores [52]. The Kelvin condensation model is widely used for the characterization of porous structures, especially for mesoporous solids, while a few authors have reported its underestimation of the pore size in the nanometer region [52,53]. Therefore, the IDBdB model was applied which takes into account both the thickness of the ethanol film measured on a similar non-porous substrate and the deviation in ethanol surface tension in the mesopores from that of a flat interface. This approach eliminates uncertainties related to the application of the statistical film thickness determined via *t*-plots in previous versions of the IDBdB model.

The specific surface area was calculated from ellipsometry data as:

$$S_{BET} = \frac{\sigma_L \cdot N_A}{\upsilon_L} \frac{f_{BET}}{\rho_{ET}} \quad (2.4)$$

where $\sigma_L = 1.091 \left(\frac{M_L}{\rho_{LF} N_A} \right)^{2/3}$ is the surface occupied by the ethanol molecule [54], with M_L the molar mass of the adsorbate (ethanol), ρ_{LF} the density of the sorbed ethanol

($\rho_{LF} = 0.803\,\rho_{ET}$), and N_A is the Avogadro number. υ_L is the molar volume of ethanol ($\upsilon_L = 5.82 \cdot 10^{-5}$ m^3/mol) and ρ_{ET} is the density of the liquid ethanol, and

$$f_{BET} = \frac{\frac{n_{BET}^2 - 1}{n_{BET}^2 + 2} - \frac{n_0^2 - 1}{n_0^2 + 2}}{\frac{1.361^2 - 1}{1.361^2 + 2}} \tag{2.5}$$

where n_0 and n_{BET} are the effective refractive indices of the empty film and of the film after filling of the mesopores with ethanol, respectively.

2.2.2.2 Low-Angle X-Ray Diffraction (LA-XRD) and 2D Small Angle X-ray Scattering (2D SAXS)

The phase composition was determined by X-ray diffraction in the range of 2-9° 2θ, using step scanning at 0.02° 2θ per step size and a counting time of 1 or 10 s for each step. XRD data were collected on a Rigaku Geigerflex Max/B diffractometer (40 kV, 40 mA) with Cu Kα radiation. The mesopore diameter was calculated from the geometrical relation $D_p = cd_{100}\sqrt{\frac{\rho V_p}{1+\rho V_p}}$, developed for hexagonal mesostructures. In this equation, c = 1.213, ρ is the density of the walls (ρ = 2.2 g/cm^3 for calcined samples), d_{100} is the (100) lattice spacing, and V_P is the mesopore volume obtained from ellipsometric porosimetry measurements (V_p = V_{ET} at p/p$_0$ after capillary condensation, see section 2.1).

The morphology of the coatings was determined by two-dimensional small angle X-ray scattering (2D SAXS) measurements. 2D SAXS experiments were performed with a rotating anode X-ray generator (copper anode, small focus, wavelength: λ = 0.15418, focus size: 0.2 x 0.2 mm^2, power: 50 kV, 20 mA) and equipped with two adjustable optical systems. The optics consisted of two parabolic multilayer graded mirrors at right angles. It delivers a well-defined and intense parallel monochromatic beam. The sample was on a rotation stage and the diffraction patterns were recorded onto photo-sensitive imaging plates. Vacuum pipes are inserted between the sample and the imaging plate to reduce air scattering.

A grazing incidence geometry can also be used and the sample was allowed to oscillate by a few degrees during exposure.

2.2.2.3 Transmission Electron Microscopy

The morphology of the films was determined by High Resolution Transmission Electron Microscopy (HR-TEM) using a FEI Tecnai TF20 electron microscope operated at 200 kV. Samples were mounted on a Quantifoil® microgrid carbon polymer supported on a copper grid by dropping the sample suspension on the grid. The particle size distribution (PSD) was obtained by measuring 100 particles from the HR-TEM micrographs. The mean particle diameter was calculated by the following formula: $d_m = \frac{1}{100}\sum_{i=1}^{100} n_i d_i$, where n_i is the number of particles with diameter d_i.

2.2.2.4 TG-DTA analysis

The thermogravimetric analysis combined with differential thermal analysis was performed on a Q500 TGA/DTG instrument. 5 to 10 mg of the as-synthesized films (S-A) were scratched from the substrate. The measurements were carried out under nitrogen flow under ambient atmosphere in the range of 298 to 823 K with a heating rate of 10 K/min.

2.2.2.5 FTIR measurements

Fourier Transmission Infrared Spectroscopy (FTIR) was used to characterize the composition change of films during the calcination. FTIR was performed with a FTS 6000 Spectrometer equipped with a BIO-RAP Digilab division UMA-500 microscope in transmission mode. Spectra were recorded at 4 cm^{-1} spectral resolution, an undersampling ratio of 4, and a speed of 20 kHz.

2.2.3 Stability tests

Stability of silica films (S-pH, S-A-20Al) was assessed after exposure of the substrates in excess of different solvents (all received from Aldrich): methanol (99.8 wt.%), 2-propanol (99.5 wt.%), diethyl lether (99.7 wt.%), tetrahydrofuran (99.9 wt.%), hexane (95 wt.%), and dichloro methane (99.8 wt.%). The experiments were carried out at 293 K for 48 h under static conditions. The stability was also assessed under typical reaction conditions at elevated temperature and pressure. The hydrogenation of phenyl acetylene was chosen as a model reaction. In these experiments, ten substrate plates with micro porous films (film weight = 4.0 mg) were loaded with 1 wt.% Pd. These plates were fixed in a holder, which was placed in an autoclave reactor (Büchi). Prior to the reaction, the Pd/SiO_2 films were reduced in a H_2 flow at 773 K for 10 minutes. The reaction was performed at 303 K and 10 bar H_2 pressure with a 0.007 M solution of phenyl acetylene in hexane. Samples of 1 μl were selected for analysis after desired time intervals using a Rapid On Line Sample Injector system (ROLSI ™) [48] connected to a Varian 3800 gas chromatograph equipped with WCOT (30 m x 0.25 mm) and CP Sil 5CB DF columns and a FID detector.

All films are referred to according to the substrate type (Si stands for silicon substrate and Ti stands for titanium substrate), synthesis method (either constant pH (pH) or fixed amount of acid (A)), and their aluminium to silica ratio (Al/Si) multiplied by 1000. For example, a film obtained on a silicon substrate by the method with a fixed amount of acid at an Al/Si ratio of 0.020, is referred to as S-A-20Al hereafter. The samples modified with Pd nanoparticles are denoted Pd-X, where X stands for the sample name as given above.

2.3 Results and discussion

2.3.1 Effect of pH

To investigate the effect of pH during hydrolysis of the silica precursor on the wall thickness and pore volume of the resulting thin films, a method was applied with pH adjustment to different pH values in the range between 1.85 and 2.3 (Table 2.1, Figure 2.1). The XRD peaks tend to shift toward small angle and significant

narrowing of XRD peaks in the as-synthesized films is observed as the pH decreased from 2.3 to 2.0. The films synthesized at a pH of 2.1 show the largest d-spacing shift after calcinations (Figure 2.1 (b)), which reduces as the pH approaches the isoelectric point of silica (pH = 2) and then increases with further decrease in pH. This phenomenon can be explained by the changes in the rates of hydrolysis and condensation as the pH changes. At a pH of 2.3 and 2.10, the hydrolysis rate is rather slow and the films have a low degree of long-order structure as it can be seen from wider peaks in the XRD pattern. With increasing the pH, the condensation rate increases much faster than that of hydrolysis. At a pH of 2.0, the morphology is already fully controlled by the surface free energy which tends to be minimized resulting in the most compact geometrical arrangement of the sol particles. For the films synthesized with the pH below the isoelectric point of silica (pH < 2), the condensation rate increases even further, resulting in the formation of the irregularly oriented domains in the micro porous films as can be concluded from the broadening of the XRD peak in the as-synthesized films.

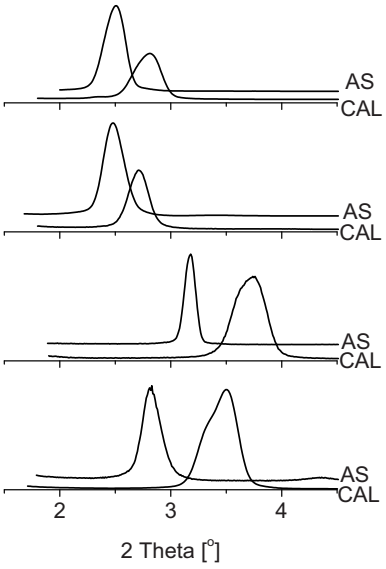

Figure 2.1. Small-angle X-ray diffraction patterns of the as-synthesized (AS) and calcined (CAL) microporous silica films obtained by adjusting the pH during hydrolysis of TEOS to different values: (a) 1.85, (b) 2.00, (c) 2.10, (d) 2.30.

Table 2.1. d-spacing, unit cell, mean pore diameter, pore wall thickness and d-spacing shift as a function of the Al/Si ratio in the micro porous silica films synthesized with pH adjustment.

pH	d_{100}-spacing (nm)		Lattice parameter[a] (nm)		FWHH[b] ($^{o}2\theta$)	Pore volume[c] (cm^3g^{-1})	Pore diameter[d] (nm)	Pore wall thickness[e] (nm)	d-spacing shift (%)
	AS	CAL	AS	CAL	AS	CAL	CAL	CAL	
1.85	3.12	2.52	3.60	2.91	0.21	0.420	1.47	1.44	19
2.00	2.77	2.35	3.20	2.71	0.13	0.360	1.26	1.45	15
2.10	3.56	3.26	4.11	3.76	0.25	0.390	1.83	1.93	8
2.30	3.52	3.14	4.07	3.62	0.24	0.404	1.79	1.83	11

[a] Lattice parameter from XRD data using the formula, $a_0 = \frac{2}{\sqrt{3}} d_{100}$

[b] Full Width at Half Height for the (100) peak

[c] Pore volume from ellipsometric porosimetry using the formula $V_p = V_{ET}$ at p/p_0 after capillary condensation, $V_{ET} = V_F(1 - f_M)f_{ET}$ (see Eq.2.3)

[d] Pore diameter from pore volume using the formula $D_p = cd_{100}\sqrt{\frac{\rho V_p}{1+\rho V_p}}$, where c = 1.213, ρ = 2.2 g/cm^3, V_p is determined from ellipsometric porosimetry

[e] Pore wall thickness = unit cell – pore diameter

It should be mentioned that an experimental error of ± 0.005 degree of 2-theta corresponds to a distance of ± 0.007 nm in the d-spacing. Therefore, the values of the d-spacing of 3.56 and 3.52 nm observed at pH of 2.10 and 2.30, respectively, are significantly different; while they are very close each other.

Similar results were reported in previous work [56], where films were prepared by dipcoating at fixed amounts of acid but at different aging times. The (100) peak in the as-synthesized samples was observed in the range of 2.4-2.9^{o} 2-theta and the best long-order structure was obtained after 6 days aging time. It was concluded that after this aging time, a desired charge density on silica species is achieved, which leads to the optimal dimensions and shape of the inorganic building blocks for the subsequent self-assembly process leading to a well-defined structure. Obviously, the pH has a similar influence on the composition of the synthesis mixture. By changing the pH, the rates of the hydrolysis and polycondensation reactions can be optimized to yield inorganic oligomers with a desired degree of branching at a pH of 2.0. This pH was used in the following experiments designed to improve the thermal stability of the micro porous films and their stability in non-aqueous solvents.

2.3.2 Aluminium incorporation

Ellipsometric porosimetry was applied to the characterization of the structural and surface properties of the porous thin films. This technique provides information about the specific surface area, pore volume, pore size distribution, and film thickness. The details obtained from this porosimetry study are listed in Table 2.2. Typical examples of the ethanol adsorption-desorption isotherms are shown in Figure 2.2 for S-A-5Al and S-pH-0.20Al, respectively.

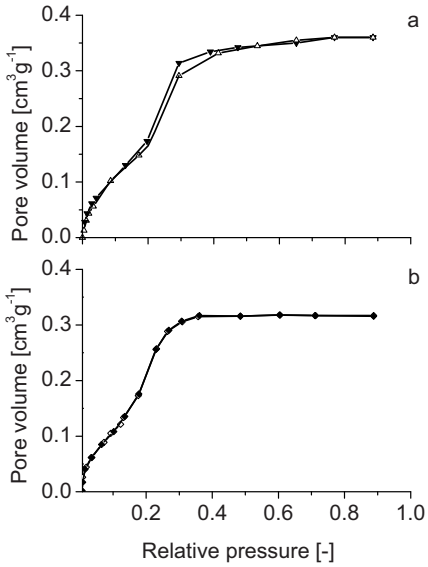

Figure 2.2. Ethanol adsorption-desorption isotherms of ethanol at 287 K on calcined samples (a) S-pH-2Al, (b) S-pH-10Al.

The isotherms are Type IV with/or without Type H1 hysteresis (parallel and close to vertical adsorption/desorption branches), which is a characteristic shape for porous materials comprised of long parallel channels. In comparison to block copolymer-templated materials, silica films templated with ionic surfactants do not exhibit the presence of complimentary microporosity in the amorphous siliceous walls. It can be seen from Figure 2.2(a) and (b) that a steep rise in the volume adsorbed was observed just from the beginning of the adsorption isotherm due to the spontaneous condensation in the monosized micropores. The total pore volume is lower for Al-containing films and it decreases with increase in Al content. This is in agreement with the results from earlier studies performed with powder materials [5,40-42]. No hysteresis was observed in the samples synthesized with the pH adjustment method which have a mean pore size below 1.3 nm. A narrow hysteresis loop for sample S-pH-20Al was in the p/p_0 range between 0.2 and 0.4, showing that a part of the pores has the size in the transition region between micro- and mesopores. The shape of the loop, when two curves are very close to each other, demonstrates that there are no any major constrictions in the pores.

Table 2.2. d-spacing, unit cell, mean pore diameter, pore wall thickness and d-spacing shift as a function of the Al/Si ratio in the micro porous silica films synthesized without pH adjustment and with pH adjustment to 2.0.

Al/Si molar ratio	d_{100}-spacing (nm)		Lattice parameter[a] (nm)		Pore volume[b] (cm^3g^{-1})	Pore diameter[c] (nm)	Pore wall thickness[d] (nm)	S_{BET}[e] ($m^2\ g^{-1}$)	d-spacing shift (%)
	AS	CAL	AS	CAL	CAL	CAL	CAL	CAL	
S-pH	2.77	2.35	3.20	2.71	0.360	1.26	1.45	1260	15
S-pH-2Al	2.76	2.38	3.19	2.75	0.342	1.24	1.51	1200	14
S-pH-3Al	2.67	2.43	3.08	2.81	0.326	1.23	1.58	1150	9.0
S-pH-4Al	2.62	2.44	3.03	2.82	0.323	1.23	1.59	1140	6.9
S-pH-5Al	2.61	2.45	3.01	2.83	0.317	1.22	1.61	1120	6.5
S-pH-10Al	2.59	2.14	2.99	2.47	0.294	1.02	1.45	1050	17
S-A	3.94	3.13	4.55	3.61	0.342	1.63	1.98	1190	21
S-A-2Al	3.81	3.16	4.40	3.66	0.326	1.60	2.06	1150	17
S-A-3Al	3.73	3.08	4.30	3.55	0.295	1.47	2.08	1040	17
S-A-7Al	3.65	2.99	4.21	3.46	0.276	1.37	2.09	978	18
S-A-10Al	3.58	2.90	4.13	3.35	0.257	1.27	2.08	913	19
S-A-20Al	3.56	2.92	4.11	3.38	0.248	1.25	2.13	882	18

[a] Lattice parameter from XRD data using the formula, $a_0 = \frac{2}{\sqrt{3}} d_{100}$

[b] Pore volume from ellipsometric porosimetry using the formula $V_p = V_{ET}$ at p/p_0 after capillary condensation, $V_{ET} = V_F(1 - f_M)f_{ET}$ (see Eq. 3)

[c] Pore diameter from pore volume using the formula $D_p = cd_{100}\sqrt{\frac{\rho V_p}{1+\rho V_p}}$, where c = 1.213, ρ = 2.2 g/cm³, V_p is determined from ellipsometric porosimetry

[d] Pore wall thickness = unit cell – pore diameter

[e] Surface area using the formula $S_{BET} = \frac{\sigma_L \cdot N_A}{\upsilon_L}\frac{f_{BET}}{\rho_{ET}}$, where σ_L is the surface occupied by ethanol molecule (σ_L = 0.276 nm²); N_A is the Avogadro number; f_{BET} is determined from ellipsometric porosimetry (see Eq.4) ; ρ_{ET} is the density of ethanol; υ_L is the molar volume of liquid ethanol at 287 K (υ_L = $5.82 \cdot 10^{-5}$ m³/mol).

The adsorption studies provide information about global properties of micro porous films, but it is not applicable for the assessment of structural ordering. For determination of the local film structure, several complimentary to EP techniques, such as small-angle X-ray diffraction (XRD), 2D small-angle X-ray scattering (SAXS), and scanning and transmission electron microscopy (SEM and TEM) were used.

The XRD patterns of the microporous silica films obtained by adjusting the pH during hydrolysis of TEOS, are shown in Figure 2.3, and those obtained by addition of a fixed acid amount are shown in Figure 2.4. X-ray diffraction patterns of all samples exhibit two well resolved peaks corresponding to (100) and (200) reflections in a hexagonal structure. Several samples (viz. S-pH, S-A, and S-A-2Al, see Figures 3(b), 4(b) and (d), respectively) demonstrate a shoulder which is assigned to (110) reflection. The *d*-spacing ratios of the (100), (110) and (200) diffraction peaks are calculated to be 1: $\sqrt{3}$: 2, which is in good agreement with the values expected for a 2D hexagonal structure (*P6mm*).

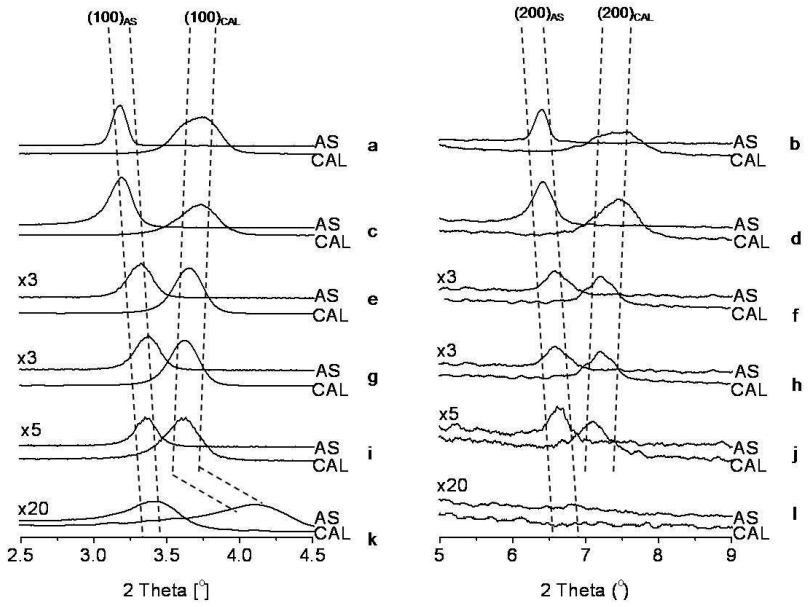

Figure 2.3. Small-angle XRD patterns of the as-synthesized (AS) and calcined (CAL) microporous silica films obtained by adjusting pH during hydrolysis of TEOS. Lower intensity peaks positioned in the range of 5-9° 2θ were enlarged to improve the clarity. (a,b) S-pH, (c,d) S-pH-2Al (e,f) S-pH-3Al, (g,h) S-pH-4Al, (i,j) S-pH-5Al, (k,l) S-pH-10Al.

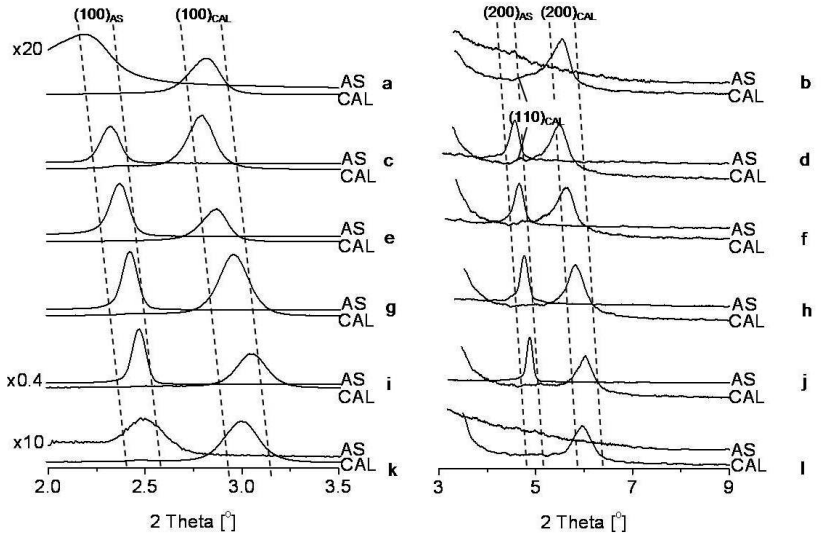

Figure 2.4. Small-angle XRD patterns of the as-synthesized (AS) and calcined (CAL) mesoporous silica films obtained by addition of a fixed acid amount. Lower intensity peaks positioned in the range of 3-9° 2θ were enlarged to improve the clarity. (a,b) S-A, (c,d) S-A-2Al (e,f) S-A-3Al, (g,h) S-A-7Al, (i,j) S-A-10Al, (k,l) S-A-20Al.

It is interesting to note that both the d_{100} value and the pore size of the films was by 15-25% smaller in the samples obtained at the fixed pH than those of the films obtained without the pH adjustment procedure. These results indicate that micro porous walls are considerably thinner in the samples obtained at fixed pH.

Upon calcination, the XRD lines shifted to higher 2-theta values indicating a significant lattice contraction. The lattice contraction monotonously reduced from 15 to 6.5% when aluminium was introduced into the synthesis mixture under pH adjustment in the range of Al/Si ratios from 0 to 0.005 (Figure 2.3 (a, c, e, g, and i)). The minimum d-spacing shift of 6.5% was observed for a highly ordered sample with an Al/Si ratio of 0.005 (Figure 2.3 (i, j)). Further increase of the Al content in the synthesis mixture resulted in films with a low long-order structure as it can be seen from the XRD patterns where the lines were severely broadened and lattice contraction was even higher than that in the corresponding all-silica samples (Figure 2.3 (k and l)). Contrarily, the samples obtained without pH adjustment demonstrated a rather constant lattice contraction of 17-21% which was not significantly affected by

the amount of aluminium introduced into the structure (Figure 2.4). The strongest peaks in the calcined films were observed at an Al/Si ratio of 0.007, demonstrating the highest degree of long order structure (Figure 2.4 (g) and (h)).

It should be noted that both the pore diameter as well as the structural order of the calcined films does not vary significantly with the variation of the Al/Si ratio in the range of 0.002-0.007. The structural ordering detected by X-rays refers to the network of periodic porosity and different density of walls and pores for ordered thin films with amorphous walls. Therefore, disappearance of a regular pattern from the densified walls is responsible for XRD peak broadening in the samples with high aluminium content.

This shows that the pH adjustment is a facile way to improve the thermal stability of ordered silica films. Additionally, the long order structure and thermal stability can be improved by addition of aluminium into the synthesis mixture corresponding to an Al/Si ratio of 0.005 or 0.007 without the pH adjustment procedure. These results on the thermal stability of micro porous silica films are similar to those earlier reported in literature for powder micro porous solids. It is very likely that for samples S-pH-10Al and S-A-20Al structural destabilization is associated with the presence of a large amount of Al located deep within the pore walls. The presence of Al deep within the pore walls can act to cancel out part of the stabilizing effects of Al located on or nearer to the surface. This argument is consistent with previous results published in literature that Al-grafted mesoporous materials, in which all the incorporated Al is located on the surface or near surface region of the pore walls, exhibit excellent stability even at very small amounts of aluminium [32,50].

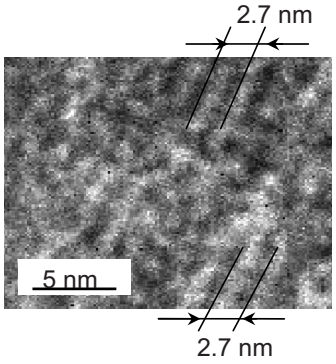

Figure 2.5. TEM image of S-A-7Al.

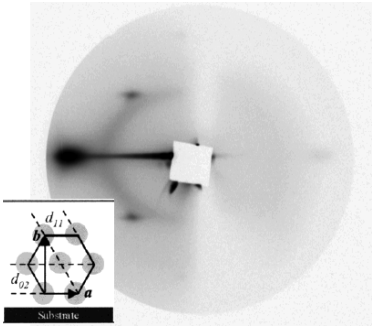

Figure 2.6. 2D-SAXS pattern of calcined S-A-20Al.

A representative TEM image of sample S-A-7Al synthesized at a constant amount of acid further confirms the conclusions from the XRD patterns, which clearly reveals the parallel orientation of the channels preferably along the long axis, suggesting that the materials obtained have a finely ordered 2D channel mesostructure (Figure 2.5). The ordered structure covers a large area, which means that the film has an ordered structure with a pore diameter of ca. 1.4 nm.

A typical 2D-SAXS pattern is shown in Figure 2.6 for S-A-20Al. In the *P6mm* structure, the densest lattice planes are preferentially oriented parallel to the substrate surface [9]. A similar pattern assigned to a 2D hexagonal structure was observed on the all-silica sample S-pH (not shown). Such a diffraction pattern has been shown to be typical for rectangular-centered domains with denser planes lying flat on the substrate and random in-plane orientation. The distortion from the 2D-hexagonal packing to a rectangular centered packing is due to stresses induced by solvent evaporation [58].

TGA/DTG measurements were performed to determine the minimum temperature required for removal of the surfactant. The all-silica sample (S-A) was heated at 10 K/min from 323 to 773 K (50 to 500°C) (Figure 2.7). The first 1.3 wt.% of total weight losses is assigned to removal of the absorbed water and a part of the bound water in the 323-373 K (50 to 100°C) range. The surfactant was removed in the 473-573 K (200 to 300°C) range which covered 31.1 wt.% of total mass losses.

The remaining carbon species were removed in the 573-773 K (300 to 500°C) range (4.7 wt.% of total mass losses). The total weight loss was 37.1 wt.%. Beside complete template removal, calcination to 773 K (500°C) resulted also in a structure consolidation (dehydration of siliceous walls and dehydroxylation of siliceous surface), accompanied by shrinkage and/or in some cases collapse of the structure. Therefore, a lower temperature of 573 K (300°C) in combination with a low residual pressure (10-15 mbar) was applied during systematic studies.

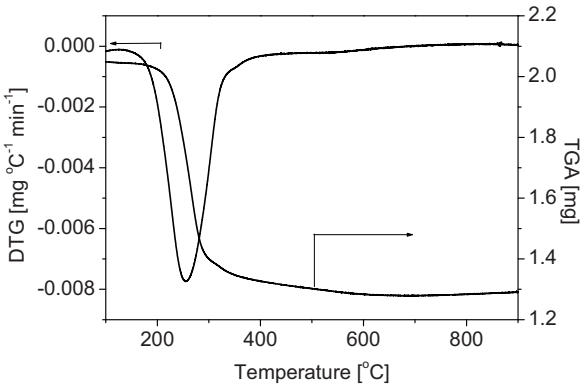

Figure 2.7. DTG–DTA curved performed on a S-A film in a nitrogen flow. Heating rate: 10 K/min.

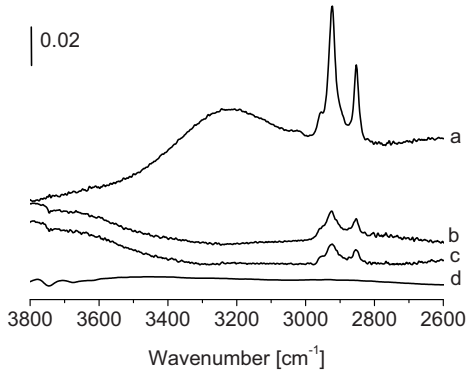

Figure 2.8. FTIR spectra of S-A films (a) as-synthesized, calcined at (b) 523, (b) 548, and (c) 573 K.

Figure 2.8 shows FTIR spectra of the as-synthesized and calcined all-silica (S-A) films. The calcination was carried out at a residual pressure of 15 mbar for 6 h. Two peaks at 2934 and 2853 cm^{-1} are ascribed to the asymmetric and symmetric vibrations of the C-H bonds of the surfactant, respectively [60]. The peak at 3250 cm^{-1} is ascribed to vibration of the hydroxyl groups. The peaks of the C-H vibrations decreased but still existed after calcination at 523 and 548 K, indicating that decomposition of the surfactant was not completed at these temperatures. Those bands disappeared at 573 K demonstrating the complete surfactant removal. The calcined film exhibits a broad peak in the range between 3000 and 3800 cm^{-1}, which is attributed to the physical absorption of water on the film surface [25]. The silanol groups at 3750 cm^{-1} are not clearly shown in Figure 2.8. The spectral range up to 3800 cm^{-1} was aimed to get a precise background line in the whole region.

It appears that a period of 4 h is sufficient for surfactant removal as no considerable differences were observed in the FTIR spectra after longer calcination periods at 573 K (not shown in Figure 2.8).

2.3.3 Stability in organic solvents

2D hexagonal porous materials have the thinnest parts of their framework between the adjacent pore channels. The degradation of these thinnest parts leads to the merging of adjacent pores, and also to the local loss of the connection between the parts of the framework, which may finally lead to the loss of integrity of such 3D framework structures. To compare the stability of thin films in different solvents, relatively mild conditions were applied that did not completely "destroy" the porous network but showed clear differences in the resulting physical characteristics.

The degree of long order structure decreased in all solvents, while disordering of the structure of the all-silica film was more pronounced than that of the Al-containing films after exposure to the polar solvents, especially in methanol and tetrahydrofuran (Table 2.3).

Table 2.3. d-spacing shift of S-A-20Al, S-A-7Al, and S-A films after exposure to different solvents for 48 h at 293 K.

Parameter	Fresh sample	After solvent exposure					
		Hexane (0.06)	DEE (2.90)	DCM (3.40)	THF (4.20)	2-propanol (4.30)	Methanol (6.60)
S-A							
d_{100}-spacing (nm)	2.69	2.69	2.77	2.79	2.80	2.74	2.56
d-spacing shift (%)		0	-3.1	-3.9	-4.3	-2.0	4.9
S-A-7Al							
d_{100}-spacing (nm)	2.99	3.04	2.95				
d-spacing shift (%)		-1.7	1.5				
S-A-20Al							
d_{100}-spacing (nm)	2.95	2.93	2.88	2.79	3.06	2.73	2.56
d-spacing shift (%)		0.5	2.1	2.1	-7.4	4.3	10.4

Polarity of the solvents are referred to [57]. Abbreviations: DEE – Diethyl ether, DCM – Dichloro methane, THF – Tetrahydrofuran.

The effect of aluminium content on the degree of d-spacing shift of the S-A-7Al and S-A-20Al films before and after solvent exposure is shown in Table 2.3. The degree of d-spacing shift demonstrates the same trend. The smallest d-spacing shift was observed in non-polar solvents, viz. hexane and diethyl ether. Sample S-A-7Al showed a higher degree of long-order structure than S-A-20Al. The degree of the d-spacing shift was smaller than that of the samples S-A-20Al and S-A. While a high Al content (S-A-20Al) mainly enhanced the non-aqueous stability, the low Al content (S-A-7Al) in the film mainly showed a positive effect in the stabilization of the structure after thermal treatment.

The XRD patterns of the all silica film (S-A) and two films with different Al content (S-A-7Al and S-A-20Al) after exposure to hexane and DEE for 48 h are shown in Figure 2.9. The unit cell slightly changed in all solvents due to swelling.

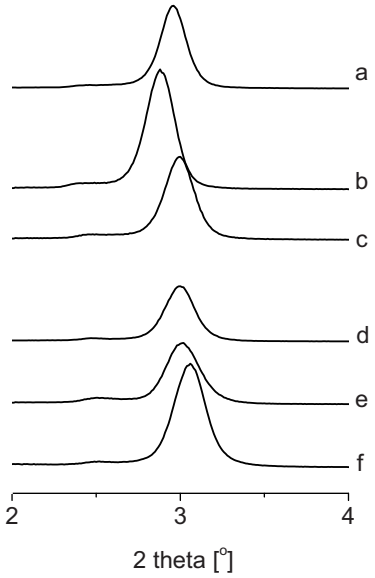

Figure 2.9. Small-angle XRD patterns of fresh samples S-A-7Al, S-A-20Al (a,d) and those after exposure to hexane (b, e), and DEE (c, f) for 48 h at 293 K.

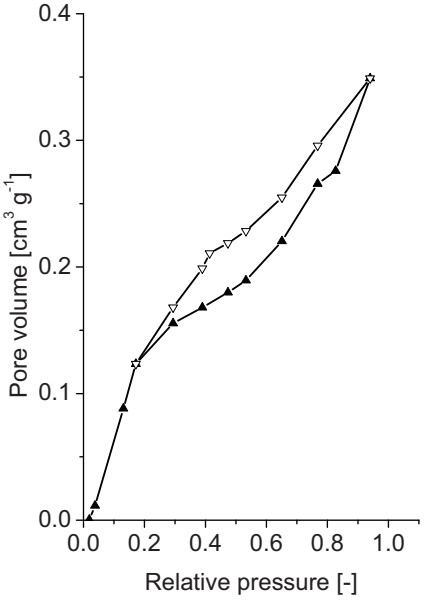

Figure 2.10. Ethanol adsorption-desorption isotherm at 287 K of 1 wt.% Pd/SiO_2 film (S-A-7Al) after reaction.

It can be seen that higher peak intensities were observed in the XRD patterns of silica films after solvent exposure (Figure 2.9 (b, c, e, and f)) as compared with those of the fresh samples (Figure 2.9 (a and d)). A similar effect was reported after exposure of mesoporous materials to an aqueous solution [61]. The authors concluded that the thin walls between the non-interconnected pores had collapsed and large pores were formed resulting in a higher contrast between the void and the wall. This resulted in an increased peak intensity.

Typical ethanol adsorption-desorption isotherm of film S-A-7Al after expose to hexane are shown in Figure 2.10. The isotherm is type IV with an H1 hysteresis loop. It appears that part of the micropores was not available for ethanol adsorption in the fresh samples because of pore blockage from both sides. Due to a partial collapse of the porous structure as a result of non-specific adsorption of solvents and appearance of large "transport" pores, the pore volume increased from 0.276 cm^3/g to

0.35 cm^3/g. These larger pores corresponded with the development of relatively open pore structures, which is in agreement with the pore entrance size enlargement on the two-step synthesis of FDU-1 observed during the hydrothermal heating at 373-413 K as reported elsewhere [27,62]. A partial collapse of the microporous network opened new passages in the porous structure which resulted in a larger pore volume.

In order to assess the stability of the silica films under real conditions of a hydrogenation reaction, the S-A-7Al film was impregnated with a Pd precursor to obtain 1 wt.% metal loading. The initial activities of Pd/SiO_2 remained high in two subsequent runs of phenyl acetylene hydrogenation [66,67] as shown in Table 2.4. High selectivity toward styrene over 61% was observed for the fresh catalyst (1st run). The selectivity to styrene over the spent catalyst (2nd run) significantly declined to less than 40%.

Table 2.4. Kinetic data from phenyl acetylene hydrogenation over 1 wt.% Pd-meso-SiO_2.

Catalyst	Initial hydrogenation rate (mmol/min/g_{Pd})	Selectivity at 35% conversion (%)		Selectivity at 50% conversion		Selectivity at 75% conversion	
		S_{ST}[a]	S_{EB}	S_{ST}	S_{EB}	S_{ST}	S_{EB}
1st run	43	61	39	63	37	58	42
2nd run	40	37	63	35	65	34	66

[a] ST is styrene and EB is ethyl benzene.

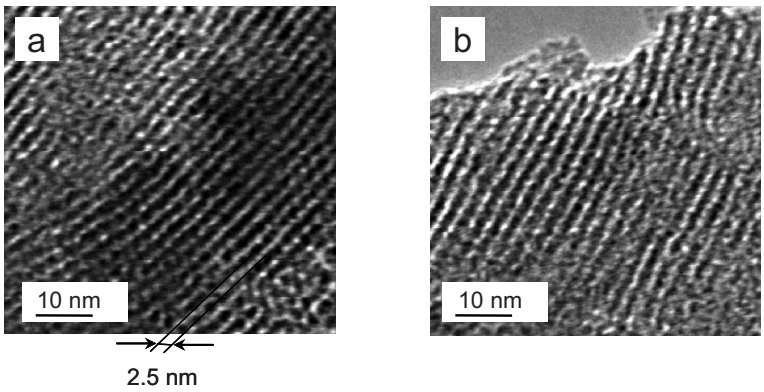

Figure 2.11. TEM images of the Pd/SiO_2 film: (a) fresh, (b) after 2 consecutive runs in hydrogenation of phenyl acetylene.

The TEM images of the fresh and spent catalytic films are shown in Figure 2.11 (a) and (b), respectively. A 2D porous structure with a channel size of ca. 2.5 nm and a silica wall thickness of 1.0 nm can be seen on the fresh sample. From the EDS analysis, palladium particles were found in this material. Pd nanoparticles with a size in the range of 1.5 to 4 nm were detected. It appeared that a part of the larger Pd particles (above 2 nm) was located in the larger pores between the micro porous domains. Larger particles with various sizes up to 15 nm were also present outside the mesostructured domain, which indicates that sintering happened during the reaction. The spent film shows the presence of mesoporosity, which indicates that the silica mesostructure of was still intact after the reaction.

2.4 Conclusions

Microporous silica films have shown potential for various applications, which require that the material remains stable for the life-time of the intended application and resists non-specific adsorption of solvents. The thermal stability of micro porous silica thin films, deposited on Si substrates, was improved by pH adjustment of the synthesis mixture to 2.0 during the hydrolysis of the silica precursor. It was further improved by incorporation of Al at an Al/Si ratio in the range of 0.005-0.007. At higher Al contents the presence of large amounts of Al deep within the pore walls cancelled out part of the stabilizing effects of Al located on or nearer to the surface. After exposure to non-polar solvents, the long-order structure of the Al-containing films remained unchanged after 48 h. The samples with an Al/Si ratio of 0.007 showed the smallest d-spacing shift after exposure to non polar solvents. This demonstrates that aluminium incorporation enhanced the hydrothermal stability in organic solvents. The Pd-impregnated films with Al/Si=0.007 were stable in the hydrogenation of phenyl acetylene performed at 303 K and 10 bar H_2 with hexane as solvent. No catalyst deactivation was observed in two subsequent hydrogenation runs.

References

[1] T.M.H. Costa, M.R. Gallas, E.V. Benvenutti, J.A.H da Jornada, *J. Non-Cryst. Solids,* 220 (1997) 195-201.

[2] S. Sumiya, Y. Oumi, T. Uozumi, T. Sano, *J. Mater. Chem.* 11 (2001) 1111-1115.

[3] J. Liu, X. Zhang, Y. Han, F.S. Xiao, *Chem. Mater.* 14 (2002) 2536-2540.

[4] F.-S. Xiao, Y. Han, Y. Yu, X. Meng, M. Yang, S. Wu, *J. Am. Chem. Soc.* 124 (2002) 888-889.

[5] Y. Han, S. Wu, Y. Sun, D. Li, F.-S. Xiao, J. Liu, X. Zhang, *Chem. Mater***.** 14 (2002) 1144-1148.

[6] X. Meng, D. Li, X. Yang, Y. Yu, S. Wu, Y. Han, Q. Yang, D. Jiang, F.-S. Xiao, *J. Phys. Chem. B* 107 (2003) 8972-8980.

[7] Y. Di, Y. Yu, Y. Sun, X. Yang, S. Lin, M. Zhang, S. Li, F.-S. Xiao, *Micropor. Mesopor. Mater.* 62 (2003) 221-228.

[8] Y. Lu, R. Ganguli, C.A. Drewlen, M.T. Anderson, C.J. Brinker, W. Gong, Y. Guo, H. Soyez, B. Dunn, M.H. Huang, J.I. Zink, *Nature* 389 (1997) 364-368.

[9] D. Grosso, F. Babonneau, P.A. Albouy, H. Amenitsch, A.R. Balkenede, A. Brunet-Bruneau, J. Rivory, *Chem. Mater*. 14 (2002) 931–939.

[10] S. Besson, T. Gacoin, C. Ricolleau, C. Jacquiod, J.P. Boilot, *J. Mater. Chem*. 13 (2003) 404-409.

[11] M. Matheron, T. Gacoin, J-P. Boilot, *Soft Matter* 3 (2007) 223-229.

[12] F. Cagnol, D. Grosso, G.J.A.A. Soler-Illia, E.L. Crepaldi, F. Babonneau, H. Amenitsch, C. Sanchez, *J. Mater. Chem*. 13 (2003) 61-66.

[13] D. Kundu, H.S. Zhou, I. Honma, *J. Mater. Sci. Lett*. 17 (1998) 2089-2092.

[14] I. Honma, H. Zhou, D. Kundu, A. Endo, *Adv. Mater*. 12 (2000) 1529-1533.

[15] R. Mokaya, *J. Mater. Chem*. 12 (2002) 3027-3033.

[16] R. Mokaya, *Chem. Commun*. 7 (2001) 933-934.

[17] A.S. O'Neil, R. Mokaya, M. Poliakoff, *J. Am. Chem. Soc.* 124 (2002) 10636-10637.

[18] R. Mokaya, *ChemPhysChem.* 3 (2002) 360-363.

[19] S.C. Shen, S. Kawi, *J. Phys. Chem. B* 103 (1999) 8870-8876.

[20] K. Cassiers, T. Linssen, M. Mathieu, M. Benjelloun, K. Schrijnemakers, P. Van Der Voort, P. Cool, E.F. Vansant, *Chem. Mater.* 14 (2002) 2317–2324.

[21] J.D. Bass, D. Grosso, C. Boissiere, E. Belamie, T. Coradin, C. Sanchez, *Chem. Mater*. 19 (2007) 4349–4356.

[22] F. Zhang, Y. Yan, H. Yang, Y. Meng, C. Yu, B. Tu, D. Zhao, *J. Phys. Chem. B* 109 (2005) 8723-8732.

[23] R. Mokaya, *J. Phys. Chem. B* 103 (1999) 10204-10208.

[24] R. Ryoo, J. Kim, *J. Chem. Soc. Chem. Commun*. 7 (1995) 711-712.

[25] D. Zhao, J. Feng, Q. Huo, N. Melosh, G.H. Frederickson, B.F. Chmelka, G.D. Stucky, *Science* 279 (1998) 548-552.

[26] N. Nishiyama, S. Tanaka, Y. Egashira, Y. Oku, K. Ueyama, *Chem. Mater*. 14 (2002) 4229-4234.

[27] M. Kruk, E.B. Celer, M. Jaroniec, *Chem. Mater.* 16 (2004) 698-707.

[28] Q. Huo, D.I. Margolese, G.D. Stucky, *Chem. Mater.* 8 (1996) 1147-1160.

[29] R. Ryoo, J.M. Kim, C.H. Ko, C.H. Shin, *J. Phys. Chem.* 100 (1996)17718-17721.

[30] R. Ryoo, S. Jun, *J. Phys. Chem. B* 101 (1997) 317-320.

[31] D. Das, C.-M. Tsai, S. Cheng, *Chem. Commun*. 5 (1999) 473-474.

[32] J.M. Kim, S. Jun, R. Ryoo, *J. Phys. Chem. B* 103 (1999) 6200-6205.

[33] Y. Han, F.-S. Xiao, S. Wu, Y. Sun, X. Meng, D. Li, S. Lin, F. Deng, X. Ai, *J. Phys. Chem. B* 105 (2001) 7963-7966.
[34] R. Mokaya, *J. Phys. Chem. B* 104 (2000) 8279-8286.
[35] R. Mokaya, *Chem. Commun*. (2000) 1541-1542.
[36] R. Mokaya, *Chem. Comm*. (2001) 633-634.
[37] R. Mokaya, W. Jones, *Chem. Commun*. (1997) 2185-2186.
[38] D.T. On, S. Kaliaguine, *J. Am. Chem. Soc.* 125 (2003) 618-619.
[39] D.T. On, S. Kaliaguine, *Angew. Chem. Int. Ed.* 41 (2002) 1036-1040.
[40] R. Mokaya, *Angew. Chem. Int. Ed*. 38 (1999) 2930-2934.
[41] S. Kawi, S.C. Shen, *Stud. Surf. Sci. Catal. 129* (2000) 227-234.
[42] S.C. Shen, S. Kawi,. *Langmuir* 18 (2002) 4720-4728.
[43] Y. Liu, T.J. Pinnavaia, *Chem. Mater***.** 14 (2002) 3-5.
[44] Z. Zhang, Y. Han, L. Zhu, R. Wang, Y. Yu, S. Qiu, D. Zhao, G.-S. Xiao, *Angew. Chem. Int. Ed.* 40 (2001) 1258-1262.
[45] Q.Yang, Y.Li, L.Zhang, J.Yang, J.L, C.Li, *J. Phys. Chem. B*, 108 (2004) 7934-7937.
[46] M. Ogawa, *Colloid Polym. Sci*, 281 (2003) 665-672.
[47] M. Ogawa, K. Kuroda, J. Mori, *Langmuir*, 18 (2002) 744-749.
[48] M. Ogawa, N. Masukawa, *Micropor. Mesopor. Mater*. 38 (2000) 35-41.
[49] A. Liepold, K. Roos, W. Reschetilowski, A.P. Esculcas, J. Rocha, A. Philippou, M.W.Anderson, *J .Chem. Soc. Faraday Trans*. 92 (1996) 4623-4629.
[50] M. Mies, J. van den Bosch, E.V. Rebrov, J. Jansen, M.H.J.M. de Croon, J.C. Schouten, *Catal. Today*, 111 (2005) 38-46.
[51] E.V. Rebrov, A. Berenguer-Murcia, H.E. Skelton, B.F. G. Johnson, A. E. H. Wheatley, J.C. Schouten, *Lab Chip*. 9 (2009) 503-506.
[52] L.N. Protasova E.V. Rebrov, Z.R. Ismagilov, J.C. Schouten, *Micropor. Mesopor. Mater*. 123 (2009), 243-252.
[53] M. Miyahara, T. Yoshioka, M. Okazaki, *J. Chem. Phys*. 106 (1997) 8124-8134.
[54] P. Emmett, S. Brunauer, *J. Am. Chem. Soc*. 59 (1937) 1553-1564.
[55] P. Guilbot, A. Valtz, H. Legendre, D. Richon, *Analysis* 28 (2000) 426–431.
[56] X. Zhang, W. Wu, J. Wang, C. Liu, *Thin Solid Films*, 515 (2007) 8376–8380
[57] D. Dunphy, S. Singer, A.W. Cook, B. Smarsly, D.A. Doshi, C.J. Brinker, *Langmuir*, 19 (2003) 10403-10408.
[58] M. Klotz, P-A. Albouy. A. Ayral, C. Ménager, D. Grosso, A. Van der Lee, V. Cabuil, F. Babonneau, C. Guizard, *Chem. Mater*. 12 (2000) 1721-1728.
[59] F. Kleitz, W. Schmidt, F. Schüth, *Micropor. Mesopor. Mater.* 65 (2003) 1-29.
[60] K.H.S. Kung, K.F. Hayes, *Langmuir* 9 (1993) 263-267.
[61] M. Landau, S. Varkey, M. Herskowitz, O. Regev, S. Pevzner, T. Sen, Z.Luz, *Micropor. Mesopor. Mater.* 33 (1999) 149-163.
[62] J. R. Matos, M. Kruk, L. P. Mercuri, M. Jaroniec, L. Zhao, T. Kamiyama, O. Terasaki, T.J. Pinnavaia, Y. Liu, *J. Am. Chem. Soc. 125* (2003) 821-829.
[63] J. March, *Advanced Organic Chemistry,* third ed., John Wiley & Sons, New York 1992.
[64] Smallwood, *Handbook of Organic Solvent Properties*, John Wiley & Sons, New York, 1996.
[65] M.B. Smith, J. March, *March's Advanced Organic Chemistry: Reactions, Mechanisms, and Structure*, fifth ed., John Wiley & Sons, New York, 2001.
[66] S.D. Jackson, L.A. Shaw, *Appl. Catal A*. 134 (1996) 91-99.
[67] R.V. Chaudhari, R. Jaganathan, D.S. Kolhe, G. Emig, H. Hofmann, *Chem. Eng. Sci*. 41 (1986) 3073-3081.

Chapter 3

Mesoporous silica films as catalyst support for microstructured reactors: Preparation and characterization

This chapter is adapted from: O. Muraza, E.V. Rebrov, T. Khimyak, B.F.G. Johnson, P.J. Kooyman, U. Lafont, M.H.J.M. de Croon, J.C. Schouten, Mesoporous silica films as catalyst support for microstructured reactors: Preparation and characterization, *Chem. Eng. J*. 135, 2008, S99-S103.

Abstract

Mesoporous silica thin films with hexagonal and cubic mesostructures have been deposited by the evaporation induced self-assembly assisted sol-gel route on microchannels etched in a Pyrex® 7740 borosilicate glass substrate. Prior to the synthesis, a 50 nm TiO_2 film has been deposited on the substrate by atomic layer deposition from titanium tetrachloride and water to increase the adhesion of the mesoporous films to the walls of the substrate. The mesoporous films were produced by templating a silica precursor (TEOS) with the non-ionic surfactant Pluronic F127 ($EO_xPO_yEO_x$, EO = ethylene oxide, PO = propylene oxide, x = 106, y = 70). Microchannels with a depth of 50 μm and with several different widths of 100, 150, 200, and 250 μm were used. Depending on the microchannel geometry, the thickness of the porous films along the channels varies in the range of 0.3-1.0 μm. The most uniform films across the whole channel cross-section were obtained at the width-to-depth ratio of 2. Afterwards, the mesoporous films were impregnated with an ether-dichloro methane suspension of $[PPN]_2[Ru_{10}Pt_2C_2(CO)_{28}]$ mixed-metal cluster

precursor to obtain well-dispersed, isolated and anchored bimetallic nanoparticles of 3-4 nm.

3.1 Introduction

Future development in catalytic microreactor technology will be strongly promoted by a progress in techniques to incorporate very active catalyst films into microreactors [1]. Up to now, many catalyst supports were amorphous materials with a low surface area and non-structured porosity, usually developed by wash coating [2,3] and anodic oxidation techniques [3]. Porous solids such as microporous and mesoporous materials [4-7] are the new generation of high surface area catalysts and catalyst supports [8], which can be used in microstructured reactors. Especially mesoporous silica thin films with an ultrahigh specific surface area (800-1000 m^2/g) and a tunable pore size in the range between 2 and 8 nm [9-10], coated on the walls of microchannels, have a large potential as a catalyst support in processing of large organic molecules, which are usually intermediates in the production of fine chemicals. Several techniques have already been explored, e.g. modified sol-gel [11-12], *in situ* hydrothermal synthesis [13], and evaporation induced self-assembly [14-15], to obtain the coatings of porous oxides with a large surface area and either hexagonal or cubic mesostructures in microchannels by open channel infiltration. The effects of the composition of the initial solution and the aging time have been studied to find the desired fraction of the organic phase to modulate the reactivity of the precursors and to adjust preferential interactions at the organic/inorganic interface in subsequent self-assembly processes. However, the physical aspects of mesostructured films such as film uniformity and film thickness are less explored on prestructured substrates. The non-uniformity in the thickness of a catalytic coating increases the residence time distribution in a microreactor resulting in a lower conversion and selectivity. In order to avoid severe non-uniformity with respect to the coating thickness, the latter has to be below 2% of the open channel cross section [16]. This implies that very active catalysts have to be used in order to provide effective utilization of the reactor volume.

Supported bimetallic clusters have been proved to be superior to their monometallic counterparts in selective hydrogenations [17-19]. There are several ways to prepare bimetallic heterogeneous catalysts on a surface. Co-impregnation of metal salts is the most common method to obtain bimetallic catalysts. The drawback of this technique is a large variation in the size, morphology and stoichiometry of the resulting nanoparticles, since there is hardly any control of the structure and composition during the subsequent reduction step. On the contrary, mixed-metal cluster impregnation provides a good size and composition control. In this method, the bimetallic cluster precursors are adsorbed on the support from a suspension and activated by removal of the ligands with gentle thermolysis [20-23]. Coalescence and sintering of the nanoparticles are prevented by firmly anchoring them to the support. Therefore, it is important that the support has a high concentration of the functional groups on the surface to accommodate the nanoparticles.

Our previous work [24] was focused on the development of a method to deposit thin silica films on the flat Pyrex® 7740 borosilicate glass substrates using triblock copolymer Pluronic F127 ($EO_xPO_yEO_x$, EO = ethylene oxide, PO = propylene oxide, x = 106, y = 70) as structure directing agent. The destabilization of the sol was done by an Evaporation-Induced Self-Assembly (EISA) [14-15] method in a spin-coater for 30 s to form an intermediate hybrid material. A F127/silica ratio of 0.0076 and a spinning rate of 1500 rpm were found to be optimal to obtain films with a large surface area (above 500 m^2/g) and a monomodal pore size distribution with a mean pore size between 6.9 and 8.2 nm [24]. Spinning rates below 1500 rpm were found to be not fast enough for complete solvent evaporation while the thickness of the films obtained above 1500 rpm was far below 1 μm. In the present study, this method was adapted to the deposition of thin films in semi-oval microchannels with a depth of 50 μm. The channels with widths of 100, 150, 200, and 250 μm were used to investigate the effect of the channel aspect ratio on the uniformity of the films produced. These mesostructured silica films are then impregnated with a Pt-Ru mixed metal cluster to obtain the active catalysts. By this approach, the functionality of the relatively fragile (bi)metallic clusters is mediated through the rigid inorganic framework providing

protection and the 3D distribution of the catalytic function. The resulting films can be used in a number of fine chemicals synthesis reactions.

3.2 Experimental

3.2.1 Synthesis of catalytic films

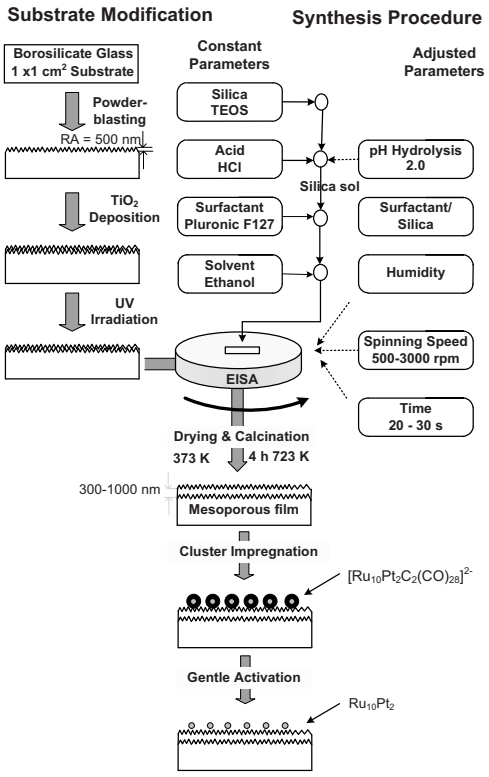

Scheme 3.1. Method for preparation of mesoporous catalytic films on a substrate.

The preparation method includes three major steps: substrate modification, preparation of the mesoporous silica films, and catalyst deposition (Scheme 3.1). A straight microchannel with a depth of 50 μm and a semi-oval cross section was etched in a Pyrex® 7740 borosilicate glass plate (20 mm length, 10 mm width, and 0.5 mm thickness). The channels with widths of 100, 150, 200, and 250 μm were produced by wet etching. The surface roughness of the substrates was increased to 0.5 μm by a micropowder jet treatment to prevent crack formation in the catalytic

layer during subsequent temperature excursions. A 50 nm TiO_2 layer was deposited by atomic layer deposition (ALD) from titanium tetrachloride and water to improve adhesion of the films to the substrate surface. Just before the synthesis, the titania layer was made super hydrophilic (> 15 OH groups/nm^2) by a UV treatment [25]. The sol molar composition was 1.0 TEOS : 0.0055-0.0076 Pluronic F127: 5.60 ethanol: 5.03 H_2O. The details of the preparation procedure are reported in [24].

The molecular cluster $[PPN]_2[Ru_{10}Pt_2C_2(CO)_{28}]$ was used as a precursor for the nanoparticle catalysts [21-23]. Four substrate plates with deposited mesoporous films were fixed in a holder and then immersed in an ether-dichloro methane suspension (20 ml ether and ten drops of dichloro methane) containing 10 mg (2.8 μmol) of the precursor for four days. Then the plates were washed with diethyl ether and dried in vacuum. The impregnated plates were subsequently heated in vacuum at 453 K to decarbonylate the molecular cluster leading to the formation of anchored bare metallic nanoparticles.

3.2.2 Characterization

The phase composition was determined by X-ray Diffraction in the range of 0.5-4° 2θ, using step scanning at 0.02° 2θ per step size and a counting time of 1 or 10 s for each step. XRD data were collected on a Rigaku Geigerflex Max/B diffractometer (40 kV, 40 mA) with Cu Kα radiation. Ellipsometric Porosimetry (EP) was used to determine the mean pore size and the pore-size distribution. The morphology of the films was determined by High Resolution Transmission Electron Microscopy (HR-TEM). HR-TEM was performed using a Philips CM30T microscope equipped with a LaB_6 filament and operated at 250 kV or a Philips CM30UT microscope equipped with a FEG operated at 300 kV. The particle size distribution (PSD) was obtained by measuring 100 particles from the HR-TEM micrographs. The mean particle diameter was calculated by the following formula: $d_m = \frac{1}{100}\sum_{i=1}^{100} n_i d_i$, where n_i is the number of particles with diameter d_i.

The morphology of the films was also studied by a field-emission gun scanning electron microscope (FEG-SEM, Philips SEM XL40 FEG) and a laser scanning confocal microscope (LSCM). The FEG-SEM was operated at 6 or 8 kV. For FE-SEM, the samples were glued to the sample holder with carbon tape. To make the samples conductive, they were sputtered with platinum. Two FEG-SEM images of the channel cross sections were taken at the side and at the bottom wall of the microchannel to study the uniformity of the film layer (Figure 3.1, positions a and b, respectively).

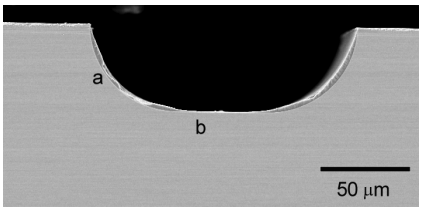

Figure 3.1. FEG-SEM image of spin-coated mesoporous silica (a) side wall (b) bottom of microchannel.

3.3 Results and discussion

Previous work [24] showed that a spinning rate of 1500 rpm is required to obtain accesible mesoporous silica films with a thickness of ca. 1 μm. Correspondingly, it was presented that by varying surfactant to silica ratio, pH, and aging time, mesoporous silica films with hexagonal and cubic mesostructures can be prepared on Pyrex® 7740 borosilicate glass substrates by the evaporation induced self-assembly assisted sol-gel route. Both EP and HR-TEM gave similar results. HR-TEM images of the most-accesible cubic mesostructured films templated by Pluronic F127 are shown in Figure 3.2. Regular long-order mesostructured silica films with an average pore size of 8.2 nm were observed. The diffraction patterns of the corresponding films [24] reveal that the mesostructure has 3D cubic *Im3m* symmetry (a_0 = 15.9 nm). The pore size is 8.2 nm as confirmed by HR-TEM images in Figure 3.2 (b).

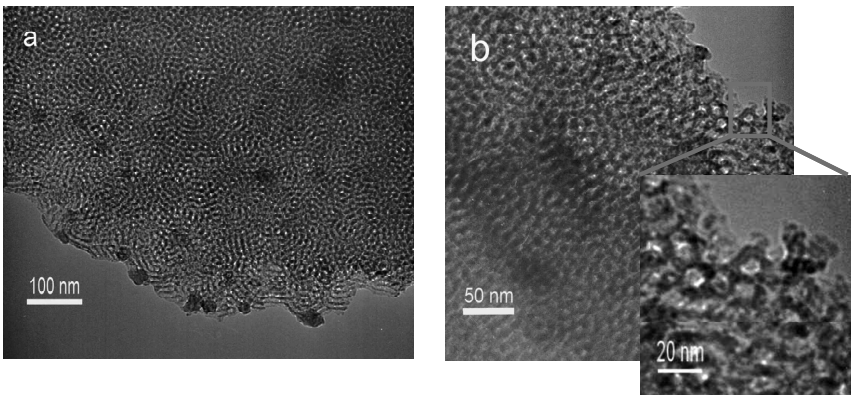

Figure 3.2. HR-TEM images of highly-ordered silica mesostructures as catalyst support, (a) Highly ordered mesostructured silica, (b) Magnification of cubic mesostructured silica with pore size of 8.2 nm.

Typical ethanol adsorption-desorption isotherms are shown in Figure 3.3. The sample exhibits a Type IV isotherm with a hysteresis loop and a narrow pore size distribution. The mean pore size is 6.9 nm. The total pore volume is 0.3 cm^3/g. These data are close to those reported in literature (6.5 nm and 0.45 cm^3/g) for F127 templated mesoporous silica films [9].

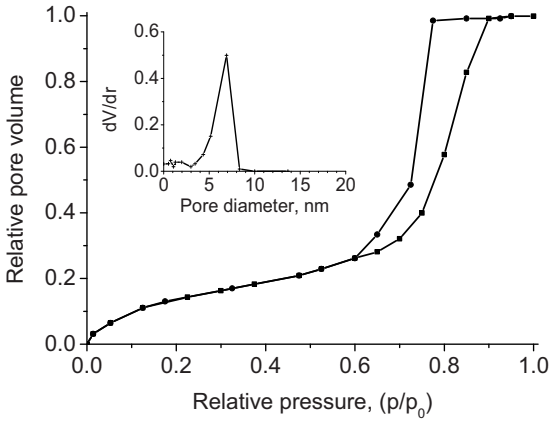

Figure 3.3. Ethanol adsorption (■) –desorption (●) isotherms and pore size distribution plot. The sol composition was: 1.0 TEOS : 0.0076 Pluronic F127: 5.60 ethanol: 5.03 H_2O. Spinning rate of 1500 rpm.

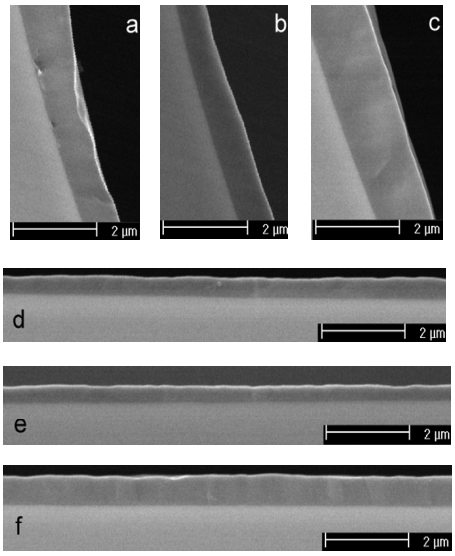

Figure 3.4. Cross sectional FEG-SEM images of highly-ordered silica mesostructure films in a microchannel with an aspect ratio (the width-to-depth ratio) of 2:1; (a, d); 3:1 (b, e) and 5:1 (c, f). The sol composition was the same as that in Fig. 3.1.

To investigate the influence of the channel geometry on the thin film quality, the width to depth ratio (t) of the microchannel was varied between 2 and 5. Typical FEG-SEM images of channel cross sections with deposited mesoporous silica films are shown in Figure 3.4. One can see that a continuous film was obtained in all cases. However, the thickness of the film on the side walls was always larger than on the bottom of the microchannel (Table 3.1). The silica film at the side walls was the thickest (1.40 ± 0.04 µm) on the channel with the width-to-depth ratio of 5. The largest difference in the film thickness between the side and bottom walls (*h-factor*) of ca. 2.4 was also observed at this aspect ratio. Within the limitations of this study (one spinning rate and one sol composition), there was only little difference in film thickness between the microchannels with t =2 and 3. In both cases, thinner films were obtained both on the side and the bottom walls. The *h-factor* of 2.0 – 2.1 is considered to be reasonable. An uneven distribution of coating thickness in the microchannels was previously reported after wash coating [2] and sol-gel routes [26]. Zapf and co-workers [2] observed deviations in film thickness between the side and

bottom walls of microchannels of 2 – 3.5 times with the thickest film always at the bottom.

Table 3.1. The thickness of mesoporous silica films at different aspect ratios of the microchannel cross-section.

T	Film thickness, μm				$\frac{\bar{h}_s}{\bar{h}_b}$
	Side wall (h_s)		Bottom wall (h_b)		
	min	max	min	max	
2	0.79	1.00	0.40	0.45	2.1
3	0.67	0.78	0.36	0.37	2.0
5	1.36	1.44	0.58	0.59	2.4

Generally, it has been reported that the larger the channel depth to width ratio, the higher the deviation in coating thickness. The situation is opposite when the spin-coating method was applied. The thickness of the film is always smaller at the bottom of the microchannels. The film thickness was slightly larger for a semicircular channel (t =2) as shown in Figure 3.5.

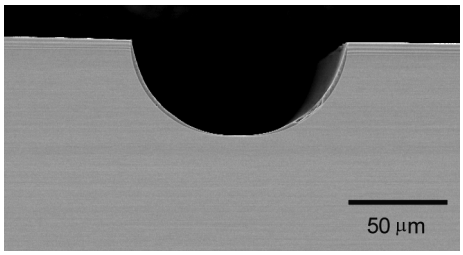

Figure 3.5. Cross sectional FE-SEM images of highly-ordered silica mesostructure films on a circular microchannel with cross-section of 100 x 50 μm². The other conditions are the same as those in Figure 3.3.

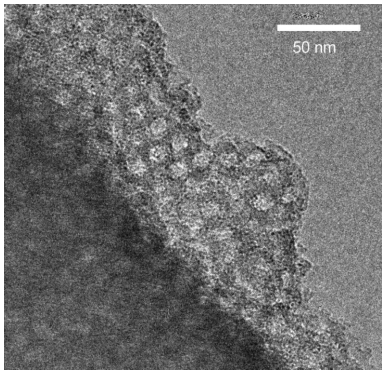

Figure 3.6. HR-TEM image of Pt-Ru particles deposited on mesostructured films. The other conditions are the same as those in Figure 3.3.

The adhesion tests with 15 minutes ultrasonication show that the adhesion of the mesoporous films to the substrate is good with a weight loss of less than 1%. The XPS data (not shown) reveal the bimetallic character of the nanoparticles while HR-TEM images show the intact mesoporosity after the encapsulation of the bimetallic

clusters. HR-TEM micrographs of bimetallic catalysts reveal the presence of randomly accessible ordered domains as well as the partly disordered mesostructure of the silica films. An example is given in Figure 3.6. The nanoparticles of Ru-Pt have a narrow particle size distribution. However, HR-TEM also shows the agglomeration of nanoparticles into large clusters. The metal particles are about 3 to 4 nm in diameter.

3.4 Conclusions

Mesoporous silica thin films with a thickness of 0.36 to 1.40 μm have been prepared by the evaporation induced self-assembly assisted sol-gel route on the microchannels etched in a Pyrex® 7740 borosilicate glass substrate. The width to depth ratio of the microchannels between 2 (semi-circular) and 3 (semi-oval) was found to provide the minimum non-uniformity of ca. 2 in the film thickness between the side and bottom walls of the microchannel. The mixed-metal precursor clusters of $Ru_{10}Pt_2$ have been inserted into the mesoporous films to obtain well-dispersed, isolated and anchored bimetallic nanoparticles of 3 to 4 nm. The intact long-order porosity with a pore size of 8.2 nm after the encapsulation of the bimetallic clusters was observed.

References

[1] V. Hessel, S. Hardt, H. Löwe, *Chemical Micro Process Engineering, Fundamentals, Modeling and Reactions,* Wiley-VCH (2004), Weinheim.

[2] R. Zapf, C. Becker-Willinger, K. Berresheim, H. Bolz, H. Gnazer, V. Hessel, G. Kolb, P. Löb, A.-K. Pannwitt, A. Ziogas, *Trans IChemE, Part A* 81 (2003) 721-729.

[3] M. Liauw, M. Baerns, R. Broucek, O.V. Buyevskaya, J.-M. Corriou, L. Falk, K. Gebauer, H.J. Hefter, O.-U. Langer, H. Lowe, M. Matlosz, A. Renken, A. Rouge, R. Schenk, N. Steinfeld, S. Walter, *Microreaction Technology: 3rd Int. Conf. Micro. Tech., Proceeding of IMRET 3*, W. Ehrfeld (ed.), Springer, Berlin, Germany, 224-234.

[4] C.T. Kresge, M.E. Leonowicz, W.J. Roth, J.C. Vartuli and J.S. Beck, *Nature* 359 (1992) 710-712.

[5] J.S. Beck, J.C. Vartuli, W.J. Roth, M.E. Leonowicz, C.T. Kresge, K.D. Schmitt, C.T. Chu, D.H. Olson, E.W. Sheppard, S.B. McCullen, J.B. Higgins and J.L. Schlenker, *J. Am. Chem. Soc.* 114 (1992) 10834-10843.

[6] D. Zhao, J. Feng, Q. Huo, N. Melosh, G. Fredrickson, B. Chmelka and G. Stucky, *Science* 279 (1998) 548-552.

[7] D. Zhao, Q. Huo, J. Feng, B. Chmelka and G. Stucky, *J. Am. Chem. Soc.* 120 (1998) 6024-6036.
[8] J.M. Thomas, R. Raja, *Stud. Surf. Sci. Catal.* 148 (2004) 163-211.
[9] D. Zhao, P. Yang, N. Melosh, J. Feng, B. Chmelka and G. Stucky, *Adv. Mater.* 10 (1998) 1380-1385.
[10] D. Grosso, F. Cagnol, G.J.d.A.A. Soler-Illia, E.L. Crepaldi, H. Amenitsch, A. Brunet-Bruneau, A. Bourgeois and C. Sanchez, *Adv. Funct. Mater*. 14 (2004) 309-322.
[11] K. Haas-Santo, M. Fichtner and K. Schubert, *Appl. Catal. A: Gen.* 220 (2001) 79-92.
[12] H. Chen, L. Bednarova, R.S. Besser, W.Y. Lee, *Appl. Catal. A: Gen.* 286 (2005) 186-195.
[13] E.V. Rebrov, G.B.F. Seijger, H.P.A. Calis, M.H.J.M. de Croon, C.M. van den Bleek, J.C. Schouten, *Appl. Catal. A: Gen.* 206 (2001**)** 125-143.
[14] C.J. Brinker, Evaporation-induced self-assembly: Functional nanostructures made easy**,** *MRS Bulletin* 29 (9) (2004) 631-640.
[15] M. Klotz, P-A. Albouy, A. Ayral, C. Ménager, D. Grosso, A. Van der Lee, V. Cabuil, F. Babonneau, C. Guizard, *Chem. Mater*. 12 (6) (2000) 1721-1728.
[16] E.R. Delsman, M.H.J.M. de Croon, G.D. Elzinga, P.D. Cobden, G.J. Kramer, and J.C. Schouten, *Chem. Eng. Technol*. 28 (2005) 367-375.
[17] B.F.G. Johnson. *Top. Catal*. 24 (2003) 147-159.
[18] R. Raja, T. Khimyak, J.M. Thomas, S. Hermans, B.F. G. Johnson, *Angew. Chem. Int. Ed.* 40 (2001) 4638-4642.
[19] W. Zhou, J. M. Thomas, D. S. Shephard, B. F. G. Johnson, D. Ozkaya, T. Maschmeyer, R. G. Bell, Q. Ge, *Science* 280 **(**1998) 705-708.
[20] S. Hermans, T. Khimyak**,** B.F.G. Johnson, *J. Chem. Soc. Dalton Trans*. 22 (2001) 3295-3302.
[21] B.F.G. Johnson, S. Hermans, T. Khimyak, *Eur. J. Inorg. Chem.* (2003) 1325-1331.
[22] T. Khimyak, B.F.G. Johnson, S. Hermans, A.D. Bond, *Dalton Trans*. 13 (2003) 2651-3657.
[23] H. Yagyu, K. Sugano, S. Hayashi, O. Tabata, *J. Micromech. Microeng*. 15 (2005) 1236-1241.
[24] O. Muraza, E.V. Rebrov, T. Khimyak, B.F.G. Johnson, P.J. Kooyman, U. Lafont, P-A. Albouy, M.H.J.M. de Croon, J.C. Schouten, *Stud. Surf. Sci. Catal.* 162 (2006) 167-174.
[25] R. Wang, K. Hashimoto, A. Fujishima, M. Chikuni, E. Kojima, A. Kitamura, M. Shimohigoshi, T. Watanabe, *Nature* 388 (1997) 431-432.
[26] G. Germani, P. Alphonse. M. Courty, Y. Schuurman, C. Mirodatos, *Catal. Today* 110 (2005) 114-120.

Chapter 4

Preparation and characterization of bimetallic catalysts supported on mesoporous silica films

This chapter is adapted from: O. Muraza, E.V. Rebrov, T. Khimyak, B.F.G. Johnson, P.J. Kooyman, U. Lafont, P-A. Albouy, M.H.J.M. de Croon, J.C. Schouten, Preparation and characterization of bimetallic catalysts supported on mesoporous silica films, *Stud. Surf. Sci. Catal.* 162 (2006) 167-174.

Abstract

Thin (300-1000 nm) mesoporous silica films with hexagonal and cubic mesostructures have been prepared on Pyrex® 7740 borosilicate glass substrates by the evaporation induced self assembly assisted sol-gel route. Prior to the synthesis, a 50 nm TiO_2 layer has been deposited on the substrate by atomic layer deposition from titanium tetrachloride and water to reach better adhesion of the coatings to the walls of the substrate. The films were produced by templating a silica precursor (TEOS) with an $EO_xPO_yEO_x$ amphiphilic triblock copolymer (EO = ethylene oxide, PO = propylene oxide, x = 106, y = 70) at a pH of 2. A surfactant/silica ratio of 0.0076 was found to be optimal at a spinning rate of 1500 rpm to obtain the films with a surface area above 500 m^2/g and a monomodal pore size distribution with a mean pore size of 6.9 nm. Mixed-metal precursor clusters $[Ph_4P]_2[Ru_5PtC(CO)_{15}]$ have been inserted into the mesoporous support. Then, the mesoporous-encapsulated clusters were activated by gentle heating in vacuo at 473 K. The average diameter of the resulting, well-dispersed, isolated and anchored bimetallic nanoparticles is 1.4 nm. By this approach, the functionality of the relatively fragile metallic clusters is mediated through the rigid inorganic framework providing protection and the 3D distribution

of the catalytic function. The resulting coatings can be used in a number of fine chemicals synthesis reactions.

4.1 Introduction

Mesoporous thin films are of interest for use as adsorbents and catalysts in microstructured reaction devices. Advantages of mesoporous films comparing to pelletized powder catalysts are the improved accessibility of the catalyst sites, improved heat- and mass transfer rates, negligible pressure drop, and the absence of macropores. The past decade has seen significant advances in the ability to synthesize different types of coatings with mesoporous structures from a wide range of different precursors. This resulted in materials with unusual properties and broadened their application range towards sensors, host materials to integrate molecular electronics, and other molecular devices within their frameworks [1]. As better and more diverse preparation protocols of mesoporous structures become available [2,3], an increasing number of porous materials are likely to find use in applications not traditionally associated with such materials. Mesoporous silica with an ultra high specific surface area and a surface concentration of silanol groups of 1-2 OH/nm^2, fulfill most of the criteria to be used as catalyst supports [4].

The application of thin mesoporous coatings in structured reactor types can be of interest from a catalytic point of view. For such applications, well-defined structures containing pores in the size range above 2 nm, ultrahigh specific surface area, and exhibiting thermal and hydrothermal stability are highly desirable, especially if the pore system is more than one-dimensional. An even more intensified contacting of the reactants with mesoporous coatings can be obtained in microstructured reactors [5].

Either hexagonal or cubic mesostructures can be synthesized using an amphiphilic triblock copolymer, Pluronic F127. The composition of the initial solution and the aging time have to be optimized to find the desired fraction of the organic phase to modulate the reactivity of the precursor and to adjust preferential interactions at the organic/inorganic interface in the subsequent self-assembly

processes. The self-assembly interaction between the surfactant and the inorganic silica source is classified as the hydrogen bonding (S^0H^+)(X^-I^+) route, where S is a surfactant head group, X^- is the halide anion, and I^+ is the inorganic precursor (TEOS) [3]. In a previous study [6], we demonstrated an effective method to prepare hexagonal silica films on glass substrates by Evaporation-Induced Self-Assembly (EISA) [7-9]. Pyrex glass is an ideal support for mesoporous silica films for application in a gas-liquid chemical synthesis because it has low density, high wear and corrosion resistance, and a low coefficient of thermal expansion. In the present contribution we demonstrate a preparation method to obtain 300 to 1000 nm thin mesoporous silica films with either hexagonal or cubic mesostructure with supported Pt-Ru bimetallic clusters, which will have a superior performance in many fine chemicals synthesis reactions [10-14].

4.2 Experimental

The preparation method includes three major steps: substrate modification, preparation of the mesoporous silica films, and catalyst deposition (Scheme 4.1).

4.2.1 Substrate modification

Pyrex® 7740 borosilicate glass plates (1 x 1 cm^2, 1 mm thickness) were used as substrates. The surface roughness of the substrates was increased to 500 nm by a micropowder jet treatment to prevent crack formation in the catalytic layer during subsequent temperature excursions. A 50 nm TiO_2 layer was deposited by atomic layer deposition (ALD) from titanium tetrachloride and water to reach better adhesion of the coatings to the substrate surface. Just before the synthesis, the titania layer was made super hydrophilic (> 15 OH groups/nm^2) by a UV treatment [15]. The hydrophilicity of the films was evaluated by measuring the contact angle of water on titania films using an automatic contact angle meter.

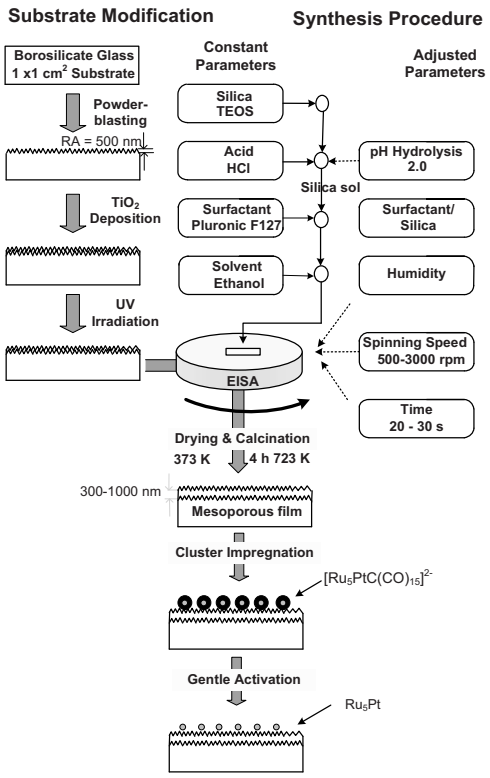

Scheme 4.1. Method for preparation of mesoporous catalytic films on a substrate.

4.2.2 Preparation of mesoporous silica films

The mesostructured films were produced by supramolecular templating a silica precursor (TEOS, 98% Merck) with Pluronic F127 ($EO_xPO_yEO_x$, EO = ethylene oxide, PO = propylene oxide, x = 106, y = 70, BASF) [3]. TEOS was prehydrolized in ethanol at 343 K below the isoelectric point of silica (pH = 2). The pH was adjusted by drop-wise addition of 1 M HCl. In parallel, Pluronic F127 was dissolved in 7.4 g of ethanol (Merck, 99.99%) and stirred for 10 min. The two solutions were mixed with each other, stirred and aged for 4-100 h. The molar composition of the prepared sol was 1.0 TEOS: 0.002-0.012 Pluronic F127: 5.60 ethanol: 5.03 H_2O. A part of the resulting sol (100 μL) was deposited on a Pyrex substrate. The destabilization of the sol was done by EISA in a spin-coater for 30 s to form an intermediate hybrid material. In these experiments, the evaporation rate was adjusted by varying of the spinning rate in the range of 1000-2500 rpm. The as-deposited films were dried at 373

K for 1 h to further remove ethanol and water. The dried films were soaked in water at 323 K for 30 minutes to remove HCl. The films were dried again at 373 K for 1 h, which was followed by calcination in an air flow with a heating rate of 1 K/min and a dwelling time of 4 h at 723 K. All films are referred to according to the F/127/Si ratio multiplied by 1000 and aging time. For example, a film obtained at F127/Si of 0.002 and aging time of 200 hours will be referred as Si-2-200.

4.2.3 Synthesis and deposition of mixed metal clusters of Ru-Pt

The molecular cluster $[Ph_4P]_2[Ru_5PtC(CO)_{15}]$ was used as a precursor for nanoparticle catalysts [14]. The substrates with the layer of mesoporous silica were dried at 473 K in vacuum. The deposition of the bimetallic clusters was achieved by immersing the substrates in an ether-dichloro methane or an ether-THF suspension (3 ml) containing 5 mg (2.8 μmol) of the precursor. This process was carried out for two days after which the plates were washed with diethyl ether and dried in vacuum. The impregnated plates were subsequently heated (either in vacuo or in air) at 473 K to decarbonylate the molecular cluster leading to the formation of anchored naked metallic nanoparticles.

4.2.4 Characterization of mesoporous silica films

The morphology of the films (hexagonal vs. cubic mesostructure) was determined by transmission electron microscopy (TEM) and two-dimensional small angle X-ray scattering (2D SAXS) measurements. 2D SAXS experiments were performed with a rotating anode X-ray generator (copper anode operated at 50 kV, 30 mA; small focus) equipped with two adjustable optical systems. The phase composition was determined by X-ray diffraction in the range of 0.5-4° 2θ, using step scanning at 0.02° 2θ per step size and a counting time of 1 or 10 s for each step. XRD data were collected on a Rigaku Geigerflex Max/B diffractometer (40 kV, 40 mA) with Cu Kα radiation. Ellipsometric porosimetry (EP) was used to determine the mean pore size and the pore size distribution. Prior to adsorption, the samples were treated in vacuum (background pressure of 0.1 mbar) at 573 K for 30 min to remove all

adsorbed species. Then, the temperature was decreased to 287 ± 0.5 K and ethanol vapour (Merck, 99.99%) was admitted up to a certain pressure. After the saturated vapour pressure ($p/p_0 = 1$) was established, the vapour was pumped off in several steps, tracking it by decrease of the pressure. The pore volume and the film thickness were determined from the change in the effective refractive index in the range of 300-1200 nm. The refraction index of the mesoporous film (n_M) and the total pore fraction ($1–f_M$) were calculated from the change in the effective refraction index (n_{ef}) at the end points of the isotherm using Bruggeman's equation [16] and the refraction indexes of air and ethanol (n_m = 1.0 and 1.361, respectively):

$$f_M \frac{n_M^2 - n_{ef}^2}{n_M^2 + 2n_{ef}^2} + (1 - f_M) \frac{n_m^2 - n_{ef}^2}{n_m^2 + 2n_{ef}^2} = 0 \qquad (2.1)$$

4.2.5 Characterization of bimetallic catalysts

High Resolution Transmission Electron microscopy (HR-TEM) images were recorded on a Philips CM-30 microscope operated at 250 kV. The films were scratched from the substrate. The collected powders and flakes were grinded and dispersed in ethanol. Then the suspensions were dropped gently to a holey amorphous carbon film on a Ni or Cu grid. The particle size distribution (PSD) was obtained by measuring 100 particles from the TEM micrographs. The mean particle diameter was calculated by the following formula: $d_m = \frac{1}{100}\sum_{i=1}^{100} n_i d_i$, where n_i is the number of particles with diameter d_i. The X-ray photoelectron spectroscopy (XPS) spectra were recorded on a VG Escalab MKII spectrometer, equipped with a dual Al/Mg-Kα X-ray source. Spectra were obtained using the aluminium anode (Al-Kα=1486.6 eV) which was operated at 480 W and constant pass energy of 20 eV with a background pressure of 2×10^{-9} mbar.

4.3 Results and discussion

The films obtained below a spinning rate of 1500 rpm were amorphous. Therefore, the spinning rate in the subsequent experiments was fixed at 1500 rpm to provide the thickness of the resulting coatings in the range of 300-1000 nm. In turn, a higher crystallinity of the films was obtained at the F127/Si ratio of 0.0078. The XRD patterns of the mesostructured films are shown in Figure 4.1.

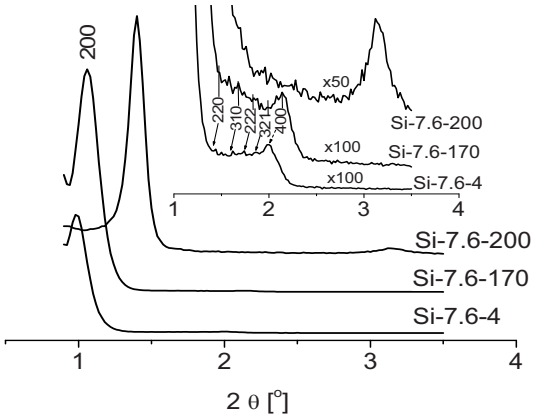

Figure 4.1. XRD patterns of mesoporous silica films at different aging times.

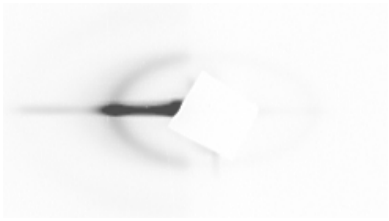

Figure 4.2. 2D SAXS for sample Si-7.6-200

The cubic structure (*Im3m*) was obtained at aging times below 170 hours as confirmed by the reflections at (200), (211), (220), (310), (222), (321), (400). Increasing the aging time from 4 to 170 hours decreased the unit cell size from 17.9 to 16.6 nm. At an aging time of 200 hours, only two peaks were observed at 1.40 and 3.14° 2θ, which might be assigned to a hexagonal structure. The 2D SAXS pattern of the sample Si-7.8-200 displays diffuse ellipses common in mesoporous silica films (Figure 4.2) [17].

Typical ethanol adsorption-desorption isotherms are shown in Figure 4.3. The sample exhibits a Type IV isotherm with a hysteresis loop and a narrow pore size distribution. The mean pore size is 6.9 nm. The total pore volume is 0.3 cm^3/g.

These data are close to those reported in literature (6.5 nm and 0.45 cm^3/g) for F127 templated mesoporous silica films [7].

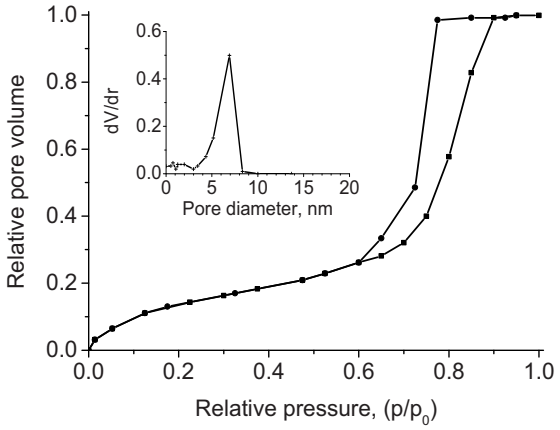

Figure 4.3. Ethanol adsorption (■) –desorption (●) isotherms and pore size distribution plot for sample Si-7.6-200.

TEM micrographs of bimetallic catalysts revealed the presence of randomly accessible ordered domains as well as the partly disordered mesostructure of silica films (Figure 4.4). The nanoparticles of Ru-Pt have a mean size of 1.4 nm with a narrow particle size distribution (Figure 4.5). However, the TEM image also shows the agglomeration of nanoparticles due to the absence of a local mesostructure.

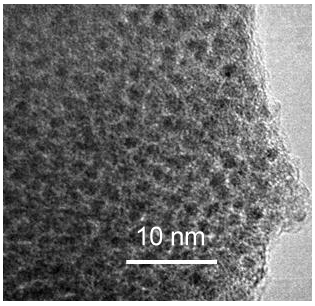

Figure 4.4. TEM image of Pt-Ru particles deposited on Si-7.6-200.

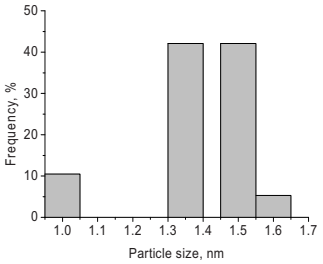

Figure 4.5. Particle size distribution for Pt/Ru clusters deposited on Si-7.6-200

XPS analyses were performed to determine the stoichiometry of the nanoparticles and oxidation states of the Ru and Pt (Figure 4.6). The spectrum of Pt

can be fitted by two pairs of overlapping curves corresponding to two doublets of spin orbital interaction at $4f_{5/2}$ and $4f_{7/2}$. The strongest doublet with binding energies of 74.42 ($4f_{7/2}$) and 77.84 eV ($4f_{5/2}$) is ascribed to Pt^{4+} [18,19]. The second doublet with binding energies of 72.63 ($4f_{7/2}$) and 76.04 eV ($4f_{5/2}$) is attributed to Pt^{2+}.

The Ru 3d spectra exhibit a spin orbit doublet of oxidized Ru with binding energies of 281.96 ($3d_{5/2}$) and 286.13 eV ($3d_{3/2}$). The second doublet is observed at 283.86 ($3d_{5/2}$) and 288.04 eV ($3d_{3/2}$). The peak at 284.9 eV belongs to C1s. The molar Pt/Ru ratio is 3.0 which is lower than that in the original cluster demonstrating partial decomposition of the bimetallic clusters, probably during the calcination step.

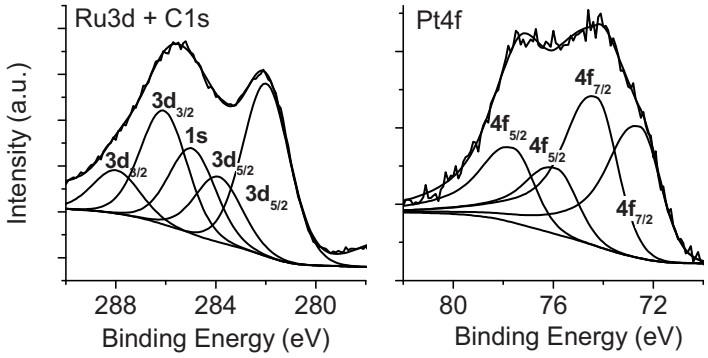

Figure 4.6. Regional XPS spectra of Pt 4f, Ru 3d, and C 1s for sample Si-7.6-200.

4.4 Conclusions

We presented the synthesis of mesostructured silica films via an evaporation-induced self-assembly method using the templating effect of the lyotropic mesophases. Both XRD and ethanol sorption analysis provide evidence of the mesostructural ordering. By adjusting the surfactant to Si ratio and the aging time during the sol preparation, mesoporous silicas with different morphologies and pore structures were synthesized. Bimetallic Pt-Ru catalysts have been prepared by immersing the mesoporous films in a solution containing mixed metal clusters $[Ph_4P]_2[Ru_5PtC(CO)_{15}]$. The mean diameter of the resulting, well-dispersed, isolated and anchored bimetallic nanoparticles is 1.35 nm with a very narrow partical size

distribution. The XPS data reveal the bimetallic character of the nanoparticles while TEM images show the intact mesoporosity after the encapsulation of the bimetallic clusters.

References

[1] M.E. Davis, *Nature* 417 (2002) 813-821.

[2] (a) C.T. Kresge, M.E. Leonowicz, W.J. Roth, J.C. Vartuli and J.S. Beck, *Nature* **359** (1992) 710. (b) J.S. Beck, J.C. Vartuli, W.J. Roth, M.E. Leonowicz, C.T. Kresge, K.D. Schmitt, C.T. Chu, D.H. Olson, E.W. Sheppard, S.B. McCullen, J.B. Higgins and J.L. Schlenker, *J. Am. Chem. Soc.* 114 (1992) 10834.

[3] (a) D. Zhao, J. Feng, Q. Huo, N. Melosh, G. Fredrickson, B. Chmelka and G. Stucky, *Science* 279 (1998) 548. (b) D. Zhao, Q. Huo, J. Feng, B. Chmelka and G. Stucky, *J. Am. Chem. Soc.* 120 (1998) 6024.

[4] J.M. Thomas, R. Raja, *Stud. Surf. Sci. Catal.* 148 (2004) 163.

[5] V. Hessel, S. Hardt, H. Löwe, Chemical Micro Process Engineering, Fundamentals, Modeling and Reactions, Wiley-VCH (2004), Weinheim.

[6] O. Muraza, E.V. Rebrov, T. Khimyak, B.F.G. Johnson, P.J. Kooyman, U. Lafont, M.H.J.M. de Croon, J.C. Schouten, *Chem. Eng. J.* 135 (2008) S99-S103.

[7] D. Zhao, P. Yang, N. Melosh, J. Feng, B. Chmelka and G. Stucky, *Adv. Mater***.** 10 (1998) 1380.

[8] C.J. Brinker**,** Evaporation-induced self-assembly: Functional nanostructures made easy**,** *MRS Bulletin* 29 (9) (2004) 631.

[9] D. Grosso, F. Cagnol, G.J.d.A.A. Soler-Illia, E.L. Crepaldi, H. Amenitsch, A. Brunet-Bruneau, A. Bourgeois and C. Sanchez, *Adv. Funct. Mater*. 14 (2004) 309.

[10] R. Raja, T. Khimyak, J.M. Thomas, S. Hermans, B.F. G. Johnson, *Angew. Chem. Int. Ed.* 40 (2001) 4638.

[11] W. Zhou, J. M. Thomas, D. S. Shephard, B. F. G. Johnson, D. Ozkaya, T. Maschmeyer, R. G. Bell, Q. Ge, *Science* 280 (1998) 705.

[12] B.F.G. Johnson, T. Khimyak. B.F.G. Johnson, *J. Chem. Soc., Dalton Trans*., (2001) 3295.

[13] B.F.G. Johnson, S. Hermans, T. Khimyak, *Eur. J. Inorg. Chem.* (2003) 1325.

[14] S. Hermans, T. Khimyak, B.F.G. Johnson, *J. Chem. Soc. Dalton Trans*. 22 (2001) 3295.

[15] R. Wang, K. Hashimoto, A. Fujishima, M. Chikuni, E. Kojima, A. Kitamura, M. Shimohigoshi, T. Watanabe, *Nature* 388 (1997) 431.

[16] V.A. Tomalchev, *J. Opt. Technol*. 68 (5) (2001) 328.

[17] M. Klotz, P-A. Albouy, A. Ayral, C. Ménager, D. Grosso, A. Van der Lee, V. Cabuil, F. Babonneau, C. Guizard, *Chem. Mater*. 12 (6) (2000) 1721.

[18] J.F. Moulder, W.F. Stickle, P.E. Sobol, and K.D. Bomben (Eds: J. Chastain), Perkin-Elmer Corporation (Physical Electronics), 1992.

[19] K.S. Kim, N. Winograd, R.E. Davis, *J. Am. Chem. Soc.* 93 (1971) 6296.

Chapter 5

Microwave-assisted hydrothermal synthesis of zeolite Beta coatings on ALD-modified borosilicate glass for application in microstructured reactors

This Chapter is adapted from:
O. Muraza, E.V. Rebrov, J. Chen, M. Putkonen, L. Niinistö, M.H.J.M. de Croon, J.C. Schouten, Microwave-assisted hydrothermal synthesis of zeolite Beta coatings on ALD-modified borosilicate glass for application in microstructured reactors, *Chem. Eng. J*. 135 (2008), pp. S117-S120.

Abstract

Stable zeolite Beta coatings with a thickness of 1 to 2 μm were synthesized on a borosilicate glass substrate by microwave-assisted hydrothermal synthesis and by *in situ* conventional hydrothermal synthesis with forced heating. Prior to the synthesis, the surface roughness of the substrate was increased to 1.0 μm. Then, two thin films of zirconia and titania were successively deposited at 573 K on the glass substrate by atomic layer deposition using $ZrCl_4$ as metal precursors for zirconia and $TiCl_4$ for titania, respectively. Oxygen and H_2O were used as oxygen precursors in the atomic layer deposition (ALD) process. The internal zirconia film protects the glass substrate from dissolution in a highly alkaline synthesis solution. The outer titania film was made superhydrophilic (> 15 OH/nm^2) by a UV irradiation, which enhances the nucleation and crystallization processes on the substrate. The crystallization rates

on the surface and in the bulk were characterized by X-ray diffraction (XRD), scanning electron microscopy (SEM), nitrogen adsorption (BET), and dynamic light scattering (DLS). The duration of the zeolite nucleation period was decreased by using the additive effect between fluoride ions and the zeolite seed solution under microwave irradiation. A uniform zeolite Beta coating was obtained already after 8 h at 423 K in a microwave oven from a precursor gel with SiO_2/Al_2O_3 = 25, TEAOH (tetraethyl ammonium hydroxide)/Al_2O_3 = 8.75, H_2O/SiO_2 = 11.6, NH_4F/SiO_2 = 0.2. This is almost six times faster comparing to conventional hydrothermal synthesis. Optimum conditions for the synthesis of uniform zeolite Beta coatings were found to be: SiO_2/Al_2O_3=25, TEAOH/Al_2O_3=8.75, H_2O/SiO_2=11.6, NH_4F/SiO_2=0.2, temperature of 423 K, and a synthesis time of 8 h in a microwave oven. The 4 wt.% seeds in water suspension was synthesized from SiO_2/Al_2O_3=94, TEAOH/Al_2O_3=33.5, H_2O/SiO_2=12, temperature of 373 K, and a synthesis time of 7 days.

In the *in situ* conventional hydrothermal synthesis method, a forced heating model was used in order to shorten the time to reach reaction temperature, without overheating. According to this model, the temperature of the synthesis gel reaches reaction temperature in 30 min, which is 9 h faster than with conventional heating. The coatings have been characterized by the same method mentioned before for MAHyS. The influence of the synthesis parameters such as reaction temperature, synthesis time, TEAOH/Al_2O_3 ratio, SiO_2/Al_2O_3 ratio, and H_2O/SiO_2 ratio on the zeolite Beta powder and coating has been studied. Optimum conditions for the synthesis of uniform zeolite Beta coatings were found to be: SiO_2/Al_2O_3=47, TEAOH/Al_2O_3=24.4, H_2O/SiO_2=14, (Na+K)/Al_2O_3=7, temperature of 403 K, and synthesis time of 48 h.

5.1 Introduction

The application of zeolitic coatings improves the performance of supported catalysts, as demonstrated in the case of membrane reactors [1], distillation units [2], adsorbents [3,4], catalytic packings [2], monoliths [5], and DeNOx reactors [6,7]. Incorporation of zeolitic coatings to microstructured reactors has also been

demonstrated for various applications [6,8,9]. The three-dimensional large pore zeolite Beta (BEA) is nowadays applied in a variety of catalytic gas and liquid phase processes such as alkylation and acylation of aromatics [10,11], selective hydrogenations [12], and fine chemicals synthesis [11]. The hydrothermal synthesis of zeolite Beta coatings is described on different molybdenum and titania substrates [8,13,14]

High-speed synthesis with microwaves has attracted a large attention in recent years due to considerable enhancement of reaction rates, especially in the area of organic synthesis [15]. Recently, Kim et al. have demonstrated that microwave assisted hydrothermal synthesis (MAHyS) with NH_4F as mineralizing agent results in a highly crystalline zeolite Beta (91% crystallinity) after 8 h at 423 K [16]. The coupling of microwave heating with a hydrothermal synthesis requires application of special non-polar substrate materials such as quartz, pure aluminium oxide (corundum), special glass types, and plastics. While these are not exotic materials for making microreactors and indeed have been applied for laboratory prototypes, there is presently no clear methodology how to perform *in situ* hydrothermal synthesis of zeolitic coatings on such substrate materials. Pyrex glass is considered to be an ideal support for zeolitic coatings in a liquid phase chemical synthesis. It has a high corrosion resistance, low coefficient of temperature expansion, and it is chemically inert towards many organic molecules. Furthermore, microchannels with a precise control of cross-section and surface roughness can be etched in glass by dry reactive ion etching. However, zeolite synthesis usually takes place at elevated temperatures (above 403 K) in a highly alkaline solution for several days. At these conditions, glass substrates would be completely dissolved during the synthesis. Therefore, an approach for the development of glass based microstructured devices is to utilize the intrinsic properties of glass through application of thin protective films, consisting of more alkali-resistant materials, e.g. zirconia, on the glass surface. The wettability can be improved by surface treatments or by deposition of a titania hydrophilic film, which can be made superhydrophilic (> 15 OH/nm^2) by UV irradiation [8,17,18]. The goal of this work is the development of microwave assisted hydrothermal synthesis

(MAHyS) of zeolite Beta (BEA) [19,20] coatings and by *in situ* conventional hydrothermal synthesis with forced heating on glass substrates to obtain a 1 μm uniform layer.

5.2 Experimental

5.2.1 Substrate modification

The experiments were carried out on 1 × 1 cm^2 surface modified glass substrates with a thickness of 1 mm. The surface roughness of the glass substrates was increased to ca. 1000 nm by sand-jet blasting [21]. Then, the zirconia and titania thin films were grown in a low pressure flow-type ALD reactor [22]. Each of the periodically repeated growth cycles included a metal precursor pulse, purge time, oxidant pulse, and another purge time. Pulsing times were 1 s and purging times were 2 s in both processes. The zirconia films with a thickness of 750 nm were grown at 573 K by using $ZrCl_4$ and H_2O as the ALD precursors in a flow of pure nitrogen gas [22,23]. The deposition rates were ca. 0.05 nm/cycle. The titania films with a thickness of 200 nm were grown at 573 K by using $TiCl_4$ and H_2O as precursors. All ALD treated substrates will be referred to according to the thickness of both zirconia and titania layers. Just before the synthesis, the TiO_2 was made superhydrophilic by UV irradiation for 3 h at room temperature in a metal box (UV lamp: Hanovia 679A-36, 450 W, λ range: 220 to 1400 nm). The contact angle of a water droplet on the modified substrates was still below 1^o up to 20 h after UV irradiation.

5.2.2 Microwave-assisted and hydrothermal synthesis

Zeolite Beta was synthesized in the presence of a nanocrystal seed solution and fluoride ions under microwave irradiation. The zeolite nanocrystals were synthesized at 373 K for 6 days from a solution of 94 SiO_2 : 1.0 Al_2O_3 : 1.35 Na_2O : 33.5 TEAOH (tetraethyl ammonium hydroxide) : 1100 H_2O [24,25]. A variation in composition was also applied. Zeolite Beta nanocrystals were obtained according to the following compositions:

I 50SiO_2 : Al_2O_3 : 1.35Na_2O : 23TEAOH : 595H_2O, 6 days, 373 K

II $50SiO_2 : Al_2O_3 : 1.35Na_2O : 28TEAOH : 640H_2O$, 6 days, 373 K

III $94SiO_2 : Al_2O_3 : 1.35Na_2O : 33.5TEAOH : 1100H_2O$, 6 days, 373 K

The solid product obtained was identified as the BEA structure having approximately 200 nm crystal size. 20 µl of a 4 wt.% aqueous colloidal suspension of zeolite Beta nanocrystals was deposited by washcoating on the substrate. The pre-seeded substrates were dried at 363 K for 10 min and then placed in the synthesis gel parallel to the gravity vector. The synthesis gel was prepared with a composition of 25 SiO_2: 1.0 Al_2O_3: 13.6 Na_2O: 8.75 TEAOH: 5 NH_4F: 290 H_2O [16]. The silica and alumina solutions were prepared separately. Colloidal silica (40%, Aldrich) and TEAOH (40%, Fluka) were mixed under continuous stirring. Sodium aluminate (Riedel-de Haën) was dissolved in demineralised water and added dropwise into a silica mixture under vigorous stirring. NH_4F (99.99%, Sigma-Aldrich) was then added and the mixture was stirred for 30 min at room temperature. The resulting gel of 50 g of was loaded in a PEEK insert which was placed in a Teflon autoclave. The autoclave was fixed tightly and placed in the microwave oven (MicroSYNTH, maximum power of 300 W). The temperature was measured via an opening in the autoclave. For comparison, zeolite Beta from the gel composition of 47 SiO_2 : Al_2O_3: 2.33 Na_2O : 1.17 K_2O : 24 TEAOH : 658 H_2O was prepared at 403 K under hydrothermal conditions. After hydrothermal synthesis, the coated substrates were rinsed with demi-water and placed into an ultrasonic bath (45 Hz) for 20 min to remove poorly bonded material. Then, the substrates were dried overnight at 383 K, calcined in an air flow for 12 h at 773 K with a heating rate of 1 K/min.

5.2.3 *In situ* hydrothermal synthesis with forced heating

In this study, the pH, Si/Al_2O_3, H_2O/Si, and $(Na+K)/Al_2O_3$ ratios were kept constant at values of 14, 47, 14 and 7, respectively. Stirring of the synthesis mixture during the reaction was not applied in this series of experiments. In order to decrease the pH of the synthesis gel, NaOH was not used in our synthesis, even though it was widely used in literature.

5.2.4 Characterization

The substrate surface roughness (R_a) was determined by Laser Scanning Confocal Microscopy (LSCM). The hydrophilicity of the titania films was evaluated by measuring the contact angle of water on the titania films using an automatic contact angle meter (Data Physics OCA 30 equipment). A droplet of demineralized water of 2.0 µl was dropped on the surface of the substrate. The contact angle of the water droplet with the substrate was determined at room humidity of 40% with the SCA 20 software.

The synthesized coatings and powders were examined by X-ray diffraction (XRD) for phase identification and crystal orientation. XRD data were collected on a Rigaku Geigerflex diffractometer using Cu Kα radiation (1.5405 Å). XRD patterns were recorded in the range of 5 – 50° 2θ using step scanning at 0.02° 2θ per step and a counting time of 4 s for each step. The intensity of the peaks at the 22-25° 2θ range after 48 h was taken as standard for calculation of the crystallinity. The coating surface coverage and crystal morphology were examined by Scanning Electron Microscopy (SEM) using a JEOL JSM-840A microscope. BET surface area and pore volume were measured with an ASAP-2000 Micromeritics equipment. The size of nanosized zeolite Beta particles was measured by Dynamic Light Scattering (DLS) with a Malvern 4700 apparatus.

5.3 Results and Discussion

5.3.1 Microwave-assisted and hydrothermal synthesis

The microwave assisted hydrothermal synthesis consists of three steps: (i) nanocrystals preparation from *in situ* hydrothermal synthesis, (ii) pre-seeding: the zeolite Beta nanocrystals, synthesized from *in situ* hydrothermal synthesis, were used as seeds and were deposited on the substrate by wash-coating, (iii) the pre-seeded substrate was placed in a microwave oven in presence of synthesis gel.

A 750 nm zirconia protective film was found to be stable in an alkali-containing mixture with a total hydroxyl concentration of 1.1 M at 423 K for at least 8

h. However, a noticeable dissolution of the glass substrates was observed already after 10 h. From a practical point of view, the ALD time above 25 h (resulting in a 750 nm zirconia film) is not feasible to apply, among others due to a non uniform growth of the film after a large number of ALD cycles. Therefore, to shorten the synthesis time to at most 10 h, the duration of the nucleation period was decreased by using the additive effect between fluoride ions and the zeolite seed solution in MAHyS.

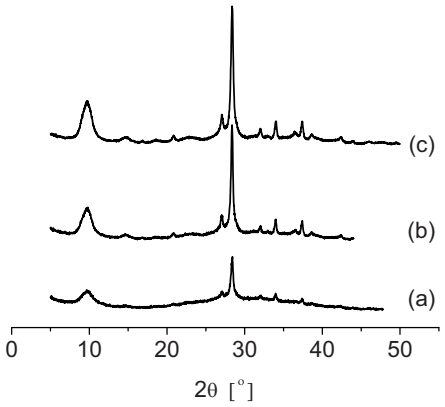

Figure 5.1. XRD patterns of zeolite Beta coating after microwave assisted hydrothermal synthesis at different synthesis time: (a) 8 hours, without pre-seeding, (b) 8 hours, with pre-seeding, (c) 10 hours without pre-seeding.

A zeolite Beta coating with a low crystallinity is obtained after 8 h under microwave irradiation. The crystallinity increases by 40% after pre-seeding of the substrate with zeolite Beta nanocrystals as shown in Figure 5.1. This confirms that seeds profoundly accelerate the crystallization rate. Almost complete crystallization of the BEA structure is achieved after 10 h with the combination of fluoride ions and seeding under microwave irradiation. Before the synthesis, the adhesion between the nanocrystals and the substrate was rather weak as they were completely removed after ultrasonication. The adhesion between the nanocrystals and the substrate was profoundly improved after MAHyS as shown in Figure 5.2.

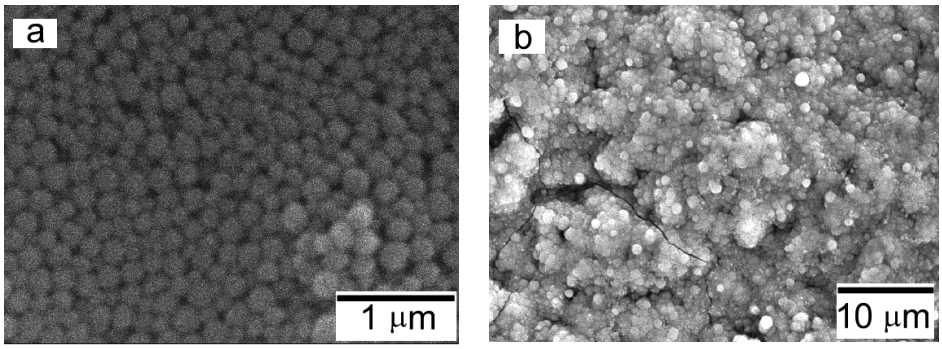

Figure 5.2. SEM images of zeolite Beta on borosilicate glass: (a) coating after MAHyS and pre-seeded nanocrystals, (b) pre-seeding the glass with nanocrystals. The solution composition was 25 SiO_2: 1.0 Al_2O_3: 13.6 Na_2O: 8.75 TEAOH: 5 NH_4F: 290 H_2O at 423 K for 8 h.

A multilayer of intergrown crystals with an average crystal size of 500 nm is observed on the substrate. The crystal size is 2.5 times larger than the size of the zeolite-nanocrystal seeds demonstrating that crystallization continues on the seeds. Additional cross-linking with the surface hydroxyl groups of the substrate is created in the course of crystallization. Without pre-seeding of the substrate with zeolite Beta nanocrystals, the complete coverage of the substrate has still not been achieved (Figure 5.3).

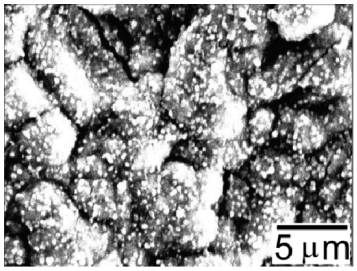

Figure 5.3. SEM images of zeolite Beta on borosilicate glass by MAHyS without pre-seeding by nanocrystals. The solution composition was 25 SiO_2: 1.0 Al_2O_3: 13.6 Na_2O: 8.75 TEAOH: 5 NH_4F: 290 H_2O at 423 K.

For comparison, zeolite Beta was prepared under conventional hydrothermal synthesis at 403 K. Based on the published data [8,13], the total OH concentration was fixed at 1.0 M, and the ratios of H_2O/Si = 14 and (Na+K)/Al_2O_3 = 7 were applied. To avoid severe dissolution of the glass substrates, NaOH was not used in the synthesis, even though its application as mineralizing agent was often reported in

literature. To prevent glass dissolution, a forced heating method was applied [26] which allowed decreasing the synthesis time in all hydrothermal *in situ* syntheses.

The synthesis of zeolite Beta coating by *in situ* hydrothermal synthesis was performed with the TEA/Al_2O_3 ratio in the range from 20 to 24 to provide the shortest synthesis time [13]. Higher synthesis temperatures resulted in a substantial dissolution of the glass substrates with the protective zirconia layer. The influence of the TEA/Al_2O_3 ratio on the XRD crystallinity and on the adhesion of the coatings with a Si/Al ratio of 23.5 was investigated. The synthesis was performed at 403 K for 48 h with TEA/Al_2O_3 ratios of 20, 22 and 24, respectively.

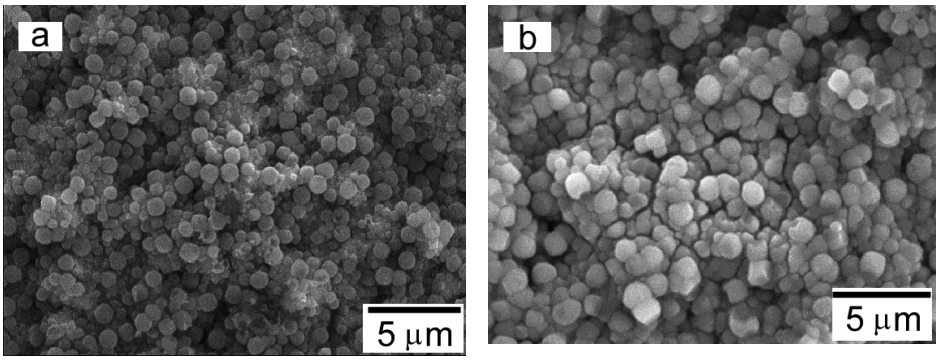

Figure 5.4. SEM images of zeolite Beta coating on borosilicate glass by conventional hydrothermal synthesis at 403 K. (a) TEA/Al_2O_3=20, (b) TEA/Al_2O_3=24. The solution composition was 47 SiO_2: 1.0 Al_2O_3: 2.33 Na_2O: 1.17 K_2O: 24 TEAOH: 658 H_2O at 403 K.

The corresponding SEM images of the coatings are shown in Figure 5.4. The coatings with TEA/Al_2O_3 ratios of 20 and 22 show weak adhesion. No zeolite Beta crystals were present on the glass substrate after 30 min ultrasonication. On the contrary, a uniform zeolite Beta coating with high adhesion was obtained at a TEA/Al_2O_3 ratio of 24. Further increase in TEA/Al_2O_3 gave a low coverage of the zeolite Beta coating.

5.3.2 Conventional *in situ* hydrothermal synthesis with forced heating

The approach to prevent glass dissolution is by decreasing the synthesis time by a fast heating method. A forced-heating model was built and applied in all *in situ*

syntheses to reduce the time to reach the equilibrium synthesis temperature. Shortening the synthesis time is aimed at to prevent glass dissolution. Without forced heating, it takes 10 h to reach the equilibrium temperature. A forced-heating model is required to decrease this period to less than 1 h and thus decreasing the glass sample dissolution. In forced-heating, the stainless steel shell of the autoclave was heated up to an elevated temperature and then the PEEK insert including synthesis at room temperature was put into the stainless steel shell, finally the whole equipment was placed into the oven (at a set temperature) immediately. The temperature of the stainless steel decreased and correspondingly the temperature of the peek insert and of the synthesis gel increased. Finally, both temperatures were equal to the temperature of the oven, and the system reached equilibrium.

The zeolite Beta coating by *in situ* hydrothermal synthesis was obtained mainly in the shortest synthesis time range (20-22.4 h) mentioned above to prevent ALD treated substrate dissolution. The influence of the ultrasonication (coating adhesion to the substrate) and TEA/Al ratio were investigated by performing the synthesis with the standard composition for 48 h at 403 K and by varying the TEA/Al Al_2O_3 ratio at 20, 22 and 24. The crystallinity of the zeolite Beta crystal was 100%, 90% and 45%, respectively. Synthesis time is also a very important parameter. In addition, the coating quality is highly depending on the quality of the ALD substrate because the samples will dissolve more during longer synthesis. All successful experiments were performed with 400 nm ZrO_2 and 400 nm TiO_2 of ALD layers. The 400 nm ZrO_2 and 400 nm TiO_2 ALD treated substrates were the only coatings which have a high quality to resist at high pH synthesis. ALD treated substrates still dissolved in even thicker protection layers, for example 500 nm ZrO_2 (400 nm TiO_2) and 750 nm ZrO_2 (50 nm TiO_2). Experiments proved that a low quality ALD treated substrate dissolved almost for 25% after 24 h synthesis at 403 K. The quality of substrates needs to be improved because *in situ* hydrothermal synthesis can not be performed on unstable substrates.

5.4 Conclusions

Microwave assisted hydrothermal synthesis (MAHyS) and conventional hydrothermal synthesis of zeolite Beta coatings on a borosilicate glass substrate have been carried out. A 750 nm zirconia layer, deposited by atomic layer deposition (ALD) from $ZrCl_4$ and H_2O precursors, provided a good protection of the glass substrate during the synthesis in a highly alkaline solution. The coatings with an average crystal size of 500 nm have been obtained in MAHyS. The synthesis time was decreased to 8 h at 423 K by using the additive effect of fluoride ions and zeolite seeds with an average particle size of 200 nm. In the absence of microwave irradiation, the hydrothermal *in situ* synthesis of zeolite Beta coatings required several days at 403 K. Higher synthesis temperatures resulted in a substantial dissolution of the glass substrates with the protective zirconia layer. The effect of synthesis conditions was investigated to decrease the synthesis time of the coating with the Si/Al ratio of 23.5. The fully crystalline coatings with a high adhesion to the substrate were obtained after 48 h from a synthesis mixture at a template to alumina ratio of 24.

In the *in situ* conventional hydrothermal synthesis method, by applying a forced heating technique to shorten the time to reach reaction temperature, the temperature of the synthesis gel reaches the reaction temperature in 30 min, which is 9 h faster than with conventional heating. Optimum conditions for the synthesis of uniform zeolite Beta coatings were found to be as follows: SiO_2/Al_2O_3=47, $TEAOH/Al_2O_3$=24.4, H_2O/SiO_2=14, $(Na+K)/Al_2O_3$=7, temperature of 403 K, and synthesis time of 48 h.

References

[1] J. Caro, M. Noack, P. Kölsch, R. Schäfer, *Micropor. Mesopor. Mater*. 38 (2000) 3-24.

[2] J.C. Jansen, J.H. Koegler, H. van Bekkum, H.P.A. Calis, C.M. van de Bleek, F. Kapteijn, J.A. Moulijn, E.R. Geus, N. van der Puil, *Micropor. Mesopor. Mater.* 21 (1998) 213-226.

[3] J.C.M. Muller, G. Hakvoort, J. C. Jansen, *J. of Thermal Anal.* 53 (1998) 449-466.

[4] M. Tather, A. Erdem-Şenatalar, *Micropor. Mesopor. Mater*. 34 (2000) 23-30.

[5] A.E.W. Beers, T.A. Nijhuis, N. Aalders, F. Kapteijn, J.A. Moulijn, *Appl. Catal. A: Gen.* 243 (2003) 237-250.

[6] E.V. Rebrov, G.B.F. Seijger, H.P.A. Calis, M.H.J.M. de Croon, C.M. van den Bleek, J.C. Schouten, *Appl. Catal. A: Gen.* 206 (2001) 125-143.

[7] A. Bueno-López, D. Lozano-Castelló, I. Such-Basáñez, J.M. García-Cortés, M.J. Illán-Gómez, C. Salinas-Martínez de Lecea. *Appl. Catal. B: Environ.* 58 (2005) 1-7.

[8] M.J.M. Mies, J.L.P. van den Bosch, E.V. Rebrov, J.C. Jansen, M.H.J.M. de Croon, J.C. Schouten, *Catal. Today*, 110 (2005) 38-46.

[9] Y.S.S. Wan, J.L.H. Chau, A. Gavrilidis, K.L. Yeung, *Micropor. Mesopor. Mater.* 42 (2001) 157-175.

[10] J.C. Jansen, E.J. Creyghton, S.L. Njo, H. van Koningsveld, H. van Bekkum, *Catal. Today* 38 (1997) 205-212.

[11] D. E. de Vos, P.A. Jacobs, *Micropor. Mesopor. Mater*. 82 (2005) 293-304.

[12] M. Lashdaf, V.-V. Nieminen, M. Tiitta, T. Venäläinen, H. Österholm, O. Krause, *Micropor. Mesopor. Mater.* 75 (2004) 149-158.

[13] M.L. Maloncy, A.W.C. van den Berg, L. Gora, J.C. Jansen, *Micropor. Mesopor. Mater.* 85 (2005) 96-103.

[14] M.J.M. Mies, E.V. Rebrov, J.C. Jansen, M.H.J.M. de Croon, J.C. Schouten, *J. Catal*. 247 (2007) 328-338.

[15] C.O. Kappe, *Angew. Chem. Int. Ed.* 43 (2004) 6250-6284.

[16] D-S. Kim, J-S. Chang, J-S. Hwang, S-E. Park, J.M. Kim. *Micropor. Mesopor. Mater.* 68 (2004) 77-82.

[17] R. Wang, N. Sakai, A. Fujishima, T. Watanabe, *Phys J. Chem. B* 103 (1999) 2188-2194.

[18] A.W.C. Van den Berg, L. Gora., J.C. Jansen, T. Maschmeyer, *Micropor. Mesopor. Mater.* 66 (2003) 303-309.

[19] M.A. Camblor, A. Corma, A. Mifsud, J. Perez-Pariente, S. Valencia. *Stud. Surf. Sci. Catal*. 105 (1997) 341-348.

[20] M.A.Camblor, A. Corma, S. Valencia. *Micropor. Mesopor. Mater.* 25 (1998) 59-74.

[21] H. Yagyu, K. Sugano, S. Hayashi, O. Tabata, J. Micromech. Microeng. 15 (2005) 1236-1241.

[22] M. Putkonen, L. Niinistö, *J. Mater. Chem.* 11 (2001) 3141-3147.

[23] M. Ritala, M. Leskelä, *Appl. Surf. Sci.* 75 (1994) 333-340.

[24] S. Mintova, M. Reinelt, T.H. Metzger, J. Senker, T. Bein, *Chem. Commun*. (2003) 326-327.

[25] L. Tosheva, V.P. Valtchev, *Chem. Mater.* 17 (2005) 2494-2513.

[26] M.J.M. Mies, E.V. Rebrov, J.C. Jansen, M.H.J.M. de Croon, J.C. Schouten, *Micropor. Mesopor. Mater.* 106 (2007) 95-106.

Chapter 6

Citral hydrogenation over Pt loaded micro- and mesoporous supports: the interplay between steric limitations and acidity

This Chapter is adapted from:
O. Muraza, E.V. Rebrov, P. Mäki-Arvela, N. Kumar, M.H.J.M. de Croon, D.Yu. Murzin, J.C. Schouten, Citral hydrogenation over Pt loaded micro- and mesoporous supports: the interplay between steric limitations and acidity *(to be submitted to Micropor. Mesopor. Mater.).*

Abstract

The effect of pore morphology and acidity on the selectivity in the hydrogenation of citral was investigated on a series of bifunctional catalysts: Pt-H-SAPO-5, Pt-H-Y zeolite, Pt-H-MCM-41, as well as on supported Pt-SiO_2. The reaction was studied in a batch reactor at 343 K with 10 bar total pressure. The highest selectivity to the unsaturated alcohols of 57% was obtained on the Pt-H-SAPO-5 catalyst at a conversion of 46%. The interplay among a monodimensional pore channel of the H-SAPO-5 support, the weak Brønsted acidity of this silico alumino phosphate, and large the platinum nanoparticles contributed to a high selectivity. The corresponding turnover frequency was 0.036 s^{-1}. Pt-H-MCM-41 showed the highest selectivity to menthol, while Pt-H-Y zeolite demonstrated the highest dehydration rate.

6.1 Introduction

Unsaturated aliphatic alcohols with an allylic double bond are important reactants in fine chemicals synthesis [1]. They can be obtained by the selective hydrogenation of α,β-unsaturated aldehydes, which is a rather difficult process as the reaction enthalpy for C=C hydrogenation is 42 kJ/mol higher than that for C=O hydrogenation [2-4]. The hydrogenation catalysts usually contain noble metals as active components. Pt, Pd, Ni, and Ru monometallic catalysts have often been applied in citral hydrogenation [5,6]. The selectivity depends strongly on the conditions during catalyst preparation as well as on the nature of the support. Silica [5], titania [6], carbon [7], carbon nanotubes [8,9], polyanilines [10], zeolites [11], and mesoporous materials [12] have been extensively studied in different structures such as thin films, monoliths, and fibers.

Selective hydrogenation of one of the α,β-unsaturated aldehydes, citral (3,7-dimethyl-2,6-octadienal), was chosen in this study as a model reaction. Citral is usually a mixture of E- and Z-isomers and it can be hydrogenated towards unsaturated aldehyde (citronellal, CAL), unsaturated alcohols (UCOL, nerol and geraniol). Subsequent hydrogenation of these products leads to citronellol (COL), and then to dimethyl octanol (DMOL), while isomerizarion of citronellal gives isopulegol (IP) (Figure 6.1).

Metal impregnated zeolites can provide shape selectivity in citral and cinnamaldehyde hydrogenation [13,14]. Only previously reported selective hydrogenation of α,β-unsaturated aldehydes on microporous zeolites will be referred as comparison with this work**.** The influence of geometric constraints in the micropores has been demonstrated in the Pt-BEA zeolite, where selectivity to cinnamylalcohol of 88% was reported [4,14]. To explain the high selectivity, the authors suggested that diffusion of an aldehyde molecule occurred parallel to the linear channel walls until it reached a Pt cluster. This makes the adsorption via a carbonyl group more probable, resulting in selective hydrogenation to the unsaturated aldehyde.

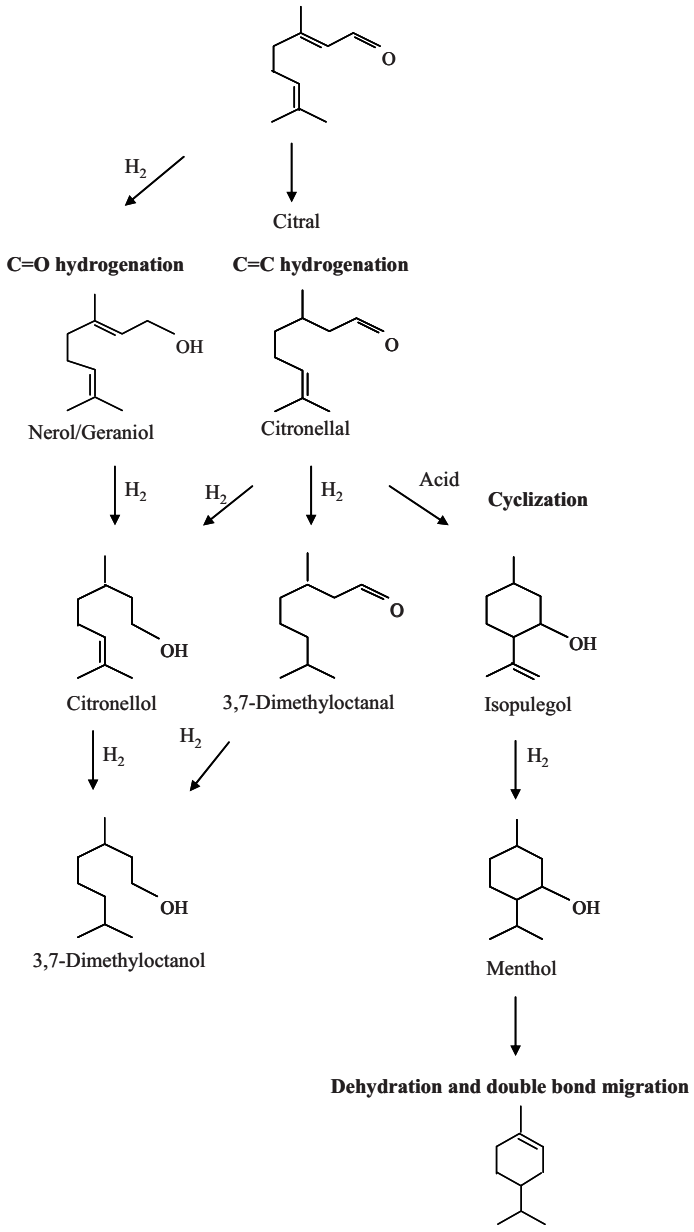

Figure 6.1. Citral and its derivatives, formed by C=O hydrogenation, C=C hydrogenation, cyclization, dehydration and double bond migration.

A similar effect was observed on a Ru-LTL zeolite catalyst which has a one-dimensional microporous network with a channel diameter of 0.71 nm. A selectivity to nerol and geraniol of 40% was reported at a citral conversion of 60% at 323 K under 50 bar pressure with 2-propanol as solvent [13].

Aluminium-phosphate-based microporous molecular sieves with a one-dimensional framework structure are other potential candidates for selective hydrogenation of α,β-unsaturated aldehydes. The nature of their weak acidic properties has been extensively investigated [15] since their first appearance in the literature [16-18]. H-SAPO-5 has 12-membered rings with an aperture of 0.73 nm in diameter (AFI topology) [19]. On metal-containing H-SAPO-5, the acid as well as the redox properties can be utilized for catalysis. The acidity of H-SAPO-5 can be tuned by changing the Al content resulting in new isomerization routes similar to that reported on Beta and Y zeolites and H-MCM-41 [11,20].

This paper focuses on the effect of pore morphology and acidity of Pt-H-SAPO-5 and H-SAPO-5 molecular sieves with an AFI structure and their influence on the catalytic performance in citral hydrogenation to unsaturated alcohols. The activity of H-SAPO-5 supported Pt catalyst was investigated and compared with that of Pt-H-Y, Pt-H-MCM-41, and Pt-SiO_2 used as reference catalysts. Pt-H-Y exhibits the FAU (faujasite) structure. It has a 3-dimensional pore structure with pores running perpendicular to each other and has a strong acidity. Pt-H-MCM-41 has a one-dimensional framework structure with a weak acidity. Pt-SiO_2 represents an amorphous oxide, standard support material with virtually no acidity.

6.2 Experimental

6.2.1 Catalyst synthesis

H-SAPO-5 was synthesized according to the procedure by Campelo et al. [21] with several adjustments. The precursors in the synthesis of H-SAPO-5 were phosphoric acid (Merck, 85 wt.%), hydrated aluminium oxide (Vista, 74.2 wt.% Al_2O_3, and 25.8 wt.% H_2O), fumed silica (Aldrich), tri-*n*-propylamine (Merck), and distilled water. A gel solution was prepared and poured into a Teflon coated stainless steel autoclave and the synthesis was carried out at 473 K for 24 h under static condition [11]. H-MCM-41 was synthesized using fumed silica (Aldrich), tetramethyl ammonium silicate (Sachem), sodium silicate (Merck), tetradecyl trimethyl

ammonium bromide ($CH_3(CH_2)_{13}N(CH_3)_3Br$, Aldrich), and aluminium isopropoxide (Aldrich) by a method described in [22]. H-Y zeolite was obtained by calcination of NH_4-Y (Zeolyst International). The supported platinum catalysts were prepared by impregnation of the corresponding supports with H_2PtCl_6 (40 wt.%, Degussa) in a rotary evaporator for 24 h.

6.2.2 Catalyst characterization

The acidity of the supports was studied on a ATI Mattson FT-IR spectrometer by pyridine adsorption. A 10 mg/cm^2 thin tablet of the catalyst was evacuated at 450^{o}C for 1 h. Pyridine (≥ 99.5 wt.%) was adsorbed at 373 K for 30 min. The desorption was carried out at 473 K. The amount of adsorbed pyridine was calculated based on the molar extinction coefficient [23]. The BET surface area was measured by a nitrogen adsorption at 77 K in an ASAP 2010 instrument (Micromeritics). A desired quantity of catalyst powder (1.0 to 5.0 wt.%) was outgassed at 573 K for 4 h prior to the measurements. XRD data were collected on a Rigaku Geigerflex Max/B diffractometer (40 kV, 40 mA) with Cu Kα radiation (using continuous scanning at 0.02^o 2θ and a counting time of 0.5 s / scan step).

The morphology of the catalysts was determined by transmission electron microscopy (TEM). High resolution transmission electron microscopy (HR-TEM) images were recorded on a FEI Tecnai TF20 electron microscope operated at 200 kV. The collected powders were grinded and dispersed in ethanol. The suspension was mounted gently to a holey amorphous carbon film on a Ni or Cu grid. The particle size distribution (PSD) was obtained by measuring 100 particles from the TEM micrographs. The mean particle diameter was calculated by the following formula: $d_m = \frac{1}{100}\sum_{i=1}^{100} n_i d_i$, where n_i is the number of particles with diameter d_i. The dispersion, $\%D$, of the metal nanoparticles was measured by CO pulse chemisorption. In case of Pt-H-SAPO-5, the dispersion was estimated from the mean particle diameter obtained from the TEM micrographs by the formula: $\%D = \frac{C_1}{d(nm)}$, where C_1 is equal to 108 for supported platinum catalysts [24].

6.2.3 Catalytic testing

Prior to reaction, the catalysts (300 mg, 1.0-5.0 wt.%)) were reduced *in situ* by hydrogen (AGA, 99.999%) at 673 K for 60 min. Then, the reactor, an autoclave (Autoclave Engineers), was cooled to the reaction temperature. A mixture of 0.01 M citral (Lancaster 5460, 97 wt.%) in cyclohexane of 200 cm^3 was stripped form oxygen and fed to the reactor. The reaction was carried out in the batch mode at 343 K under 10 bar total pressure at a stirring rate of 1500 rpm. Since vigorous stirring and small catalyst particle sizes (< 90 μm) were applied, the mass transfer resistance could be eliminated [25]. The metal to substrate molar ratio was 20 to 65 in all experiments. Sampling volumes of 1 cm^3 were selected for analysis after desired time intervals. The reactants and products were analyzed by a gas chromatograph equipped with a DB-1 capillary column (length: 30 m, internal diameter: 0.25 mm, film thickness: 0.50 μm). The temperatures of injector and detector were 523 K and 573 K, correspondingly.

6.3 Results and discussion

6.3.1 Characterization of the catalysts

The Y zeolite demonstrated the highest concentration of Brønsted acid sites (Table 6.1). The acidity of H-MCM-41 and H-SAPO-5 was respectively three and nine time less than that of Y zeolite, while the silica support showed no Brønsted acidity. The concentration of Lewis acid sites on Y zeolite and H-MCM-41 was considerably higher than that on H-SAPO-5 and SiO_2. Introducing metal on the support usually diminishes the number of strongest acid sites [26]. The structure of the micro- and microporous materials, i.e. zeolite Y, H-SAPO-5 and MCM-41 was confirmed by XRD; it remained untagged after Pt loading [27,28].

The BET specific surface area of the supports and catalysts are given in Table 6.1. To be noted, it can be seen that the BET surface area of H-MCM-41 was lower than that of Pt-H-MCM-41, which can be explained by the opening of the micropores in the mesoporous material during catalyst preparation; the heat treatment may have opened micropores in the mesoporous material. The specific surface area of the

catalysts decreased in the following order: Pt-H-MCM-41 > Pt-H-Y > Pt-SiO_2 > Pt-H-SAPO-5 (Table 6.1). The relatively low surface area of the SiO_2 support was corresponding to its amorphous nature. Pt-SiO_2 has the highest metal loading of 5.0 wt.% and the lowest Pt specific surface area resulting in the lowest Pt dispersion [29]. The Pt-H-SAPO-5, Pt-H-MCM-41, and Pt-H-Y catalysts have a moderate specific Pt surface area and a Pt dispersion in the range of 21 to 29%.

The nitrogen adsorption-desorption isotherms of the H-SAPO-5 support and of the Pt-H-SAPO-5 catalyst are shown in Figure 6.2. The initial part of the isotherms corresponds to micropore filling. The subsequent adsorption up to a relative pressure of 0.37 occurs on the outer surface and in the mesopores. An uptake in the adsorption branch of the isotherms in the range of relative pressures between 0.4 and 0.9 corresponds to mesopore filling. Above a relative pressure of 0.9, adsorption takes place mainly on the outer surface and in the macropores which were produced during the pelletizing of the powders [30,31]. It can be seen that the H-SAPO-5 support has a higher mesopore contribution (0.040 cm^3/g) as compared to the Pt-H-SAPO-5 (0.016 cm^3/g) catalyst.

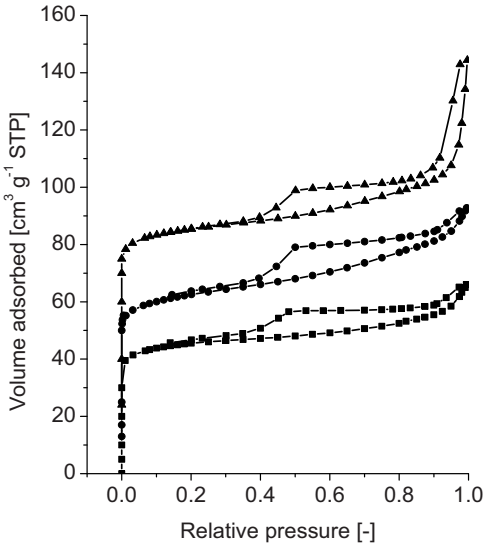

Figure 6.2. N_2 adsorption-desorption isotherms of H-SAPO-5 (▲), Pt-H-SAPO-5, Fresh (♦) and Spent (■). Pt-H-SAPO-5, Fresh (♦) isotherms were shifted by 10 cm^3/g STP and H-SAPO-5 isotherms were shifted by 20 cm^3/g STP along the Volume adsorbed axis to obtained well separated isotherms for presentation purposes.

Table 6.1. Catalyst characterization data.

Catalyst	Acid site concentration of the support (μmol/g_{cat}) [a]		Specific surface area of the support (m^2/g_{cat})	Specific surface area of the catalyst (m^2/g_{cat})	Support mean pore size (nm)	Pt loading (wt.%)	Specific Pt surface area (m^2/g_{Pt})	Pt dispersion, (%)
	Brønsted	Lewis						
Pt-H-Y	291	165	1218[c]	1088 [c]	0.74	3.8	78	29
Pt-H-MCM-41	89	168	902 [b]	1189 [b]	3.0	2.5	67	24
Pt-H-SAPO-5	27	32	220 [b]	178 [b]	0.73	1.0	n.d.	21
Pt-SiO_2	0	7	n.d.	412[b]	6.0	5.0	17	5

[a] desorption at 523 K, [b] BET equation, [c] Dubinin equation
n.d. not determined

After Pt deposition, the BET surface area decreased from 220 to 178 m^2/g (Table 6.1). However, the accessibility of the microporous network was not affected by Pt impregnation. The micropore contribution of 124 m^2/g remained unchanged after Pt deposition. The mesopore contribution was considerably reduced from 96 to 54 m^2/g due to partial pore blockage by Pt agglomerates. The Pt-H-SAPO-5 catalyst has a wide distribution of Pt nanoparticles in the range between 2 and 80 nm (Figure 6.3 (a), (b), and (c)). The Pt particle sizes can be combined into four groups: 2-4 nm (small), 5-11 nm (medium), 15-20 nm (large), and 50-80 nm (giant).

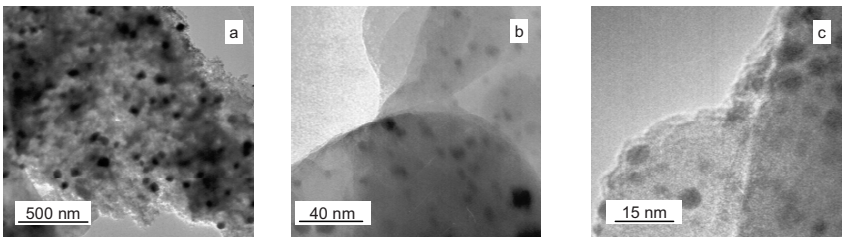

Figure 6.3. TEM images of (a) fresh Pt-H-SAPO-5, (b) magnification of fresh Pt-H-SAPO-5, and (c) spent Pt-H-SAPO-5.

6.3.2 Activity of the catalysts

The hydrogenation and the dehydration followed by double bond migration routes in citral transformation (Figure 6.1) can occur simultaneously and their rates determine the selectivity and the deactivation rate of the catalysts. Dehydration products were typically formed via dehydration of isopulegol or menthol followed by double bond isomerization and thus they consisted of C10 cyclic, unsaturated structures, such as 1-methyl-4-propyl-cyclohexene (Figure 6.1).

Some of the by-products could also be formed by consecutive dehydrogenation to form menthatriene type compounds [11]. The presence of gas-phase low molecular weight hydrocarbons was not analyzed. The adsorption of the dehydration products on the walls of the support porous network leads to fast catalyst deactivation. Therefore, the contribution of each route to the overall conversion of citral was

evaluated before a detailed activity study on four types of the supported Pt catalysts was carried out (Figure 6.4).

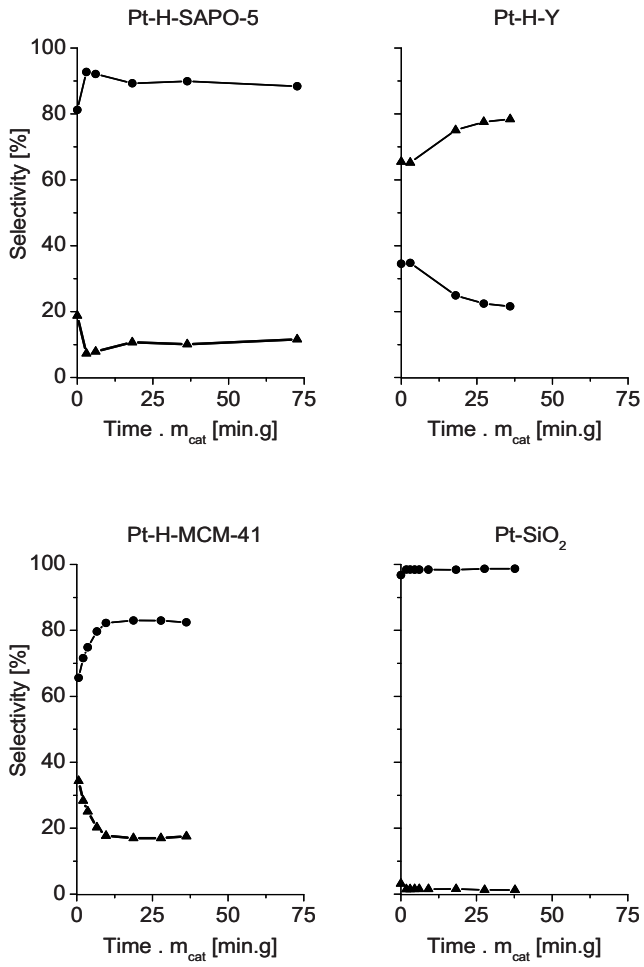

Figure 6.4. Selectivity towards hydrogenation (●) and dehydration and double bond migration (▲) over Pt-H-SAPO-5, Pt-H-Y, Pt-H-MCM-41, and Pt-SiO_2 at 343 K under 10 bar total pressure in cyclohexane. The initial citral concentration was 0.01 M.

The initial hydrogenation and dehydration rates are listed in Table 6.2. For ease of comparison, the selectivity and concentration profiles in Figures 6.4 to 6.8 are normalized to 1 gram of Pt. Citral can be strongly adsorbed on the acid sites [11]. It can be seen that the dehydration selectivity is in line with the acidity of the supports.

Table 6.2. Kinetic data from citral hydrogenation.

Catalyst	TOF after 120 min (s^{-1})	Initial overall rate (mmol/min/g_{cat})	Initial reaction rate (mmol/min/g)		Selectivity at 50% conversion (%)		
			[a]Hydrogenation (mmol/min/g_{Pt})	Dehydration (mmol/min/g_{cat})	S_{UCOL}[b]	S_{CAL}	S_{DH}
Pt-H-Y	0.016	0.95	8.7	0.62	0	2	67
Pt-H-MCM-41	0.030	0.20	4.0	0.1	4	10	27
Pt-H-SAPO-5	0.036	0.11	2.8	0.08	57	4	13
Pt-SiO_2	0.072	0.76	15	0	0	54	0

[a]Hydrogenation rate is presented in mmol/min/g_{Pt} unit (not in mmol/min/g_{cat}) as hydrogenation is controlled by the metal nanoparticles.
[b]where CAL is citronellal, UCOL is nerol + geraniol, and DH = dehydration and double bond migration products.

The dehydration and double bond migration dominates over hydrogenation on the Pt-Y catalyst. Its contribution considerably decreases on the Pt-H-MCM-41 and further on the Pt-H-SAPO-5 catalysts, while its contribution can be neglected on Pt-SiO_2. An increase of the dehydration rate with an increase of Brønsted acidity was also reported over nickel supported H-MCM-41 and H-Y catalysts [11].

It is well known that hydrogenation occurs on the metal sites while dehydration occurs on the acid sites. Therefore, the hydrogenation rates will be given per unit of Pt weight while the dehydration rates will be given per unit of support weight, hereafter.

The turnover frequency (TOF) after a reaction time of 30 min was in the range of 0.02 to 0.07 s^{-1}. The TOF decreased in the following order: Pt-SiO_2 > Pt-H-SAPO-5, Pt-H-MCM-41 > Pt-H-Y (Table 6.2). To be noted, the high TOF of Pt-SiO_2 can be related to the large pore size of the support. It was well documented [36] that the pore size of the amorphous SiO_2 (6 nm) was two times larger than that of the mesoporous H-MCM-41 and nine times larger than that of microporous zeolites. Whereas, the pore size of H-MCM-41 was approximately three times higher that of H-SAPO-5 and H-Y.

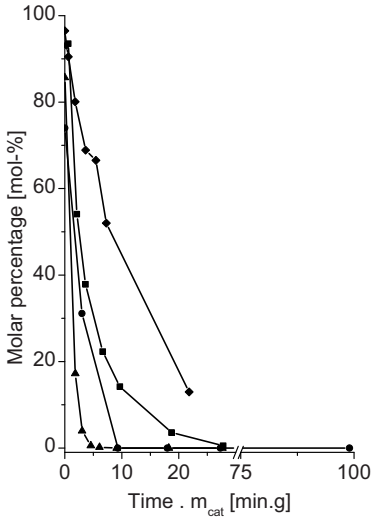

Figure 6.5. Citral molar percentage as a function of time over Pt-H-SAPO-5 (♦), Pt-H-Y (●), Pt-H-MCM-41 (■), and Pt-SiO_2 (▲).

Full citral conversion over Pt-SiO_2, Pt-H-Y and Pt-H-MCM-41 was reached within 25 min (Figure 6.5). However, full conversion over Pt-SAPO-5 was not reached within this reaction time due to the fast catalyst deactivation. The BET surface area of the Pt-H-SAPO-5 catalyst decreased from 178 to 154 m^2/g after reaction, mainly due to a decrease in the mesopore surface area from 54 to 36 m^2/g. In other words, about one third of the initial mesopore area was not accessible for nitrogen after the reaction. The micropore surface area of the spent Pt-H-SAPO-5 catalyst of 118 m^2/g and the micropore volume of 0.054 cm^3/g remained relatively unchanged. The Pt-H-SAPO-5 catalyst after the reaction showed a narrow distribution of predominantly spherical nanoparticles in the range from 5 to 11 nm (Figure 6.3 (c)). Therefore, neither partial pore blocking nor metal sintering can be responsible for such rapid deactivation. Most probably deactivation is caused by decarbonylation of citral and its hydrogenation products, resulting in strongly adsorbed CO and other carbon fragments [32].

Full citral conversion over Pt-H-Y occurred after 10 min with a substantial contribution from the dehydration route. The selectivity to the dehydration products at 50% conversion was 67%. The citral conversion over Pt-H-MCM-41 was 62% after a reaction time of 10 min. Then, the reaction proceeds much slower. The presence of the Brønsted acid sites was required to achieve high conversion of citral over Ni-H-MCM-41 [11,33]. Compared with the micro- and mesoporous support catalyst, the activity of Pt-SiO_2 with an amorphous support was the highest as shown by the highest TOF and the highest initial hydrogenation rate. There were no dehydration products over Pt-SiO_2 due to the absence of acidity.

6.3.3 Selectivity in citral hydrogenation

In citral hydrogenation one of the most important issues regarding catalyst development is to compare chemoselective hydrogenation, i.e. hydrogenation of carbonyl and ethylenic functionalities, respectively. This was performed here in two ways, i.e. by calculating the ratio of the initial rates for formation of nerol and

geraniol to that of citronellal $\left(\frac{r_{0,\,C=O}}{r_{0,\,C=C}}\right)$, and by reporting selectivities. The ratio between the initial formation rates of nerol and geraniol to citronellal decreased in the following order: Pt-H-SAPO-5 (2.0) > Pt-H-MCM-41 (0.4) > Pt/SiO_2 (0.03) > Pt-H-Y (0), indicating that Pt-H-SAPO-5 was five-fold more active in the hydrogenation of carbonyl bond than Pt-H-MCM-41, which was the second most active catalyst for hydrogenation of the carbonyl bond. The selectivities towards the main hydrogenation products, nerol and geraniol, citronellal, citronellol, 3,7-dimethyl-octanal, 3,7-dimethyl-octanol, isopulegol, menthol and towards the dehydration products, are listed in Tables 6.2 and 6.3. It should be noted that the sum of the selectivities of the seven main products is often less than 100% due to formation of small amounts of other isomerization by-products, e.g. neomenthol, isomenthol and menthones, which selectivities were not included in further consideration.

Comparison of the formation of various products, both hydrogenation and cyclisation products over different catalysts is depicted in Figures 6.6 and 6.7. In the absence of steric limitations and strong acid sites, the supported Pt catalysts are selective in C=C hydrogenation [32]. Hydrogenation of the conjugated C=C bond to citronellal was the main route over Pt-H-MCM-41 and Pt-SiO_2. The selectivity to the unsaturated alcohols was below 5%. The selectivity towards the undesired dehydration and double bond migration products was 18% over Pt-H-MCM-41 at full conversion of citral.

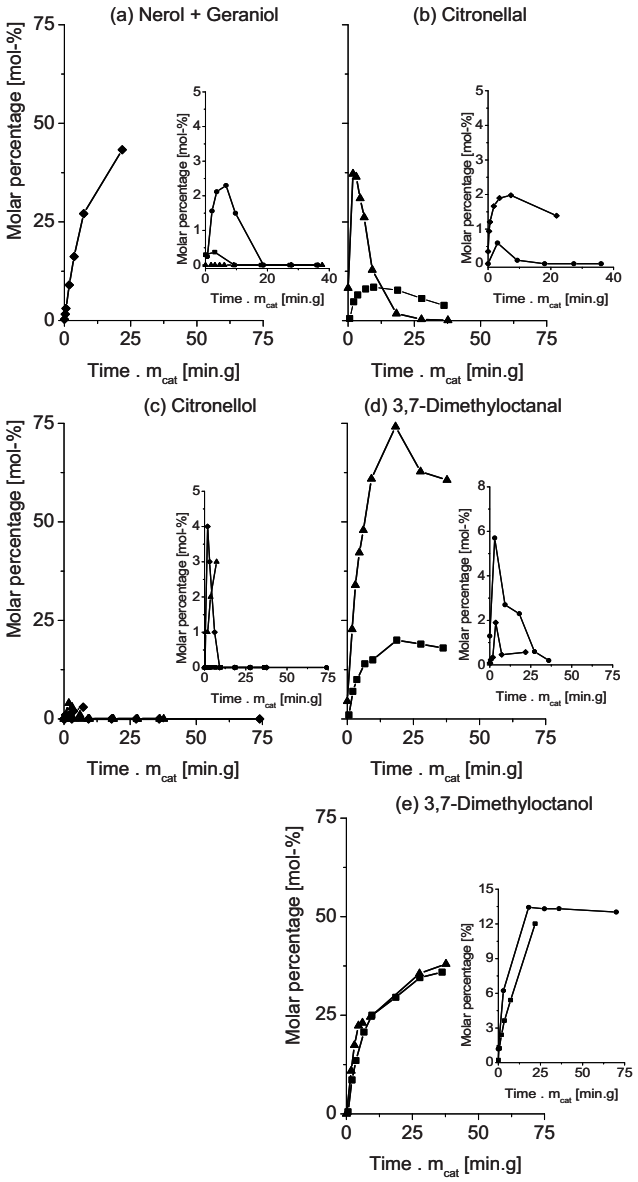

Figure 6.6. (a) Molar percentage of nerol and geraniol, (b) molar percentage of citronellal, (c) molar percentage of citronellol, (d) molar percentage of 3,7-dimethyl-octanal, and (e) molar percentage of 3,7-dimethyl-octanol in citral hydrogenation over Pt-H-SAPO-5 (♦), Pt-H-Y (●), Pt-H-MCM-41 (■), and Pt-SiO_2 (▲).

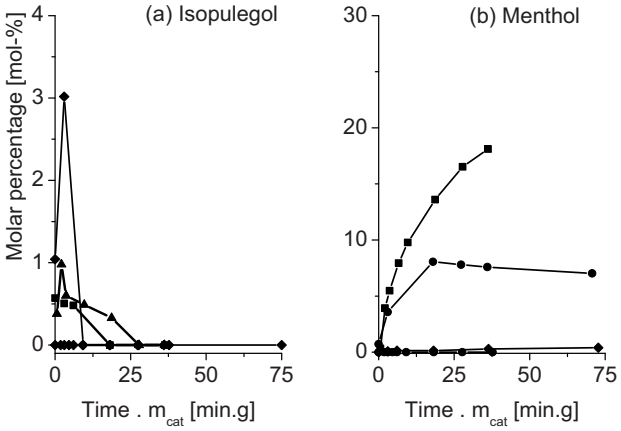

Figure 6.7. (a) Molar percentage of isopulegol, and (b) molar percentage of menthol in a 300 min prolonged citral hydrogenation over Pt-H-SAPO-5 (♦), Pt-H-Y (●), Pt-H-MCM-41 (■), and Pt-SiO_2 (▲).

The most selective catalyst towards nerol and geraniol from the four studied catalysts was the bifunctional Pt-H-SAPO-5, giving nerol and geraniol with a selectivity towards 57% at a citral conversion level of 46% (Table 6.3). This value was higher than that previously reported on a monodimensional LTL zeolite [13]. The overall kinetics for citral hydrogenation over Pt-H-SAPO-5 is shown in Figure 6.8 (a), in which exceptionally high formation rates for nerol and geraniol compared to those for the formation of citronellal and 3,7-dimethyl-octanal are clearly visible. Furthermore, citronellol was hydrogenated rapidly to 3,7-dimethyl-octanol. An increase of selectivity to the unsaturated alcohols with the increase of citral conversion over Pt-SAPO-5 (Figure 6.8 (b)) occurred up to about 46% conversion, thereafter the selectivity decreased due to the consecutive hydrogenation. This curve shape is exceptional, since a typical selectivity curve for a consecutive reaction is similar to that of Pt-H-MCM-41 (Figure 6.8 (b)), in which the selectivity of an intermediate product started to decrease with increasing conversion. An increasing selectivity to the unsaturated alcohols as a function of conversion has been previously reported for citral [13] and for cinnamaldehyde [34]. This exceptionally selectivity increase on the conversion can be caused by multicentred adsorption

where the steric constrains induced by the H-SAPO-5 monodimensional pores influence the number of sites available for adsorption of carbonyl and carbon double bond on Pt-H-SAPO-5 [35].

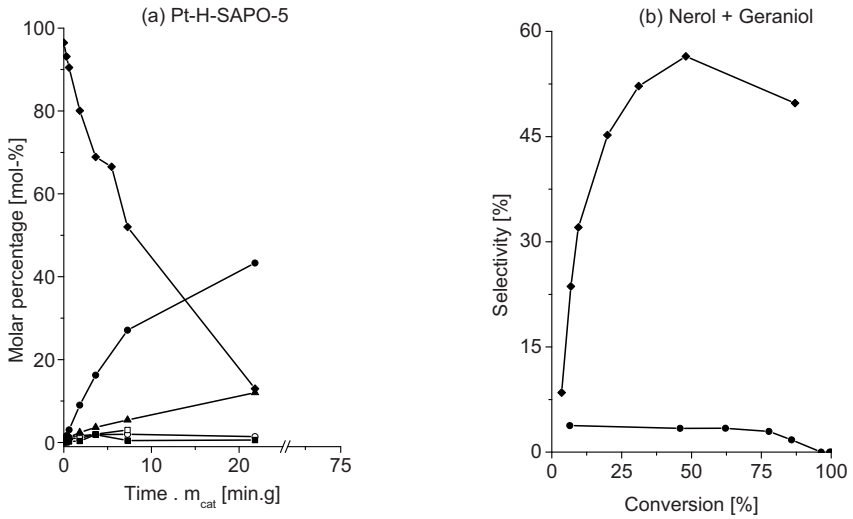

Figure 6.8. (a) Kinetics of citral (♦) hydrogenation over Pt-H-SAPO-5, formation of nerol and geraniol (●), 3-7, dimethyl-octanol (▲), citronellol ( ), citronellal (O), and menthol (Δ), (b) selectivity of nerol and geraniol as a function of conversion over Pt-H-SAPO-5 (♦) and Pt-H-MCM-41 (■).

The steric limitations of the citral molecule with a molecular diameter of 0.58 nm [36] confined in the monodimensional pores of Pt-H-SAPO-5 with a diameter of 0.73 nm, induce an end-on C=O adsorption mode [14]. As a result, the selectivity to citronellal over Pt-H-SAPO-5 was below 7% while a substantial amount of isomerization products (isopulegol) were also produced on the acid sites.

Hydrogenation of the isolated C=C bond rather than of the C=O bond occurred in the second hydrogenation step over both Pt-H-MCM-41 and Pt-SiO_2 catalysts (Figure 6.6). As a result, a low selectivity to citronellol and a moderate selectivity to 3,7-dimethyl octanal were observed at larger reaction times. 3,7-dimethyl-octanol was formed either via hydrogenation of citronellal or via hydrogenation of nerol and geraniol to citronellol. At longer reaction times,

citronellol and 3,7-dimethyl octanal were further hydrogenated on the supported Pt catalysts towards 3,7-dimethyl-octanol (Figure 6.8 (a)). Thus, if reaction time allows, hydrogenation on the supported Pt catalysts always proceeds towards the fully hydrogenated products in the absence of steric limitations. The highest selectivity to 3,7-dimethyl-octanol of 42% was observed on the macroporous Pt-SiO_2 catalyst. It is also possible to stop the reaction after the second hydrogenation step (citronellol) using Ni as an active metal [37,38].

Table 6.3. Selectivity of selected main products in citral hydrogenation over Pt-H-SAPO-5, Pt-H-MCM-41, and Pt-SiO_2 catalysts.

Catalyst	X_{citral} [a] [-]	CAL	UCOL	COL	DMAL	DMOL	IP	MT	∑
Pt-H-SAPO-5	25	7	48	6	2	13	2	6	84
	46	4	57	6	1	13	2	3	82
	75	2	52	9	1	12	1	3	80
	87[b]	2	50	10	1	11	1	3	78
Pt-H-MCM-41	25	9	4		11	13	4	18	60
	50	10	4	-	15	19	2	14	63
	75	10	3	-	17	26	1	15	72
	99	6	-	-	19	34	1	23	83
Pt-SiO_2	25	56	-	1	30	2	2	-	91
	50	51	-	3	29	6	1	-	90
	75	47	-	5	28	12	-	-	92
	99	32	-	1	42	22	-	-	97

[a]where X is conversion, CAL = citronellal, UCOL = nerol + geraniol, COL = citronellol, DMAL = 3,7-dimethyl-octanal, DMOL = 3,7-dimethyl-octanol, IP = isopulegol, and MT = menthol. ∑ is the total selectivity for the main products excluding other menthols such as isomenthol and neomenthol.

[b]the experiment was carried out until conversion of 87%.

However, not all citral was hydrogenated towards citronellol over the bifunctional Pt-H-MCM-41 and Pt-H-Y catalysts. The product of the first hydrogenation step, citronellal, was isomerized to isopulegol on the acid sites and further hydrogenated to menthol at longer reaction times [38-41]. The concentration of menthol as a function of citral conversion is shown in Figure 6.7 (b). The highest selectivity to menthol of 18% was observed on the Pt-H-MCM-41 catalyst at a citral conversion of 25% (Table 6.3). Unlike Ni-H-MCM-41, platinum supported H-MCM-

41 was not selective to menthol at long reaction times [12] due to the fast subsequent hydrogenation of citronellol to 3,7-dimethyl-octanol. The most acidic catalyst (Pt-H-Y) was also not selective in menthol formation due to considerable conversion of citral towards dehydration products (e.g. menthatrienes) which were the main products with a selectivity of 70% at full citral conversion (Table 6.3). The highest selectivity to menthol was 7%. The selectivity to isopulegol over the Pt-H-SAPO-5 and Pt-SiO_2 catalysts was below 2%.

6.4 Conclusions

The hydrogenation of citral was investigated on a series of bifunctional catalysts: Pt-H-Y zeolite, Pt-SAPO-5, Pt-MCM-41, as well as on a supported Pt-SiO_2 catalyst. The initial reaction rate in terms of TOF was the highest on the macroporous Pt-SiO_2 catalyst, followed by the micro-mesoporous Pt-H-MCM-41 and Pt-H-SAPO-5, and finally the microporous Pt-H-Y. The acid site concentration decreased in the reversed order. In this way, the H-Y support showed the highest activity in dehydration and double bond migration, which was due to its highest concentration of Brønsted acid sites. H-SAPO-5 was the most selective support for hydrogenation towards the unsaturated alcohols with a selectivity of 57% at the conversion level of 46%. A unique combination of a monosized pore diameter, weak Brønsted acidity, and a large Pt particle size contributed to a high selectivity. However, rapid deactivation occurred on this support due to adsorption of the dehydration products and partial pore blocking. The most selective catalyst for the formation of menthol was Pt-H-MCM-41. However, on this catalyst, the parallel dehydrogenation reaction still consumed 18% of citral, while the deactivation rate was less pronounced as compared with H-SAPO-5. Further tuning of the support properties is required for one-pot transformation of citral to menthol.

References

[1] H. Surburg, J. Panten, *Common Fragrance and Flavor Materials: Preparation, Properties and Uses*, 5th Ed., Wiley-VCH, Berlin, 2006.

[2] E.J. Creyghton, R.S. Downing, *J. Mol. Catal. A: Chem*. 134 (1998) 47-61.

[3] P. Mäki-Arvela, J. Hajek, T. Salmi, D. Yu. Murzin, *Appl. Catal A: Gen.* 292 (2005) 1-49.

[4] P. Claus, *Top. Catal*. 5 (1998) 51-62.

[5] (a) U.K. Singh, M.A. Vannice *J. Catal*. 191 (2000) 165-180. (b) U.K. Singh, M.N. Sysak, M.A. Vannice, *J. Catal.* 191 (2000) 181-191. (c) U.K. Singh, M.A. Vannice. *J. Catal.* 199 (2001) 73-84.

[6] R. Malathi, R. P. Viswanath, *Appl. Catal. A: Gen.* 208 (2001) 323-327.

[7] S. Galvagno, C. Milone, A. Donato, G. Neri, R. Pietropaolo, *Catal. Lett*. 18 (1993) 349-355.

[8] E. Asedegba-Nieto, A. Guerrero-Ruiz, I. Rodríguez-Ramos, *Carbon* 44 (2006) 799-823.

[9] G. Guo, F. Qin, D. Yang, C. Wang, H. Xu, S. Yang, *Chem. Mater*. 20 (2008) 2291-2297.

[10] M. Steffan, F. Klasovsky, J. Arras, C. Roth, J. Radnik, H. Hofmeister, P. Claus, *Adv. Synth. Catal.* 350 (2008) 1337-1348.

[11] P. Mäki-Arvela, N. Kumar, D. Kubička, A. Nasir, T. Heikkilä, V-P. Lehto, R. Sjöholm, Tapio Salmi, D. Yu. Murzin, *J. Mol. Catal. A: Chem.* 240 (2005) 72-81.

[12] M. Guisnet, M. Guidotti, One-pot Reactions on Bifunctional Catalysts, in *Catalysts for Fine Chemical Synthesis, Microporous and Mesoporous Solid Catalysts*, Vol. 4, E.G. Derouane (Ed.) 165-166, John Wiley & Sons, Chichester (2006).

[13] (a) J. Alvarez-Rodriquez, A. Guerrero-Ruiz, I. Rodriguez--Ramoz, A. Arcoya, *Micropor. Mesopor. Mater*., 110 (2008) 186-196. (b) J. Álvarez-Rodríguez, A. Guerrero-Ruiz, I. Rodríguez-Ramos, A. Arcoya-Martín, *Catal. Today* 107-108 (2005) 302-309.

[14]. P. Gallezot, B. Blanc, D. Barthomeuf, M.I. Païs da Silva. *Stud. Surf. Sci. Catal.* 84 (1994) 1433-1439.

[15] B. Parlitz, E. Schreier, H.L. Zubowa, R. Eckelt, E. Lieske, G. Lischke, R. Fricke. *J. Catal.* 155 (1995) 1-11.

[16] B.M. Lok, C.A. Messina, R.L. Patton, R.T. Gajek, T.R. Cannan, E.M. Flanigen, US Patent No. 4 440 871, 1984.

[17] S.T. Wilson, E.M. Flanigen, US Patent No. 4 567 029, 1986.

[18] B.M. Lok, C.A. Messina, R. L. Patton, R.T. Gajek, T.R. Cannan, E.M. Flanigen *J. Am. Chem. Soc*. 106 (1984) 6092-6093.

[19] W. M. Meier, D. H. Olson, Ch. Baerlocher, in *Atlas of Zeolite Structure Types*, Elsevier, Amsterdam, 4th Ed., 1996.

[20] J.A. Martens, C. Janssens, P.J. Grobet, H.K. Beyer, P.A. Jacobs In: P.A. Jacobs, R.A. Van Santen, Eds., *Zeolites: Facts, Figures, Future*, *Stud. Surf. Sci. Catal.* 49A (1989) 215.

[21] J.M. Campelo, F. Lafont, J.M. Marinas, *J. Catal.* 156 (1995) 11-18.

[22] J.S. Beck, J.C. Vartuli, W.J. Roth, M.E. Leonowicz, C.T. Kresge, K.D. Schmitt, C.T. Chu, D.H. Olson, E.W. Sheppard, S.B. McCullen, J.B. Higgins, J.L. Schlenker, *J. Am. Chem. Soc.* 114 (1992) 10834–10843.

[23] C.A. Emeis, *J. Catal.* 141 (1993) 347-354.

[24] C.H. Bartholomew, R.J. Farrauto, *Fundamentals of Industrial Catalytic Processes*, 2nd Ed., John Wiley, 2006.

[25] R.A. van Santen, P.W.M.N. van Leeuwen, J.A. Moulijn, B.A. Averlill, Eds. *Catalysis: An Integrated Approach*, 2nd Ed., *Stud. Surf. Sci. Catal.* 123, Elsevier, Amsterdam. 1999, 375.
[26] D. Kubička, N. Kumar, T. Venäläinen, H. Karhu, I. Kubickova, D. Yu. Murzin, *J. Phys. Chem. B* 110 (2006) 4937-4946.
[27] D. Kubička, N. Kumar, P. Mäki-Arvela, T. Venäläinen, M. Tiitta, T. Salmi, D. Yu. Murzin, *Stud. Surf. Sci. Catal.* 158B (2005) 1669-1676.
[28] E. Toukoniitty, B. Ševčíková, N. Kumar, P. Mäki-Arvela, T. Salmi, J. Väyrynen, T. Ollonqvist, P. Kooyman, *Stud. Surf. Sci. Catal*. 135 (2000) 23-P-15.
[29] P. Mäki-Arvela, N. Kumar, I. Paseka, T. Salmi, D. Yu. Murzin, *Catal. Lett*. 98 (2004) 173-179.
[30] B. Boddenberg, V.R. Rani, R. Grosse, *Langmuir* 20 (2004) 10962-10969.
[31] K.S.W. Sing, D.H. Everett, R.A.W. Haul, L. Moscou, R.A. Pierotti, J. Rouquerol, T. Siemieniewska, *Pure Appl. Chem.* 57 (1985) 603-619.
[32] M. Burgener, R. Wirz, T. Malat, A. Baiker, *J. Catal.* 228 (2004) 152-161.
[33] PG.N. Mertens, F. Verpoort, A-N. Parvulescu, D.E. De Vos, *J. Catal.* 243 (2006) 7-13.
[34] J. Hajek, N. Kumar, P. Mäki-Arvela, T. Salmi, D.Yu. Murzin, I. Paseka, T. Heikkilä, E. Laine, P. Laukkanen and J. Väyrynen, *Appl. Catal. A: Gen.* 251 (2003) 385-396.
[35] D.Yu. Murzin, H. Backman, *React. Kinet. Catal. Lett*. 91 (2007) 141−147.
[36] S. Mukherjee, M.A. Vannice, *J. Catal*. 243 (2006) 108-130.
[37] P. Mäki-Arvela, L.-P. Tiainen, M. Lindblad, K. Demirkan, N. Kumar, R. Sjöholm, T. Ollonqvist, J. Väyrynen, T. Salmi, D.Yu. Murzin, *Appl. Catal. A: Gen*. 241 (2003) 271-288.
[38] P. Mäki-Arvela, N. Kumar, V. Nieminen, R. Sjöholm, T. Salmi, D.Yu. Murzin, *J. Catal.* 225 (2004) 155-169.
[39] G.K. Chuah, S.H. Liu, S. Jaenicke, L.J. Harrison, *J. Catal.* 200 (2001) 352-359.
[40] C. Milone, C. Gangemi, G. Neri, A. Pistone and S. Galvagno, *Appl. Catal. A: Gen.* 199 (2000) 239-244.
[41] (a) A.F. Trasarti, A.J. Marchi, C.R. Apesteguia, *J. Catal.* 224 (2004) 484-488.
(b) A.F. Trasarti, A.J. Marchi, C.R. Apesteguia, *J. Catal.* 247 (2007) 155-165.

Chapter 7

Selectivity control in hydrogenation reactions by nanoconfinement of polymetallic nanoparticles in mesoporous thin films

This Chapter is adapted from:
O. Muraza, E.V. Rebrov, A. Berenguer-Murcia, M.H.J.M. de Croon, J.C. Schouten, Selectivity control in hydrogenation reactions by nanoconfinement of polymetallic nanoparticles in mesoporous thin films, *Appl. Catal. A: Gen. in press* (2009), doi:10.1016/j.apcat1.2009.08.14.

Abstract

A one-pot sol-gel synthesis method has been developed for the incorporation of metal nanoparticles into mesoporous oxide thin films deposited on various plane substrates by spin-coating and on the inner surface of fused silica capillaries by dip-coating. The size, the metal loading and the stoichiometry of the metal nanoparticles could be precisely controlled by following this methodology. In the first step, polymer stabilized $Pt_{50}Sn_{50}$ and $Pt_{90}Sn_{10}$ nanoparticles were obtained by a solvent-reduction method. Then, the nanoparticles were added to a metal oxide precursor sol, which was destabilized by solvent evaporation. After calcination, the obtained materials were tested in the hydrogenation of citral in both batch and continuous modes. The highest selectivity of 30% to the unsaturated alcohols was obtained over supported $Pt_{90}Sn_{10}$ nanoparticles with a preferential formation of the cis-isomer (nerol) due to a unique confinement of the bimetallic nanoparticles in the mesoporous framework. The selectivity to the unsaturated alcohols was further improved to 56% over the $PtRu_5Sn$ nanoparticles supported by impregnation onto mesoporous silica films.

7.1 Introduction

The development of modern chemical technologies depends more and more on the availability of novel materials with well controlled structure and functionalities. Mesoporous thin films possess large surface areas and adjustable pore sizes, and their chemical composition can be varied in a wide range. These structured materials can be deposited onto the inner walls of microchannels in miniaturized reactors to prevent high pressure drop, to enhance catalyst accessibility, and to avoid internal diffusion limitations. Previous works have shown the controlled deposition of thin layers of mesoporous silica and titania films onto different substrates by evaporation induced self-assembly (EISA) with a possibility to control porosity, thickness, and chemical composition of the resulting films [1-5]. EISA has proved to be readily suited for the preparation of novel mesoporous materials with a variety of pore systems and dimensions, and the technique is now commonly applied in the preparation of silica and metal oxide nanostructured porous catalytic layers on various substrates. In the presence of colloidal nanoparticles or during deposition on substrates with microstructured features, preparative conditions should be adjusted for silica and titania systems [6] following the original synthetic protocols documented by Grosso et al. [7,8].

Ordered mesoporous oxide films are considered to be the potential host matrices to support metal or metal oxide nanoparticles for secondary growth of carbon nanowires [9], as well as for application in catalysis [10-13], bioelectrochemistry [14], electrochemistry [15], and sensors [16]. These highly ordered and precisely controlled structures are especially attractive for development of new generations of structured catalysts [17] for various gas-liquid-solid reactions.

Two synthetic approaches were applied in this study to incorporate nanoparticles into mesoporous silica and titania thin films. In the first approach, the mesoporous silica films were synthesized by sol-gel synthesis which was followed by adsorption of a $PtRu_5Sn$ cluster precursor [16,18] in the consecutive step. The second approach is based on a novel methodology [10,11] by which a uniform film, containing controlled amounts of polymetallic nanoparticles, can be obtained. This

elegant strategy is based on the condensation of metal oxide species by self-assembly in the presence of polymer stabilized $Pt_{50}Sn_{50}$ and $Pt_{90}Sn_{10}$ nanoparticles. This approach, however, has been hitherto successfully applied to relatively large nanoparticles with an average size of above 2 nm in order to prevent metal sedimentation inside the amorphous titania walls.

As opposed to stirred tank reactors, capillary microreactors with thin catalytic films nearly always operate in the kinetic mode instead of in the mass transport limited mode. Therefore, the screening of sufficiently active, in-house synthesized, catalytic films becomes an important step in the development of microreactor technology. The activity and selectivity of supported $Pt_{50}Sn_{50}$, $Pt_{90}Sn_{10}$, and $PtRu_5Sn$ nanoparticles, were studied in the hydrogenation of citral (3,7-dimethyl-2,6-octadienal) as a model reaction to demonstrate the feasibility of the applied approaches for the preparation of catalytic thin films. Citral is usually a mixture of cis- and trans-isomers and it can be hydrogenated towards the unsaturated aldehyde (CAL, citronellal) and unsaturated alcohols (UCOL, nerol and geraniol, cis- and trans-isomers, respectively). Subsequent hydrogenation of these products leads to citronellol (COL), and then to dimethyl octanol (DMOL), while isomerization of citronellal gives isopulegol (IP) (Scheme 7.1).

The probability to hydrogenate either the C=C or the C=O bond of the unsaturated aldehydes, which governs the final selectivity towards the production of the unsaturated alcohols, depends critically on the adsorption mode of the reactant molecule [19]. Higher electron density on the surface metal atoms decreases the binding energy of the C=C bond via an increase of the repulsive four-electron interaction and, on the other hand, favors the backbonding interaction with the π^*_{CO}-orbital and the hydrogenation of the C=O bond with respect to that of C=C. Therefore, electron-donating metals in bimetallic [19,20] or trimetallic [21] catalysts usually improve the selectivity towards the unsaturated alcohols.

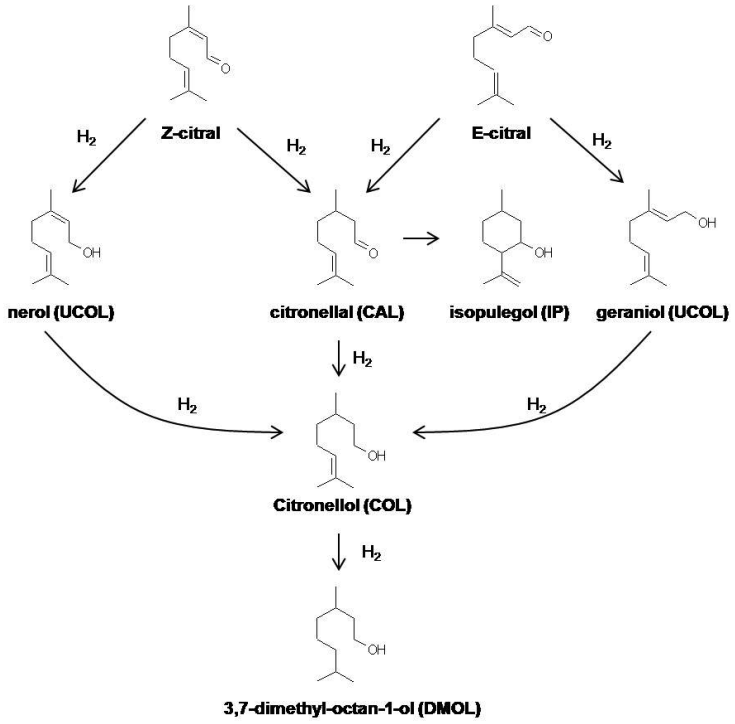

Scheme 7.1. Main products in hydrogenation of citral.

In this chapter, we address the influence of the capillary residence time, the reaction temperature, and the metal stoichiometry on the hydrogenation of citral and selectivity (including stereoselectivity) over a series of in-house made nanostructured catalytic films. The role of catalyst aging on the selectivity in the liquid phase hydrogenation of citral will be presented.

7.2 Experimental Section

To demonstrate the range of possible nanoparticles, supports and deposition methods, several combinations of them were investigated. Four types of nanoparticles (Pt, $Pt_{50}Sn_{50}$, $Pt_{90}Sn_{10}$, and $PtRu_5Sn$), three types of thin films (mesoporous silica templated with non-ionic surfactant, polymer templated mesoporous silica, and mesoporous titania), and two deposition methods (spin-coating and dip-coating) have been applied. In the first approach, metal

nanoparticles and thin films were prepared separately, which was followed by a cluster-derived nanoparticles deposition step (sections 7.2.1-7.2.3). In the second approach, one-pot synthesis of thin mesoporous oxide films containing controlled amounts of bimetallic nanoparticles was employed (section 7.2.4).

7.2.1 Nanoparticle synthesis

7.2.1.1 Synthesis of $PtRu_5Sn$ clusters

The mixed metal cluster nanoparticle precursor, $[PtRu_5C(CO)_{15}(\mu\text{-}Sn\text{-}Ph_2)]$, was synthesized using previously reported methodology [22] from the reaction of $[PtRu_5(CO)_{16}]$ with Ph_3SnH.

7.2.1.2 Synthesis of $Pt_{90}Sn_{10}$ and $Pt_{50}Sn_{50}$ nanoparticles

For solution 1, in a two-necked, round-bottom flask, 1.1 g of polyvinyl pyrrolidone (this amount corresponded to a metal-to-polymer ratio of 10:1) was added to 120 ml of anhydrous ethylene glycol. Different amounts of tin(II) acetate (depending on the final nanoparticle composition) were added to the mixture, and the system was stirred for 3 h at 353 K.

For solution 2, in a two-necked, round-bottom flask, different amounts of hydrogen hexachloroplatinate (depending on the final colloid composition) were dissolved in 50 ml of methanol under vigorous stirring for 2 h. The solution was dark orange in color. Solution 1 was cooled to 273 K with an ice bath, and solution 2 was poured into solution 1 under stirring to ensure homogenization. The pH of the resulting mixture was adjusted to approximately 9.5 by adding a 1 M NaOH solution. The resulting bright yellow solution was capped and heated at 373 K for 2 h under vigorous stirring. Then, the resulting colloidal solution was cooled to room temperature. The stability of the prepared bimetallic colloids is acknowledged by the fact that the colloidal glycol dispersions remained stable for more than 8 months after preparation, with no noticeable amount of aggregated colloid.

7.2.2 Synthesis of mesoporous thin films

To get a better adhesion, the surface roughness of the silicon substrates (1 cm x 1 cm) was increased to 500 nm by a micropowder jet treatment. A 50 nm TiO_2 layer was deposited by atomic layer deposition as descibed elsewhere [23]. Prior to the mesoporous thin film synthesis, the titania layer was made super hydrophilic by a UV irradiation (contact angle below 3^o, corresponding to a concentration of surface OH groups > 15 per nm^2) [24].

The synthesis solution was prepared following an earlier reported approach [2,25]. Briefly, the synthesis solution with a molar composition of 1.0 TEOS: 6.48 1-propanol: 2.64 2-butanol: 0.15 cetyl trimethyl ammonium bromide (CTAB): 0.007 aluminium tri-sec-butoxide (ATSB): 9.84 H_2O: 0.14 HCl (method A) and 1.0 TEOS : 0.007 Pluronic F127: 5.60 ethanol: 5.03 H_2O (method B) were used to prepare films with different pore diameter. After aging, a drop of the appropriate solution was deposited on the substrate. The substrate was spin-coated at 1500 rpm for 30 s at a relative humidity (RH) of 80%. The as-deposited films were dried and calcined at 573 K and a residual pressure of 5 mbar followed the approach developed by Glazneva et al. [24].

7.2.3 Catalyst deposition

7.2.3.1 Pt deposition

Fifty substrate plates coated on one side with the SiO_2 films (14 mg SiO_2) were impregnated with an aqueous solution of a H_2PtCl_6 precursor (40 mg $H_2PtCl_6.6H_2O$ / 8 ml water) for 24 h to obtain 1 wt.% metal loading. After impregnation, the substrates were left in a glove box at a RH of 80% for 4 h and then were exposed to a UV light for 24 h at a distance of 3 cm below the UV source (UV lamp: Hanovia 679A-36; 450 W; λ range, 220–1400 nm).

To prevent crack formation during thermal expansion and to obtain a uniform distribution of metal nanoparticles, a modified photocalcination procedure [25] was adopted for surfactant removal from the as-synthesized thin films containing Pt nanoparticles at ambient temperature [26-28].

7.2.3.2 Ru_5PtSn deposition

A substrate plate coated from one side with the mesoporous silica film was immersed in ether-dichloro methane solution (3 ml) containing 5 mg (2.8 μmol) of the $PtRu_5C(CO)_{15}(\mu\text{-}SnPh_2)$ molecular cluster at room temperature for 96 h. Then, the substrates were washed with diethyl ether and dried in vacuum and heated up to 573 K in vacuum to produce polymetallic nanoparticles.

7.2.4 Synthesis of thin films with embedded nanoparticles

Pluronic F127 (BASF) was dissolved in ethanol and a polyvinyl pyrrolidone stabilized ethanol suspension of colloidal $Pt_{50}Sn_{50}$ (or $Pt_{90}Sn_{10}$) nanoparticles was heated to 333 K for 5 min. The amount of Pt-Sn nanoparticles was chosen to obtain a 1 wt.% metal loading in mesoporous films. To this solution, water and HNO_3 (65% wt.) were added. The solution then was aged for 5 min. Titanium tetrabutoxide was added dropwise in the solution and then the solution was aged for 2 h. The final solution with a molar composition of 1 $Ti(OBu)_4$: 0.005 Pluronic F127 : 40 ethanol: 0.13 HNO_3 : 1.3 H_2O) was spin-coated in a similar way as described in section 3.2 (method C1). In case of film deposition on the inner wall of fused silica capillaries (250 μm i.d., 10 m length, Varian), dip-coating was applied instead of spin-coating (method C2). The deposition method is described elsewhere in detail [11]. Briefly, the titania sol was withdrawn from the capillary at a constant speed of 1 cm s^{-1}. The capillaries were left in a glove box for 24 h at a RH of 80% and then calcined at 573 K under a residual pressure of 10 mbar with a heating rate of 1 K/min to remove the surfactant.

7.2.5 Characterization

The morphology of the catalysts was determined by transmission electron microscopy (TEM). High resolution transmission electron microscopy (HR-TEM) images were recorded on a FEI Tecnai TF20 electron microscope operated at 200 kV. The collected powders were grinded and dispersed in ethanol. Then the suspensions were dropped gently to a holey amorphous carbon film on a Ni or Cu grid. The

particle size distribution (PSD) was obtained by measuring 100 particles from the TEM micrographs. The mean particle diameter was calculated by the following formula: $d_m = \frac{1}{100}\sum_{i=1}^{100} n_i d_i$, where n_i is the number of particles with diameter d_i. The dispersion of the metal nanoparticles, *%D*, was estimated from the mean particle diameter obtained from TEM by the formula: $\%D = \frac{C_1}{d(nm)}$, where C_1 is a constant, for supported platinum catalysts, C_1 is 108 [29]. XRD data were obtained on by a Rigaku Geigerflex Max/B diffractometer (40 kV, 40 mA) with Cu Kα radiation (using continuous scanning at 0.02° 2θ and a counting time of 0.5 s scan step).

For inductively coupled plasma (ICP) elemental analysis, the films were spin-coated on larger (2 cm x 2 cm) Si substrates following the same method as described in Section 7.2.2). Then the films were scratched, the scales were treated with aqua regia and the resulting solution was analyzed by inductively coupled plasma-atomic emission spectroscopy (ICP-AES).

7.2.6 Catalytic testing

7.2.6.1 Batch mode

The hydrogenation of citral was carried out in a 130 ml autoclave reactor (Büchi) at 343 K and 10 bar H_2 pressure with cyclohexane as solvent. Fifty substrate plates with mesoporous films were loaded in a rotating holder which was positioned in the reactor. The initial concentration of citral was varied depending on the Pt loading (see Table 7.1). Prior to the reaction, the films were reduced in a H_2 flow at 773 K for 10 min. After transfer into the reactor, the substrates with the thin films were reduced inside the reactor at 513 K. Liquid samples of 1 µl were selected for analysis after desired time intervals using a Rapid On-Line Sample Injector system (ROLSI ™) connected to a Varian 3800 gas chromatograph equipped with WCOT (30 m x 0.25 mm) and CP Sil 5CB DF columns and a FID detector.

Table 7.1. Synthesis parameters for supported catalysts

Catalyst (metal/support)	Synthesis method[a]	Acid	Solvent 1	Solvent 2	SDA[b]	Aging time (h)
Pt/SiO_2	A	HCl	1-propanol	2-butanol	CTAB	2
$PtRu_5Sn/SiO_2$	B	HCl	Ethanol	Dichloro methane	F127	4
$Pt_{50}Sn_{50}/TiO_2$	C1, C2	HNO_3	$Pt_{50}Sn_{50}$ suspension in ethanol		F127	2
$Pt_{90}Sn_{10}/TiO_2$	C2	HNO_3	$Pt_{90}Sn_{10}$ suspension in ethanol		F127	2

[a]See Section 7.2.2 for the description of methods A and B and Section 7.2.4 for the description of methods C1 and C2.
[b]SDA stands for structure directing agent

7.2.6.2 Continuous mode

In the catalytic activity tests, a mixture of citral in hexane was mixed in a T-mixer with a hydrogen flow. The internal diameters of the inlet and outlet tubes of the T-mixer were 250 μm. The gas was fed at an angle of 90° with respect to the liquid flow. The liquid flow was varied between 5 and 10 μL/min and the H_2 flow was kept constant at 1.0 mL/min (STP). The capillary and connecting tubes were placed in an oven maintained at the desired temperature. The product analysis was done off-line with the same Varian 3800 gas chromatograph.

There are two main operating flow regimes for gas-liquid flow in a microchannel: slug flow and annular flow. In the slug flow of a gas–liquid mixture, the gas slugs are separated from each other by liquid slugs, while in the annular flow the gas flows along the centre of the channel, and the liquid flows along the channel walls as a liquid film. In the absence of external mass transfer limitations, the choice of the flow regime determines the liquid hold-up in the reactor and does not influence the reaction kinetics. The range of applied gas and liquid flow velocities corresponds to the annular flow regime [30]. In this regime, the liquid hold-up depends on the thickness of the liquid film. The thickness of the liquid film can be calculated from the Lockhart-Martinelli-Chisholm correlation [31]. The correlation between the liquid two-phase friction multiplier ϕ_L^2 and the Martinelli parameter X^2, being the ratio of the single-phase liquid and gas pressure gradients, is given as $\phi_L^2 = 1 + C/X + 1/X^2$, where C is a parameter that depends on whether the liquid and gas flows are laminar or turbulent. For the laminar (liquid) - laminar (gas) case, considered in this study, C=5.

7.3 Results and discussion

7.3.1 Mesoporous titania films with embedded $Pt_{90}Sn_{10}$ and $Pt_{50}Sn_{50}$ nanoparticles

The synthesis protocol for the one-pot synthesis of mesoporous films by spin-coating on flat substrates or by dip-coating on the inner surface of fused silica capillaries involves four major steps [11] (Scheme 7.2): (1) Synthesis of colloidal

(metal or polymetallic) nanoparticles stabilized by a surfactant; (2) Preparation of an inorganic metal precursor sol containing colloidal nanoparticles and a structure directing agent; (3) Destabilization of the sol by solvent evaporation to yield a gel; and (4) Surfactant removal and *in situ* reduction of metal nanoparticles.

The individual steps of this method were presented and discussed in a series of publications [10,11] for the deposition of bimetallic nanoparticles into mesoporous silica and titania films. The properties of resulting catalytic films are summarized in Table 2.

In this section, we focus on the unique properties of the embedded nanoparticles in the liquid phase hydrogenation of citral. We address the influence of the nanoparticle composition, the catalyst configuration, and the reaction conditions on the hydrogenation of citral. The hydrogenations of the C=C and C=O bonds in citral transformation (Scheme 7.2) occur simultaneously depending on the accessibility of the actives sites, the size and the shape of the nanoparticles, and the citral to metal ratio. The latter was fixed during the experiments within a narrow range for proper activity comparison of the different catalytic systems. According to TEM data the mean particle size of nanoparticles was 2.4 ± 0.6 nm and 2.6 ± 0.7 nm for $Pt_{90}Sn_{10}$ and $Pt_{50}Sn_{50}$, respectively (Figure 7.1). In the following discussion we refer to the titania supported nanoparticles, however we omitted the support from the catalyst codes to avoid repetitions.

On metal nanoparticles with a size less than 4 nm, the presence of metal atoms with low coordination may allow unconstrained adsorption of both double bonds. In this case, the hydrogenation of the C=C bond is thermodynamically favored [20]. The $Pt_{50}Sn_{50}$ nanoparticles are substantially more selective than the $Pt_{90}Sn_{10}$ nanoparticles towards the formation of the saturated aldehyde (CAL) at 343 K in a capillary microreactor (Figure 7.2). The selectivity towards CAL reaches 72% over the $Pt_{50}Sn_{50}$ catalyst as compared with 13% over the $Pt_{90}Sn_{10}$ one. As the temperature decreases from 343 to 323 K, the amount of isopulegol (IP) formed increases from 8 to 38% over $Pt_{50}Sn_{50}$ and becomes equal to that of CAL while the sum of these two products remains rather constant (Figure 7.3 (a)).

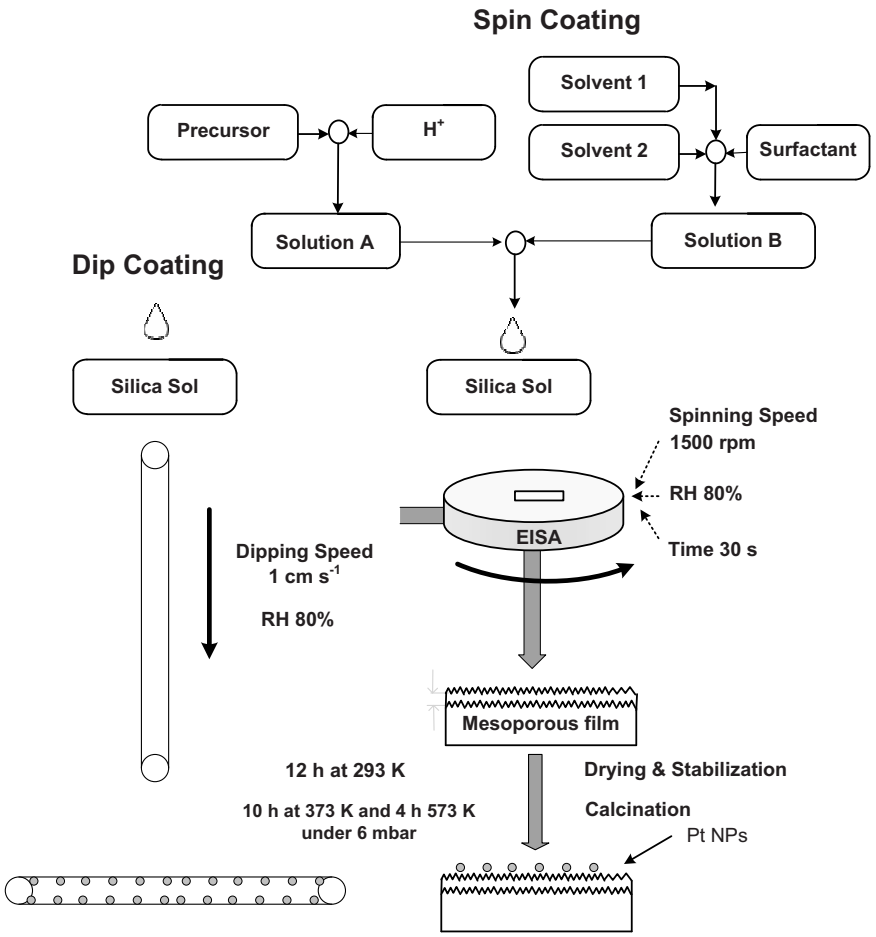

Scheme 7.2. Schematic representation for preparation of mesoporous catalytic films.

A similar trend was observed in a conventional batch reactor [32]. Such behavior can be explained if the production rates of CAL and UCOL in parallel reactions have similar activation energies while the activation energy of the subsequent isomerization of CAL to IP will be lower. The activation energies for the hydrogenation of citral of 75 and 53 kJ/mol were calculated from the Arrhenius plot at low conversions for $Pt_{50}Sn_{50}$ and $Pt_{90}Sn_{10}$, respectively (Figure 7.4).

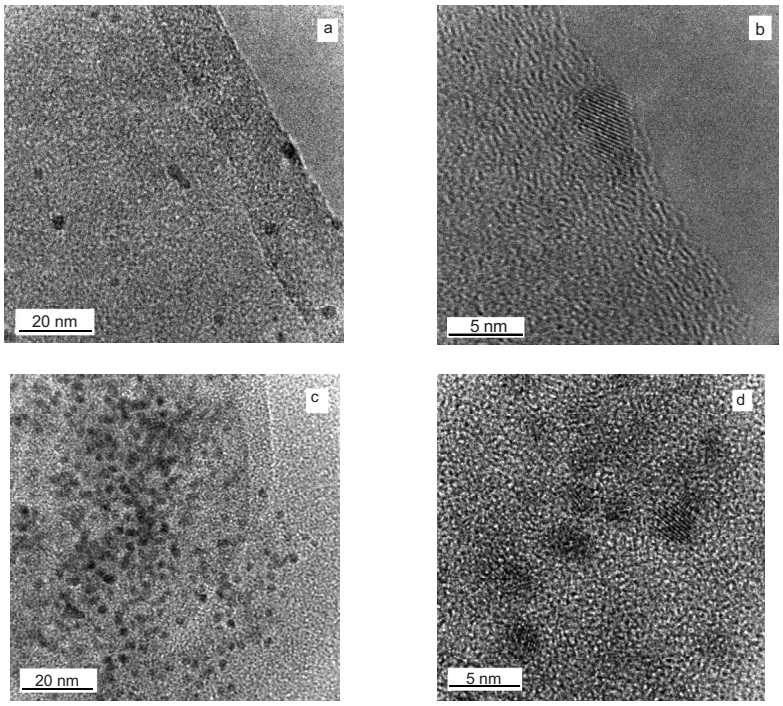

Figure 7.1.TEM images of (a and b) $Pt_{50}Sn_{50}$ and (c and d) $Pt_{90}Sn_{10}$ nanoparticles at different magnifications.

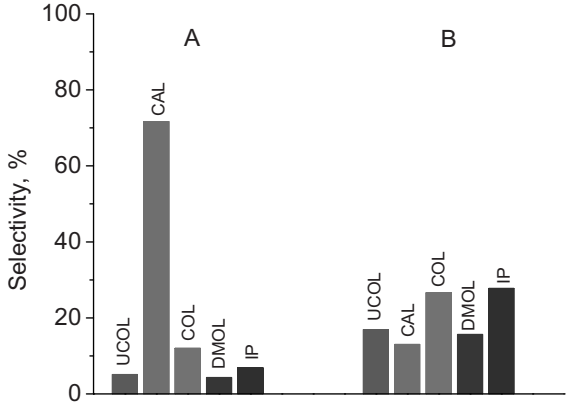

Figure 7.2. Selectivities to major reaction products on (a) $Pt_{50}Sn_{50}$ and (b) $Pt_{90}Sn_{10}$ at 343 K. Citral conversion: 25%. Liquid flow rate: 5 μl/min, H_2 flow rate: 1.0 ml/min (STP). Abbreviations: UCOL – unsaturated alcohols (geraniol and nerol), CAL – citronellal, COL – citronellol, DMOL – dimethyl octanol, IP – isopulegol.

A different selectivity pattern was observed at 343 K over the $Pt_{90}Sn_{10}/TiO_2$ film. IP and citronellol (COL), with the latter being an intermediate in the subsequent hydrogenation of both CAL and UCOL, are the main reaction products with a selectivity of 28% at 343 K (Figure 7.3 (b)). The yield of the fully saturated product (DMOL) is four times higher as compared with the $Pt_{50}Sn_{50}$ catalyst. As the temperature decreases to 323 K, the selectivity to IP increases from 28 to 50% while the sum of the IP and COL selectivities remains constant and equals 52-53%. This allows to conclude that COL is formed over the $Pt_{90}Sn_{10}$ catalyst preferably via hydrogenation of CAL rather than UCOL. The temperature dependence of the selectivities towards the main reaction products resembles that observed over the $Pt_{90}Sn_{10}$ catalyst with the exception of a much higher amount of CAL becoming hydrogenated to COL and even further to DMOL as well as a larger amount of CAL being converted to IP. In other words, subsequent hydrogenation and isomerization of the partially hydrogenated intermediates is more pronounced over the catalyst with the higher Pt content.

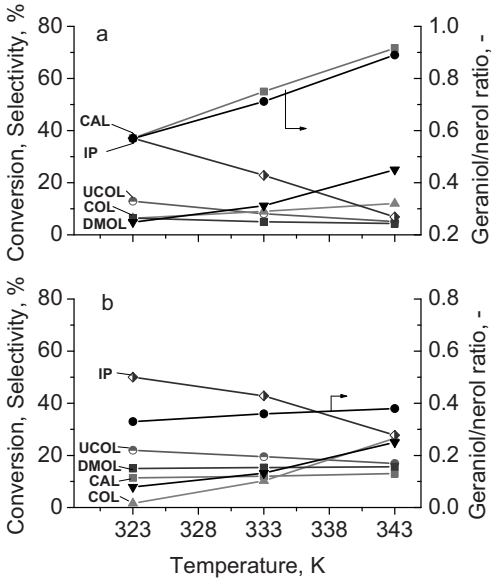

Figure 7.3. Citral conversion (▼) and selectivities to major reaction products over (a) $Pt_{50}Sn_{50}/TiO_2$ and (b) $Pt_{90}Sn_{10}/TiO_2$ as a function of temperature. Liquid flow rate: 5 µl/min, H_2 flow rate: 1.0 ml/min (STP). Symbols represent experimental data, lines are the guide for the eye. Abbreviations are the same as those in Figure 7.2.

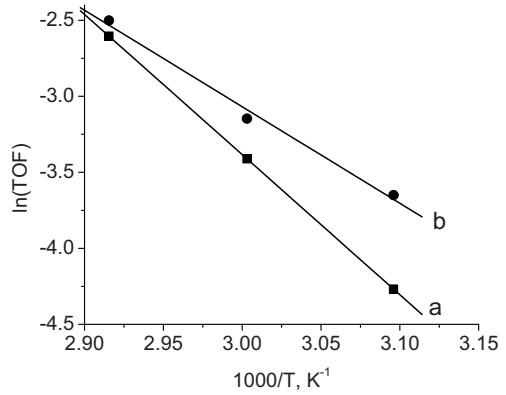

Figure 7.4. Arrhenius plot on (a) $Pt_{50}Sn_{50}/TiO_2$ and (b) $Pt_{90}Sn_{10}/TiO_2$. The conditions are the same as those in Figure 7.3.

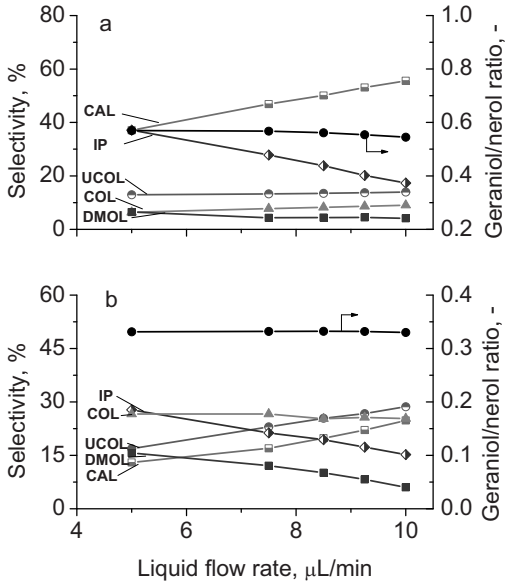

Figure 7.5. Citral conversion (▼) and selectivity to major reaction products over (a) $Pt_{50}Sn_{50}/TiO_2$ and (b) $Pt_{90}Sn_{10}/TiO_2$ as a function of the liquid flow rate. Temperature: 343 K. H_2 flow rate: 1.0 ml/min (STP). Abbreviations are the same as those in Figure 7.2.

Over the $Pt_{50}Sn_{50}$ catalyst, the selectivity towards IP decreases from 37 to 17% while the selectivity to CAL increases from 37 to 55% with an increase of the liquid flow rate from 5 to 10 μL/min, which corresponds to a decrease of the liquid residence time from 23 to 13.5 min (Figure 7.5 (a)). The selectivities to other products

remain relatively unchanged. From the discussion above it follows that the subsequent hydrogenation of CAL proceeds slowly, therefore this product dominates at the shortest liquid residence time of 13.5 min. As the residence time increases to 23 min (liquid flow rate of 5 μL/min), substantial amounts of CAL are converted to IP. Constant selectivities towards UCOL and COL clearly point out that COL is mainly formed via the hydrogenation of UCOL over the $Pt_{50}Sn_{50}$ nanoparticles. The dependence of the selectivity to IP and CAL on the liquid flow rate has a similar trend over the $Pt_{90}Sn_{10}$ nanoparticles (Figure 7.5(b)). The isomerization of CAL to IP proceeds to a larger extend at a liquid residence time of 23 min, therefore the selectivity to CAL increases by 11.5 %, while the selectivity to IP decreases by 13% as the liquid flow rate increases from 5 to 10 μl/min. A difference of 1.5% in selectivity is due to the fact that a part of CAL is hydrogenated to COL and further to DMOL. However, the selectivity to UCOL increases by 11.7% while that to the fully hydrogenated product (DMOL) decreases by 9.6%. This observation allows to conclude that a part of COL, and also of DMOL, is produced via the hydrogenation of UCOL over the $Pt_{90}Sn_{10}$ catalyst.

Apart from the ratio between two metals, it is well known that the distribution of the second metal in a bimetallic nanoparticle is also responsible for the selectivity pattern [33]. Vilella et al. [33] studied addition of Sn to Pt/SiO_2 by controlled surface reactions which allowed them to modify the selectivity to different hydrogenation products. For a low surface concentration of the second metal in a Pt–M bimetallic nanoparticle, the catalysts were selective for the hydrogenation of the - C = C - bonds, but the higher Sn to Pt ratio catalysts were selective for the hydrogenation of the carbonyl group. Vilella et al. [34] observed a similar trend in the selectivity pattern in citral hydrogenation over a series of bimetallic PtSn catalysts supported on an activated carbon felt (ACF). The Pt loading was fixed at 5 wt.% while the Sn loading was varied corresponding to nominal compositions of Pt_6Sn_2, Pt_6Sn_3, and Pt_6Sn_6. The selectivity to UCOL at a citral conversion of 70% decreased from 46.3% over Pt_6Sn_2 to 42.5% over Pt_6Sn_3 and then increased, reaching values higher than 70% for the catalyst with a Sn/Pt ratio of 1. Besides, the formation of CAL was also affected by

the tin addition. The selectivity towards CAL increased from 13.4% over Pt_6Sn_2 to 16.4% over Pt_6Sn_3 and then decreased to 6.7% over Pt_6Sn_6. The authors concluded that different degree of dilution of Pt atoms by Sn would either inhibit or promote the hydrogenation of the - C = C - bonds and the adsorption of the unsaturated alcohols. They observed an enrichment of the surface of bimetallic particles in Sn at low tin content, however the degree of this enrichment was much lower than the one that was found on a PtSn/C catalyst with a Pt loading of 0.3 wt.%. A conclusion has been made that the total metallic loading, the promoter tin loading and the nature of the support (carbon vs. ACF) can affect the structure of the metallic phase and the selectivity towards UCOL. It should be mentioned that several other authors have reported an important influence of the support on the structure of the metallic phase in the hydrogenation of α,β-unsaturated aldehydes [35] and [36].

This difference in the selectivity pattern between $Pt_{50}Sn_{50}$ and $Pt_{90}Sn_{10}$ might be primarily attributed to the different fractions of exposed metal surfaces with varying metal stoichiometry, i.e. at Pt-rich colloids there exist a larger polycrystalline Pt domain while individual Pt atoms prevail in the $Pt_{50}Sn_{50}$ nanoparticles. The current results show that the reaction conditions can also alter the activity and the selectivity, but the intrinsic properties of the catalyst, viz. the nanoparticle composition, are still the dominating features, regardless of which reaction parameter is varied.

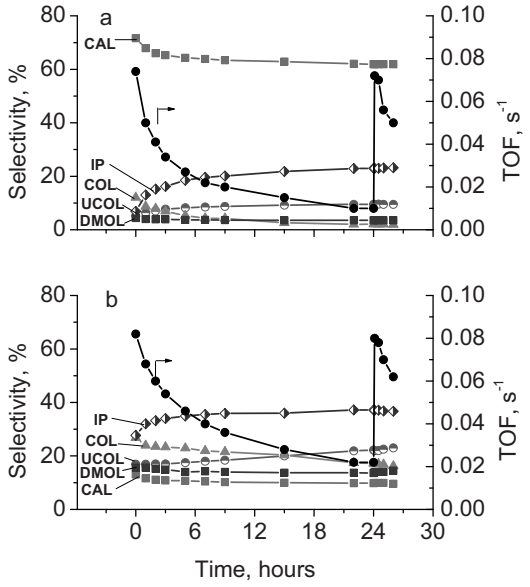

Figure 7.6. Reaction rate and selectivity to major reaction products as a function of time-on-stream for (a) $Pt_{50}Sn_{50}/TiO_2$ and (b) $Pt_{90}Sn_{10}/TiO_2$. Temperature: 343 K. Liquid flow rate: 5 μl/min, H_2 flow rate: 1.0 ml/min (STP).

The capillary microreactor with the $Pt_{50}Sn_{50}/TiO_2$ catalyst deactivated faster than the $Pt_{50}Sn_{50}/TiO_2$ one (Figure 7.6). The activity of both catalysts in the hydrogenation of citral decreased significantly during the course of the reaction for all reaction conditions studied. The selectivity towards UCOL increased for all reaction conditions during the course of the reaction and reached a steady-state value. The initial activity of the deactivated films could be completely restored by purging the capillary microreactor with an air/hexane flow at 353 K. After regeneration with air, the selectivities towards the major products were not identical with the initial values, but close to those just before regeneration (Figure 7.6). For both catalysts it was found that the selectivity towards the unsaturated alcohols (UCOL) monotonously increased with time-on-stream. This suggests that higher selectivities may be obtained at a defined number of turnovers with both catalysts. However, increasing the selectivity by a longer exposure of the catalyst to the reaction mixture is limited to some extend as the $Pt_{90}Sn_{10}$ and $Pt_{50}Sn_{50}/TiO_2$ films decrease their initial

activity by 75% for the hydrogenation of all types of double bonds after 8 and 24 hours, respectively.

As the catalysts regained their initial activities after regeneration, it appears that decarbonylation and the irreversible adsorption of CO on the metal surface is the main reason for the loss in activity. For gas phase reactions, the initial activity of the deactivated catalysts can be restored by removing CO via evacuation at 573 K, while for the capillary microreactors this is not practical, but the activity of a deactivated catalyst could be fully restored by replacing the hydrogen flow with air. During that procedure, the adsorbed CO is oxidized to CO_2 which has a significantly lower adsorption constant than CO on Pt [37]. It desorbs and the properties of the films are restored without influencing the metal dispersion. Our results suggest that CO blocks the active sites, leading to a decrease in the activity of the catalyst, but this is of minor importance for the selectivity. After the oxidation pretreatment, the initial selectivity of 30% was not fully recovered (Figure 7.6 (b)). The selectivity was close (about 4% lower) to that obtained just before the oxidation treatment. It appears that the metal sites at the steps, corners and kinks do not regain their original properties [38] by the oxidative treatment under mild conditions.

7.3.2 Stereoselectivity in hydrogenation of citral over bimetallic supported catalysts

Citral used in this study was a mixture of cis- and trans-isomers with a molar ratio of the cis (*Z*-) and trans (*E*-)isomers of 1.08. The difference in selectivity towards formation of the cis- and trans-isomers of UCOL was studied for both the $Pt_{90}Sn_{10}/TiO_2$ and the $Pt_{50}Sn_{50}/TiO_2$ catalysts and the ratio of geraniol to nerol (trans- to cis-isomer) is given in Figures 7.3 and 7.5 as a function of the temperature and the liquid flow rate, respectively. This ratio is about 0.55 and 0.33 over the $Pt_{50}Sn_{50}$ and $Pt_{90}Sn_{10}/TiO_2$ films, respectively, for all reaction conditions at 343 K. This means that the yield of the trans-isomer (geraniol) was much lower on both supported catalysts. As both catalysts have similar particle sizes (as shown in Figure 7.1) and were deposited on the same support, it is obvious that the difference in the selectivity is a

consequence of the metal ratio (nanoparticle formulation) and the nanoconfinement of the nanoparticles within the mesoporous structure.

An excess of the cis-isomer (nerol) in the liquid phase hydrogenation of citral can be explained by a higher reactivity of cis-citral (neral) as compared to that of trans-citral (geranial). Such selectivity pattern is rather unusual in the hydrogenation of unsaturated aldehydes. It is difficult to rationalize the higher reactivity of the cis-isomer compared to the trans-isomer over titania supported bimetallic nanoparticles. The trans-to-cis isomerization is thermodynamically possible [39] and it has been reported in the literature [38-41]. It is well known that trans-to-cis isomerization reactions are catalyzed by weak or medium acid sites and their rates are independent from the presence of metal particles [38]. However, this isomerization reaction can be excluded at 323 K. Indeed the rates of disappearance of the trans- and cis-isomers of citral are equal to the respective rates of formation of the trans- and cis-isomers of UCOL (geraniol and nerol, respectively), thus indicating that isomerization of trans- to cis-isomer is not observed under reaction conditions. However, as the temperature increases (from 323 to 343 K), larger amounts of the trans-isomer were produced on both catalysts. It appears that the hydrogenation of the trans-isomer increases faster at higher temperature as compared with that of the cis-isomer.

It should be mentioned that decreasing the pore size from 3.0 to 2.2 nm as well as the bimetallic $Pt_{50}Sn_{50}$ particle size from 2.4 to 1.8 nm, considerably improved the selectivity to UCOL (Table 7.2). At the same time geraniol was formed in much higher amounts as compared with nerol. We assume that such dramatic change in selectivity pattern can be due to geometrical constrictions in the smaller mesopores. The difference between the pore diameter and the nanoparticle size of 0.4 nm can substantially decrease the amount of active sizes available for citral adsorption via the C=C double bond (Table 7.3).

Bimetallic catalysts seem to have a promising prospect to change the selectivity (including stereo selectivity) in the hydrogenation of citral by varying the metal stoichiometry in the nanoparticles. In this way, trimetallic supported catalysts possess even larger possibilities for fine tuning of their electronic properties and

changing the mode of adsorption of organic molecules. Below we focus on one example of application of trimetallic nanoparticles deposited onto a mesoporous silica support to improve the yield of unsaturated aldehydes in citral hydrogenation.

7.3.3 Improvement selectivity to unsaturated alcohols on trimetallic supported catalysts

Trimetallic $PtRu_5Sn$ clusters were embedded into mesoporous silica films by impregnation. The resulting nanoparticles were attached to the support via two Ru-Si-Si bonds [42]. The $PtRu_5Sn$ cluster was chosen as a model system following the previous results obtained in the hydrogenation of dimethyl terephthalate (DMT) [18]. The conversion of DMT over silica supported $PtRu_5Sn$ was much higher as compared with that observed over silica supported Ru_5Pt and Ru_6Sn nanostructured catalysts. It should be pointed out that the size of the $PtRu_5Sn$ clusters was much smaller as compared to that of the channel wall. If one-pot deposition method is applied, a substantial number of clusters would be located entirely inside the silica walls rather than exposed to the reactants in the mesopores. Therefore impregnation was used for the deposition of $PtRu_5Sn$ clusters. The silica film was chosen as a support for this study to exclude a possible strong metal support interaction effect observed in case of a titania support. However, the silica support is less stable as compared with the titania support in polar organic solvents [25], therefore the duration of these tests was limited to seven hours.

The initial hydrogenation activity and selectivity towards the main reaction products are listed in Table 7.2 and shown in Figure 7.7 in comparison with monometallic and bimetallic catalysts. It should be noted that the sum of the selectivities is less than 100% as several other by-products were formed in minor quantities. After a reaction time of 120 min, the $PtRu5Sn/SiO_2$ film showed the highest turnover frequency (TOF). The hydrogenation of the carbonyl group was dominant over this catalyst, producing UCOL with a selectivity of 56% at a 50% citral conversion. The high activity is related to the precise control of the nanoparticles size of 1.8 nm anchored on the inner surface of the silica mesopores [18]. The long order

structure of the films was still intact after completion of the reaction as shown in Figure 7.8. The cis-isomer (nerol) was formed in slightly larger amounts as compared with geraniol, corresponding to the geraniol to nerol molar ratio in the range of 0.88 to 0.93 (Table 7.2) over $PtRu_5Sn/SiO_2$, which is in agreement with previously reported data [32].

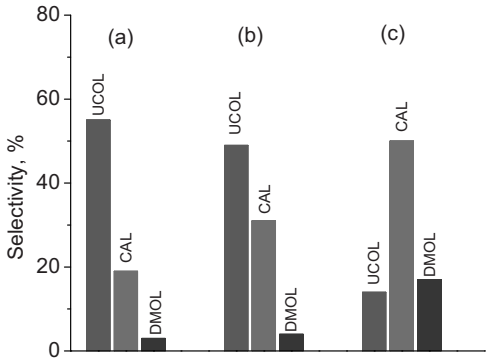

Figure 7.7. Selectivity towards unsaturated alcohols, citronellal and dimethyl octanol at 50% conversion over (a) $Pt_{50}Sn_{50}/TiO_2$, (b) $PtRu_5Sn/SiO_2$, and (c) Pt/SiO_2, at 343 K under 10 bar hydrogen in cyclohexane.

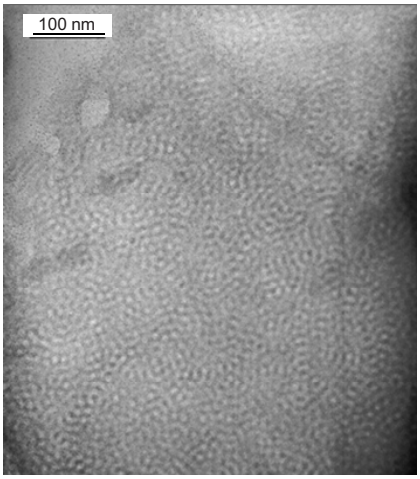

Figure 7.8. TEM images of spent $PtRu_5Sn/SiO_2$ film.

Table 7.2. Properties of mono- and bi-metallic catalytic systems.

Catalyst	Synthesis method[a]	Porosity[b]	Mesopore volume[b] (cm^3/g)	Pore size[b] (nm)	Particle size (nm)
Pt/SiO_2	A + I	n/d	n/d	> 10	2-10
$Pt_{50}Sn_{50}/TiO_2$	C1	n/d	n/d	2.2	1.8
$Pt_{50}Sn_{50}/TiO_2$	C2	0.28	0.22	3.0	2.6
$Pt_{90}Sn_{10}/TiO_2$	C1	0.30	0.25	3.0	2.4
$PtRu_5Sn/SiO_2$	B + 1	n/d	n/d	6.7	1.8

Abbreviations:

[a] See Section 7.2.2 for the description of methods A and B and Section 7.2.4 for the description of methods C1 and C2. Letter "I" stands for impregnation

[b] Ethanol adsorption data

Table 7.3. Comparison of initial TOF and selectivities towards major products over different catalytic systems in citral hydrogenation.

Catalyst	Synthesis method[a]	TOF after 120 min (s^{-1})	Selectivity at 25% conversion (%)				at 50% conversion			
			G/N	S_{UCOL}	S_{CAL}	S_{DMOL}	G/N	S_{UCOL}	S_{CAL}	S_{DMOL}
Pt/SiO_2	A + I	0.025	n/d	13	54	0	n/d	17	50	0
$Pt_{50}Sn_{50}/TiO_2$	C2	0.041	0.90	5	72	6	n/d	n/d	n/d	n/d
$Pt_{90}Sn_{10}/TiO_2$	C2	0.060	0.39	17	13	16	n/d	n/d	n/d	n/d
$Pt_{50}Sn_{50}/TiO_2$	C1	0.184	1.57	53	28	6	1.64	48	31	4
$PtRu_5Sn/SiO_2$	B + I	0.190	0.93	45	29	0	0.88	56	19	1

Abbreviations: I – impregnation, G/N is the geraniol to nerol molar ratio, UCOL – unsaturated alcohols, CAL - citronellal, COL - citronellol, and DMOL - 3,7-dimethyl-octanol. n/d – not determined.

[a] See Section 7.2.2 for the description of methods A and B and Section 7.2.4 for the description of methods C1 and C2.

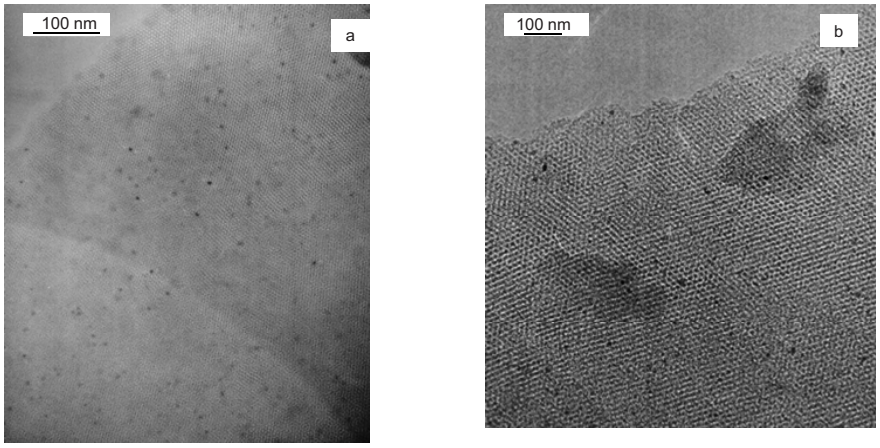

Figure 7.9. TEM images of (a) fresh Pt/SiO_2 and (b) spent Pt/SiO_2 films.

The activity and selectivity of the bi- and trimetallic catalysts was compared with that of the Pt/SiO_2 film obtained by photocalcination. The Pt nanoparticles have a narrow particle size distribution with an average size of 1.9 and 1.8 nm before and after catalytic tests, respectively (Figure 7.9), which justifies using photocalcination [43] as a promising method for fabrication of catalytic thin films containing embedded nanoparticles. However, monometallic Pt nanoparticles demonstrate a lower reaction rate after a reaction time of 120 min as compared to bi- and tri-metallic ones. The selectivity to UCOL was increased from 13 to 17% in the course of the reaction and it was quite similar to that observed over the bimetallic nanoparticles embedded into mesoporous supports with a larger pore diameter. As discussed above, a similar increase in the selectivity towards UCOL over the bimetallic catalysts was related to the fact that the less selective sites deactivate faster.

7.4 Conclusion

Two modes of functionalized nanoparticle delivery onto film films for application in catalytic microstructured reactors were demonstrated: post-synthesis impregnation of the support and one-pot synthesis. An addition of the second and third element to the nanoparticles is responsible for dramatic changes in the activity

and selectivity pattern of supported thin films in hydrogenation of citral. Reaction conditions can also alter the activity and the selectivity, but the intrinsic properties of the catalyst, viz. the nanoparticle composition, are still the dominating features, regardless of which reaction parameter was varied. The selectivity towards the target product can be changed in a wide range by varying the composition, the metal ratio, and/or the pore size of the support. The methods proposed in this study allow independent control of each of these parameters.

References

[1] G. Cortial, M. Siutkowski, F. Goettmann, A. Moores, C. Boissiere, D. Grosso, P. Le Floch, C. Sanchez, *Small* 2 (2006**)** 1042-1045.

[2] O. Muraza, E.V. Rebrov, T. Khimyak, B.F.G. Johnson, P.J. Kooyman, U. Lafont, P.A. Albouy, M.H.J.M. de Croon, J.C. Schouten, *Stud. Surf. Sci. Catal.* 162 *(*2006**)** 167-174.

[3] P. C. Angelomé, M. C. Fuertes, G. J. A. A. Soler-Illia, *Adv. Mater.* 18 (2006) 2397-2402.

[4] M. C. Fuertes, F. J. López-Alcaraz, M. C. Marchi, H. E. Troiani, V. Luca, H. Míguez, G. J. A. A. Soler-Illia, *Adv. Funct. Mater.* 17 (2007) 1247-1254.

[5] M.C. Fuertes, S. Colodrero, G. Lozano, A. R. Gonzalez-Elipe, D. Grosso, C. Boissière, C. Sanchez, G. J. A. A. Soler-Illia, H. Miguez, *J. Phys. Chem. C* 112 (2008) 3157-3163.

[6] O. Muraza, E.V. Rebrov, T. Khimyak, B.F.G. Johnson, P.J. Kooyman, U. Lafont, M.H.J.M. de Croon, J.C. Schouten, *Chem. Eng. J*. 135 (2008**)** S99-S103.

[7] D. Grosso, F. Cagnol, G.J. Soler-Illia, E.L. Crepaldi, H. Amenitsch, A. Brunet-Bruneau, A. Bourgeois, C. Sanchez, *Adv. Funct. Mater.* 135 (2004) 309-322.

[8] D. Grosso, A.R. Balkenende, P.A. Albouy, A. Ayral, H. Amenitsch, F. Babonneau, *Chem. Mater*. 13 (2001**)** 1848-1856.

[9] D. Barreca, W.J. Blau, G.M. Croke, F.A. Deeney, F.C. Dillon, J.D. Holmes, C. Kufazvinei, M.A. Morris, T.R. Spalding, E. Tondello, *Micropor. Mesopor. Mater.* 103 (2007) 142-149.

[10] E.V. Rebrov, A. Berenguer-Murcia, B.F.G. Johnson, J.C. Schouten, *Catal. Today* 138 (2008) 210-215.

[11] E.V. Rebrov, A. Berenguer-Murcia, H.E. Skelton, B.F.G. Johnson, A.E.H. Wheatley, J.C. Schouten, *Lab Chip* 9 (2009) 503-506.

[12] S.B. Zhang, J. K. Wang, H. T. Liu, X. L. Wang, *Catal. Commun.* 9 (2008) 995-1000.

[13] Y. Zhang, A. H. Yuwono, J. Li, J. Wang, *Micropor. Mesopor. Mater.* 110 (2008) 242-249.

[14] X. Xu, B.Z. Tian, J.L. Kong, S. Zhang, B.H. Liu, D.Y. Zhao, *Adv. Mater*. 15 (2003) 1932-1936.

[15] D.F. Rohlfing, J. Rathouský, Y. Rohlfing, O. Bartels, M. Wark, *Langmuir* 21 (2005) 11320-11329.

[16] G. Walters, I.P. Parkin, *J. Mater. Chem*. 19 (2009) 574-590.

[17] F. Goettmann, C. Sanchez, *J. Mater. Chem*. 17 (2007) 24-30.

[18] A.B. Hungria, R. Raja, R.D. Adams, B. Captain, J.M. Thomas, P.A. Midgley, V. Golovko, B.F.G. Johnson, *Angew. Chem. Int. Ed*. 45 (2006) 4782-4785.

[19] F. Delbecq, P. Sautet, *J. Catal.* 152 (1995) 217-236.

[20] G. Neri, C. Milone, S. Galvagno, A.P.J. Pijpers, J. Schwank, *Appl. Catal. A* 227 (2002) 105-115.
[21] G. Cárdenas, R. Oliva, P. Reyes, B.L. Rivas, *J. Mol. Catal. A* 191 (2003) 75-86.
[22] Hungria, R.D. Adams, B. Captain, W. Fu, *J. Organomet. Chem*. 671 (2003) 158-165.
[23] M.J.M. Mies, E.V. Rebrov, J.C. Jansen, M.H.J.M. de Croon, J.C. Schouten, *J. Catal. 247* (2007) 328-338.
[24] T.S. Glazneva, E.V. Rebrov, J.C. Schouten, E.A. Paukshtis, Z.R. Ismagilov, *Thin Solid Films 515* (2007) 6391-6394.
[25] O. Muraza, E.V. Rebrov, M.H.J.M. de Croon, J.C. Schouten, *Micropor. Mesopor. Mater.* 124 (2009) 20-29
[26] Y. Kumai, H. Tsukada, Y. Akimoto, N. Sugimoto, Y. Seno, A. Fukuoka, M. Ichikawa, S. Inagaki, *Adv. Mater*. 18 (2006) 760-762.
[27] A. Fukuoka, H. Araki, Y. Sakamoto, N. Sugimoto, H. Tsukada, Y. Kumai, Y. Akimoto, M. Ichikawa, *Nano Lett.* 2 (2002**)** 793-795.
[28] K.J. Chao, Y.P. Chang, Y.C. Chen, A.S. Lo, T.H. Phan *J. Phys. Chem. B* 110 (2006**)** 1638-1646.
[29] C.H. Bartholomew, R.J. Farrauto, Fundamentals of Industrial Catalytic Processes, 2nd edition, John Wiley, 2006.
[30] V. Haverkamp, V.Hessel, H.Löwe, G. Menges, M.J.F.Warnier, E.V. Rebrov, M.H.J.M. de Croon, J.C. Schouten M.A. Liauw *Chem. Eng. Technol.* 29 (2006) 1015-1026.
[31] D. J. Chisholm, *Heat Mass Transfer.* 10 (1967) 1767-1778.
[32] P. Mäki-Arvela, J. Hájek, T. Salmi, D.Yu. Murzin, *Appl. Catal. A: Gen*. 292 (2005) 1-49.
[33] I.M.J. Vilella, I. Borbáth, J.L. Margitfalvi, K. Lázár, S.R. de Miguel, O.A. Scelza, *Appl. Catal. A* 326 (2007) 37–47.
[34] I.M.J. Vilella, S.R. de Miguel, O.A. Scelza, *Lat. Am. Appl. Res.* 35 (2005) 51-57.
[35] N. Homs, J. Llorca, P.R. de la Piscina, F. Rodríguez-Reinoso, A. Sepúlveda Escribano, J. Silvestre-Albero, *Phys. Chem. Chem. Phys*. 3 (2001) 1782-1788.
[36] R. Malathi, R.P. Visnawanath, *Appl. Catal. A* 208 (2001) 323–327.
[37] B. Beden, A. Bewick, M. Razaq, J. Weber, *J. Electroanal. Chem.* 139 (1982) 203-206.
[38] M. Englisch, V.S. Ranade, J.A. Lercher. *Appl. Catal. A: Gen*. 163 (1997) 111-122.
[39] R.C. Reid, J.M. Prausnitz, T.K. Sherwood, The Properties of Gases and Liquids, McGraw-Hill, New York, 1977.
[40] M.A. Chesters, C. De La Cruz, P. Gardner, E.M. McCash, P. Pudney, G. Shahid, N. Sheppard. *J. Chem. Soc., Faraday Trans*. 86 (1990) 2757-2763.
[41] C. Yoon, M.X. Yang, G.A. Somorjai. *J. Catal.* 176 (1998) 35-41.
[42] A.M. Dattelbaum, M.L. Amweg, J.D. Ruiz, L.E. Ecke, A.P. Shreve, A.N. Parikh, *J. Phys. Chem. B*, 109 (2005**)** 14551-14556.

Chapter 8

Conclusions and Outlook

8.1 Conclusions

Microstructured reactors have found strong potential to replace conventional three phase slurry reactors for production of fine chemicals where the massive production volume is not the barrier to accomplish industrial scale microplants. The application of microstructured catalytic reactors for gas-liquid-solid multiphase reactions requires new techniques for incorporation of highly active catalytic thin films onto their surfaces. This catalyst incorporation is the critical variable in microstructured reactor prominence. These catalytic thin films with an open porosity up to 50% prevent high pressure drop, enhance catalyst accessibility and eliminate mass transfer limitations.

In this thesis, ordered mesoporous silica and titania films with a thickness of 100 to 400 nm were developed via an evaporation induced self assembly method on various substrates (glass, silicon, titanium). Ordered micro- and mesoporous silica films (OMSFs) have shown potential for various applications, which requires that the material remains stable for the life-time of the intended application and resists non-specific adsorption of solvents. In **Chapter 2,** The thermal and hydrothermal stability of micro porous silica thin films templated by ionic surfactant and deposited on Si substrates, was improved by pH adjustment of the synthesis mixture to 2.0 during the hydrolysis of the silica precursor. It was further improved by incorporation of Al at an Al/Si ratio in the range of 0.005 to 0.007. At higher Al contents the presence of large amounts of Al deep within the pore walls cancelled out part of the stabilizing

effects of Al located on or nearer to the surface. After exposure to non-polar solvents, the long-order structure of the Al-containing films remained unchanged after 48 h. The samples with an Al/Si ratio of 0.007 showed the smallest d-spacing shift after exposure to non polar solvents. This demonstrates that aluminium incorporation enhanced the hydrothermal stability in organic solvents. A new calcination protocol has been proposed which allows complete surfactant removal at mild conditions. The Pd-impregnated films with Al/Si=0.007 were stable in the hydrogenation of phenyl acetylene performed at 303 K and 10 bar H_2 with hexane as solvent. No catalyst deactivation was observed in two subsequent hydrogenation runs.

A complete and elaborated description of the morphology of mesoporous oxide film as a promising catalyst support in microstructured reactors has been obtained by combining X-Ray diffraction, small angle X-Ray scattering (2D-SAXS) analyses, and ellipsometric porosimetry (EP) experiments. The EP analysis has been adapted to obtain rapid technique which operates at close to ambient pressure and temperature. The principle of EP is based on the evaluation of the optical characteristics of a porous oxide film during vapour adsorption in the pores. An improved Derjaguin–Broekhoff–de Boer model enables determination of the structural parameters of a films porous network: the pore diameters, porous volume, and surface area [1]. EP is considered to be more informative than conventional adsorption porosimetry, and is much simpler than other porosimetry techniques, for example, small angle neutron scattering (SANS) or positron annihilation techniques because, in addition to structural characteristics, the heat of adsorption of volatile adsorbates on different surfaces can also be determined by measuring of the optical characteristics at different temperatures.

Mesoporous silica thin films templated by non-ionic triblock copolymer with a thickness of 0.36-1.40 μm have been prepared by the evaporation induced self-assembly assisted sol-gel route on the microchannels etched in a Pyrex® 7740 borosilicate glass substrate. In **Chapter 3**, it was reported that the width to depth ratio of the microchannels between 2 (semi-circular) and 3 (semi-oval) was found to provide the minimum non-uniformity of ca. 2 in the film thickness between the side

and bottom walls of the microchannel. The mixed-metal precursor clusters of $Ru_{10}Pt_2$ have been inserted into the mesoporous films to obtain well-dispersed, isolated and anchored bimetallic nanoparticles of 3 to 4 nm in diameter. The intact long-order porosity with a pore size of 8.2 nm after the encapsulation of the bimetallic clusters was observed.

The triblock-copolymer templated mesostructured silica films with a narrow pore size distribution via an evaporation-induced self-assembly method have been synthesized in a wide range of pore sizes (2 to 8 nm). The development of adsorption methods to deposit bimetallic (Pt-Sn) mixed-metal cluster precursors onto OMSFs has been elaborated in **Chapter 4**. Both XRD and ethanol sorption analysis provide evidence of the mesostructural ordering. By adjusting different synthesis parameters such as the surfactant to silica ratio, the aging time and the spinning rate during spin-coating, mesoporous silicas with different morphologies and pore structures were synthesized. Bimetallic Pt-Ru catalysts have been prepared by immersing the mesoporous films in a solution containing mixed metal clusters $[Ph_4P]_2[Ru_5PtC(CO)_{15}]$. The mean diameter of the resulting, well-dispersed, isolated and anchored bimetallic nanoparticles is 1.35 nm with a very narrow partical size distribution. The relatively fragile mixed metallic clusters were mediated through the rigid inorganic framework providing protection and by the 3D distribution of the nanoparticles. The XPS data reveal the bimetallic character of the nanoparticles while TEM images show the intact mesoporosity after the encapsulation of the bimetallic clusters.

On glass and silicon substrates, it is crucial to reduce the synthesis time of the zeolitic film to less than 10 hours to avoid their dissolution. In **Chapter 5**, microwave assisted hydrothermal synthesis (MAHyS) was investigated and the results were compared with conventional hydrothermal synthesis of zeolite Beta coatings. A 750 nm zirconia layer, deposited by atomic layer deposition (ALD) from the $ZrCl_4$ and H_2O precursors, provided a good protection of the glass substrate during the synthesis in a highly alkaline solution. The coatings with an average crystal size of 500 nm have been obtained in MAHyS. The synthesis time was decreased to 8 hours

at 423 K by using the additive effect between fluoride ions and the zeolite seeds with an average particle size of 200 nm. In the absence of microwave heating, the hydrothermal *in situ* synthesis of zeolite Beta coatings required several days at 403 K. Higher synthesis temperatures resulted in a substantial dissolution of the glass substrates with the protective zirconia layer. The fully crystalline coatings with a high adhesion to the substrate were obtained after 48 hours from a synthesis mixture with template to alumina ratio of 24.

The microporous and mesoporous supports developed in this study were used as a catalyst support for Pt and Pd catalysts. The activity and selectivity in citral hydrogenation of Pt nanoparticles embedded in different micro- and meso- supports (Pt-Y zeolite, Pt-SAPO-5, Pt/MCM-41) have been reported in **Chapter 6**. The initial reaction rate in terms of TOF was the highest on the macroporous Pt-SiO_2 catalyst, followed by the micro-mesoporous Pt-MCM-41 and Pt-SAPO-5, and finally the microporous Pt-Y. The acid site concentration decreased in the reversed order. The H-Y support showed the highest activity in dehydration and double bond migration, which was due to its highest concentration of Brønsted acid sites. The H-SAPO-5 support was the most selective for hydrogenation towards the unsaturated alcohols with a selectivity of 57% at a citral coversion of 46%. A unique combination of a monosized pore diameter, weak Brønsted acidity, and a large Pt particle size contributed to a high selectivity. However, rapid deactivation occurred on this support due to adsorption of the dehydration products and partial pore blocking. The Pt-MCM-41 catalyst was the most selective for the formation of menthol while the deactivation rate was less pronounced as compared with the H-SAPO-5 support.

The chemical reaction processes that work best with microreactors have fast kinetics and usually generate high-value materials. However, in view of in the tailoring that is possible with microreactors, it is increasingly being recognized that major improvements in the selectivity of reaction products can be achieved by modifications of the catalysts and and support structures and compositions rather than in process conditions.

A series of bi- and tri-metallic catalysts supported on mesoporous oxide films were developed by integrating thin film technology with colloidal and cluster chemistry. A "one pot" sol-gel synthesis of mesoporous films with embedded colloidal nanoparticles has been described in **Chapter 7.** The method eliminates an additional impregnation step and produces a uniform distribution of the active component throughout mesoporous films. The activity and selectivity of the resulting clusters and colloidal nanoparticles supported on mesostructured silica thin films have been investigated in the batch and continuous modes in the hydrogenation of citral and phenyl acetylene. The studies in continuous mode were carried out in capillary microreactors, with a catalytic thin film deposited onto the inner surface. It has been shown that the selectivity towards the target product can be changed by varying the metal ratio in the bimetallic nanoparticles. The unsaturated alcohols with a maximum selectivity of 56% in cyclohexane were obtained. A high stability of the catalytic thin films allows further implementation of this technology in fine chemicals synthesis. This new family of microstructured reactors offers a wide range of possibilities due to the tunability of the chemical nature of the coating and its porous texture, as well as the "freedom of choice" of the catalytic species he significant adaptability or versatility of this approach is a direct consequence of the number of parameters that may be controlled or fine-tuned to fit specific needs. The following table summarizes a few of the properties that may be tailored.

Table 8.1. Tunable parameters of thin oxide films and selected procedures.

Parameter	Procedure
Ratio of metals in the nanoparticle (for bimetallic nanoparticles)	Change initial precursor concentrations
Nanoparticle size	Change amount of anti-agglomerant or increase nucleation kinetics
Porous structure of the coating	Change surfactant/fractional volume of surfactant in solution
Pore size	Use of co-surfactants (eg. *N*-butanol)
Coating thickness	Change delivery flow rate/perform multiple depositions
Nanoparticle structure (alloy versus core-shell)	Sequential addition of metallic precursors

8.2 Outlook

The development of large surface area support materials for application in multiphase microstructured reactors can further be developed towards:

(i) thicker films (up to the critical thickness to avoid internal diffusion limitations) by multiple spin-coating steps,

(ii) optimizing the nanoparticle synthesis deposition to reach a higher metal utilization [2], and

(iii) extra large surface area materials such as multiwall carbon nanotubes grown on top of the mesoporous films.

Multi wall carbon nanotubes (CNT) [3,4] can be considered as a catalyst support in microstructured reactors. To deposit CNT, an array of metallic nanoparticles can be fit into thin mesoporous oxide films to avoid their sintering during high temperature synthesis. The targeted CNT network will resemble the porous structure of the films [5]. Several novel metal-organic framework (MOF) coatings are another possible candidates for surface enlargement in microreactors [6].

The selectivity with which semihydrogenation is achieved in capillary microreactors is higher than that observed in batch systems under similar reaction conditions. In accordance with these results, a future prospect for application multiphase microstructured reactors would be the integration of a separation step in these systems by using e.g. affinity separators, will create the possibility of undertaking multistep synthesis [7]. In such a microreactor assembly, individual capillaries and affinity separators can be connected in series using appropriate fittings (click-together-interfaces). The main advantage of this approach is that end-users receive ready-to-use catalytic components which can be assembled on-site, similar to Lego components. Another advantage is that after finishing one chemical synthesis, the individual parts can be disassembled, cleaned and re-used in a different process.

The research described above has aimed to optimize reaction systems for single channel operation (i.e. at a more fundamental level). However, for industrial

applications it will become necessary to move from single to multichannel systems and, when doing this, achieving a uniform flow in each channel will be essential. Obviously there are other important factors as well, like process control, start up/ shut-down, catalyst characterization, etc., which will have to be addressed accordingly.

References

[1] L.N. Protasova, E.V. Rebrov, Z.R. Ismagilov, J.C. Schouten, *Micropor. Mesopor. Mater*. 123 (2009) 243-252.

[2] F. Studt, F. Abild-Pedersen, T. Bligaard, R.Z. Sørensen, C.H. Christensen, Jens K. Nørskov, *Science* 320 (2008) 1320-1322.

[3] M. D. Barreca, W.J. Blau, G.M. Croke, F.A. Deeney, F.C. Dillon, J.D. Holmes, C. Kufazvinei, M.A. Morris, T.R. Spalding, E. Tondello, *Micropor. Mesopor. Mater*. 103 (2007) 142-149.

[4] (a) M. Tamura, Y. Kemmochi, Y. Murakami, N. Chino, M. Ogura,, S. P. Naik, M. Takai, Y. Tsuji, S. Maruyama, T. Okubo, *Appl. Phys. A* 84 (2006) 247-250. (b) Y. Murakami, S. Yamakita, T. Okubo, S. Maruyama, *Chem. Phys. Lett*. 375 (2003) 393-398. (c) Y. Kemmochi, M. Hu, Y. Murakami, Y. Tsuji, M. Ogura, S. Maruyama, T. Okubo, *Trans Mater. Res. Soc. Jpn.* 30 (2005) 341-344.

[5] R. Fan, S. Huh, R. Yan, J. Arnold, P. Yang, *Nature Mater*. 7 (2008) 303-307.

[6] R. Ameloot, L. Stappers, J. Fransaer, L. Alaerts, B.F. Sels, D.E. De Vos, *Chem. Mater.* 21 (2009) 2580-2582.

[7] H.R. Sahoo, J.G. Kralj, K.F. Jensen, *Angew. Chem. Int. Ed*. 46 (2007) 5704-5708.

Acknowledgment

This thesis describes my work that was performed during my appointment at the Laboratory of Chemical Reactor Engineering (SCR) Research Group, Faculty of Chemical Engineering and Chemistry, Eindhoven University of Technology (TU/e), the Netherlands. First and foremost, I would like to thank my promotor Jaap Schouten and my supervisors Evgeny Rebrov and Mart de Croon who gave me trust, opportunity, encouragement, and required freedom with continuous feedback, stimulated my curiosity, respective fully nurtured my skills and certainly providing support for my personal development.

At SCR, I enjoyed the conducive environment shared with my MIRAACs partner (Maurice Warnier), my room-mates (Karen Scholz, Ouafae El Fahmi, Tanya Glazneva, Jovan Jovanovic, Chattarbir Singh, and Vladimir Dolmatov), my lab-mates (Martijn Mies and Lida Protasova), group-mates (Keshav Ruthiya, Vikrant Gangwal, Charl Stemmet, Patrick Wenmakers, Roman Tschentscher, Faysal Benaskar, Serdar Celebi, Poul van Male, Niek Zuidhof, Gregory Govender, Ma'moun Al-Rawashdeh, Mohamed Halabi, Stijn de Loos, Marco Meeuwse, Anton Dubrovskiy, Joost Rooze, Narendra Patil, Jiaqi Chen), other SCR research staffs (John van der Schaaf and Xander Nijhuis), and all SCR support team (Denise Tjallema-Dekker, Wim Groenland and Frank Grootveld, Anton Bombeeck, Madan Bindraban, Marlies Coolen-Kuppens, Peter Lipman, Erik van Herk, Dolf van Liempt, and Carlo Buijs), other TU/e researchers (Emiel Hensen, Adriana Creatore), and my MSc students (Jingyu Chen, Floris Helmich, Manja de Jonge, and Zhang Yi).

I would like to express my gratitude for all collaborators from the other groups in Europe: the Cambridge group (Brian Johnson, Tanya Khimyak, Vladimir Golovko and Angel Berenguer-Murcia), the Turku group (Paivi Maki-Arvela, Dmitry

Murzin), the Paris-Sud group (Pierre-Antoine Albouy), and the Delft group (Ugo Lafont and Patricia Kooyman).

I am grateful for financial support by STW and for all (near future) feedbacks from my Promotion Committee (Dmitry Murzin, Emiel Hensen, Volker Hessel and Kulathuiyer Seshan).

I thank all my Indonesian friends and the Indonesian communities who helped to make me feel at home in Delft and Eindhoven. For all badminton matches, lovely gathering and hot and delicious traditional foods, which accompanied my weekends.

I in person dedicate this thesis to my beloved family: my late father, my mother, my brother, my lovely wife and my sons, who have always supported me with their spirit, encouragement, and patience to have long distance relationship for 1 to 6 years in my life. I am deeply thanking to God the Almighty, who gave me continuous love.

Oki Muraza, Eindhoven, Fall 2009

List of Publications

Publications

[1] O. Muraza, E.V. Rebrov, T. Khimyak, B.F.G. Johnson, P.J. Kooyman, U. Lafont, M.H.J.M. de Croon, J.C. Schouten, Mesoporous silica films as catalyst support for microstructured reactors: Preparation and characterization, *Chemical Engineering Journal* 135 (2008) S99-S103.

[2] O. Muraza, E.V. Rebrov, J. Chen, M. Putkonen, L. Niinistö, M.H.J.M. de Croon, J.C. Schouten, Microwave-assisted hydrothermal synthesis of zeolite Beta coatings on ALD-modified borosilicate glass for application in microstructured reactors, *Chemical Engineering Journal* 135 (2008), S117-S120.

[3] O. Muraza, E.V. Rebrov, T. Khimyak, B.F.G. Johnson, P.J. Kooyman, U. Lafont, P.A. Albouy, M.H.J.M. de Croon, J.C. Schouten, Preparation and characterization of bimetallic catalysts supported on mesoporous silica films, *Studies in Surface Science Catalysis* 162 (2006) 167-174.

[4] O. Muraza, E.V. Rebrov, M.H.J.M. de Croon, J.C. Schouten, Enhancement of the stability of microporous silica films in non-aqueous solvents at elevated temperature, *Microporous and Mesoporous Materials* 124 (2009) 20-29.

[5] O. Muraza, E.V. Rebrov, P. Mäki-Arvela, N. Kumar, M.H.J.M. de Croon, D.Yu. Murzin, J.C. Schouten, Citral hydrogenation over Pt loaded micro- and mesoporous supports: the interplay between steric limitations and acidity (to be submitted to *Microporous and Mesoporous Materials*).

[6] O. Muraza, E.V. Rebrov, A. Berenguer-Murcia, Mart H.J.M. de Croon, J.C. Schouten, Selectivity control in hydrogenation reactions by confinement of polymetallic nanoparticles in mesoporous thin films, *Applied Catalysis A: General* (*in press* 2009), doi:10.1016/j.apcat1.2009.08.14.

Oral Presentations

[1] O. Muraza, E.V. Rebrov, M. Creatore, M.H.J.M. de Croon, J.C. Schouten, Influence of impregnation on the properties of mesoporous thin films deposited on metal substrates, in Proc. 9th Netherlands' Catalysis and Chemistry Conf.; Noordwijkerhout, Netherlands (2008).

[2] H.E. Skelton, O. Muraza, E.V. Rebrov, A. Berenguer-Murcia, J.C. Schouten, J. Robertson, B.F.G. Johnson, Surface nano-fabrication for lubricant applications, in Proc. 1st Int. Conf. on Functional Nanocoatings; Budapest, Hungary (2008).

[3] W. Keuning, E. Langereis, J.L. van Hemmen, O. Muraza, E. Rebrov, M.C.M. van de Sanden, W.M.M. Kessels, Remote Plasma ALD of Amorhous and Anatase TiO2 Studied by *In Situ* Spectroscopic Ellipsometry, in Proc. The 8th International Conference on Atomic Layer Deposition, Bruges, Belgium (2008).

[4] E.V. Rebrov, M.J.F. Warnier, O. Muraza, M.H.J.M. de Croon, V. Hessel, J.C. Schouten, Advanced catalytic microstructured reactor for continuous chemical synthesis integrated with a separation step, in Proc. AIChE Spring Meeting; Houston, TX, United States, CD-ROM nr. 95b (2007).

[5] E.V. Rebrov, M.J.M. Mies, O. Muraza, S.A. Kuznetsov, M.H.J.M. de Croon, J.C. Schouten, Application of functional and catalytic coatings in microstructured reactors, in Proc. 6th Anque Int. Congr. on Chemistry; Tenerife, Spain, pp. 321-322, (2006).

[6] O. Muraza, E.V. Rebrov, U. Lafont, P.J. Kooyman, P.A. Albouy, T. Khimyak, B.F.G. Johnson, M.H.J.M. de Croon, J.C. Schouten, Mesoporous silica films as catalyst support for microstructured reactors, in Book of Abstract 6th Netherlands Process Technology Symposium; Veldhoven, Netherlands, p. 33 (2006).

[7] O. Muraza, P.J. Kooyman, U. Lafont, P.A. Albouy, T. Khimyak, E.V. Rebrov, M.H.J.M. de Croon, J.C. Schouten, Preparation and characterization of bimetallic catalysts supported on mesoporous silica films, in Proc. 9th Int. Symp. Scientific bases for the Preparation of Heterogeneous Catalysts; Editors: Gaigenaux et al., Louvain-la-Neuve, Belgium (2006).

[8] O. Muraza, U. Lafont, P.J. Kooyman, P.A. Albouy, T. Khimyak, E.V. Rebrov, M.H.J.M. de Croon, J.C. Schouten, Preparation of mesoporous catalytic coatings on borosilicate glass for application in microstructured reactors, in Book of abstracts Netherlands Catalysis and Chemistry Conference (NCCC VII); Noordwijkerhout, Netherlands, O71, p. 135 (2006).

[9] O. Muraza, E.V. Rebrov, U. Lafont, P.J. Kooyman, P.A. Albouy, T. Khimyak, B.F.G. Johnson, M.H.J.M. de Croon, J.C. Schouten, Preparation of mesoporous catalytic films on borosilicate glass for application in microstructured reactors, in Book of abstracts 4th EFCATS School of Catalysis; Editors: V.I. Bukhtiyarov, St. Petersburg, Russia, O18, p. 56 (2006).

[10] E.V. Rebrov, M.J.M. Mies, O. Muraza, T.S. Glazneva, S.A. Kuznetsov, M. Putkonen, M.H.J.M. de Croon, Z.R. Ismagilov, J.C. Schouten, Application of functional and catalytic coatings in microstructured reactors, in CERC3 Young Chemists Workshop on Microreactor Technology; Enschede, Netherlands, p. 2, (2006).

[11] W. Keuning, J.L. Van Hemmen, O. Muraza, E.V. Rebrov, M.C.M. van de Sanden, W.M.M. Kessels, Film Properties and *In Situ* Optical Analysis of TiO_2 Layers Synthesized by Remote Plasma ALD, in Book of abstracts AVS 54th International Symposium & Exhibition, Seattle, United States, TF-MoA9 (2007).

[12] A. Berenguer-Murcia, E.V. Rebrov, O. Muraza, B.F.G. Johnson, J.C. Schouten, Development of thin inorganic films with high loadings of confined colloids, in Proc. 14th Int. Congress on Catalysis; Seoul, Korea (2008).

[13] O. Muraza, J.C. Jansen, The First Attempts to Synthesize Zeolite Membranes from MTT Structure; An Exploratory Study for Application in Hydroisomerization, in Proc. Indonesian Students' Scientific Meeting 2004, Aachen, Germany, (2004) ISSN: 0855–8692.

Poster Presentations

[1] E.V. Rebrov, O. Muraza, M.H.J.M. de Croon, J.C. Schouten, Enhancement of the stability of microporous silica films in non-aqueous solvents at elevated temperature, in Book of Abtract, EuropaCat IX, Salamanca, Spain, P10-40, p. 526 (2009).

[2] O. Muraza, E.V. Rebrov, M. Creatore, M.H.J.M. de Croon, M.C.M. van de Sanden, J.C. Schouten, Synthesis of Mesoporous Oxide Coatings and Their Characterization by Ellipsometric Porosimetry, in Book of abstracts EuropaCat VIII, Åbo-Turku, Finland, P2-87 (2007).

[3] V.B. Golovko, E.V. Rebrov, O. Muraza, P. Abdulkin, T. Khimyak, M.H.J.M. de Croon, B.F.G. Johnson, J.C. Schouten, Metal nanoparticles derived from cluster precursors supported onto mesoporous SiO_2 film as a novel catalyst system for prospective applications in microstructured reactors, in Book of abstracts Europacat VIII, Åbo-Turku, Finland, P2-140 (2007).

[4] O. Muraza, E.V. Rebrov, T. Khimyak, B.F.G. Johnson, P.J. Kooyman, U. Lafont, M.H.J.M. de Croon, J.C. Schouten, Mesoporous silica films as catalyst support for microstructured reactors: preparation and characterization, in Book of Abstracts the 9th International Conference on Microreaction Technology (IMRET 9), Postdam-Berlin, Germany, P36, p. 239-240 (2006).

[5] O. Muraza, E.V. Rebrov, M. Creatore, W. Keuning, W.M.M. Kessels, M.H.J.M. de Croon, M.C.M. van de Sanden, J.C. Schouten, Pore structure characterization of meso-SiO2 coatings on glass and silicon substrates by ellipsometric porosimetry, in Book of Abstracts Netherlands' Catalysis and Chemistry Conference, Noordwijkerhout, Netherlands, P104, p. 256, (2007).

[6] O. Muraza, E.V. Rebrov, J. Chen, M. Putkonen, L. Niinistö, M.H.J.M. de Croon, J.C. Schouten, Microwave-assisted hydrothermal synthesis of zeolite beta coatings on ALD-modified borosilicate glass for application in microstructured reactors, in Book of Abstracts the 9th International Conference on Microreaction Technology (IMRET 9), Postdam-Berlin, Germany, P37, p. 241-242 (2006).

[7] O. Muraza, U. Lafont, E.V. Rebrov, M.H.J.M. de Croon, J.C. Schouten, Mesoporous silica films as catalyst supports on borosilicate glass: preparation and characterization, in Proc. E-MRS 2005 Spring meeting, Symp. E: Synthesis, Characterization and Applications of Mesostructured Thin Layer, Strasbourg, France, E/PII.51, (2005).

About the Author

Oki Muraza was born on October 27, 1978 in Jakarta, Indonesia. He finished secondary school education at SMA Taruna Nusantara Magelang, Indonesia in 1996. In 2001, he obtained a B.Sc. degree in Chemical Engineering from *Institut Teknologi Bandung* (ITB). During this bachelor period, he did an internship in styrene-butadiene latex plant at Dow Chemical. His final project was on polymeric membranes under supervision of Dr. I. Gede Wenten in the Downstream Processing Laboratory, Inter University Research, ITB. From 2001 until 2002, he was working in Offshore Oil and Gas operation with Repsol YPF, Asia Pacific as Chemical Supervisor and later Production Supervisor. In 2002-2004, he obtained a scholarship and enrolled in the MSc International Program of Chemical Engineering at the *Technische Universiteit Delft* (TUD) in the Netherlands. During this master period, he did an internship at the Shell Research and Technology Centre Amsterdam (SRTCA). He finished his MSc research on the topic "*The First Attempts to Synthesize Zeolite Membranes from MTT and TON Structures*" at the PORE Ceramic Membrane Centre under supervision of Prof.em.dr. J.C. (Koos) Jansen. From October 2004 until March 2009, Oki was employed as a Junior Researcher at the Laboratory of Chemical Reactor Engineering of the *Technische Universiteit Eindhoven* (TU/e) under supervision of Prof.dr.ir. Jaap C. Schouten, Dr. Evgeny V. Rebrov and Dr. Mart H.J.M. de Croon.